

X 90-36052

X 90-36052\*

NASA Technical Memorandum 4194

*nasa pers. only*

# Close-Range Photogrammetric Measurement of Static Deflections for an Aeroelastic Supercritical Wing

Thomas A. Byrdsong, Richard R. Adams,  
and Maynard C. Sandford

DECEMBER 1990

**NASA**

# Close-Range Photogrammetric Measurement of Static Deflections for an Aeroelastic Supercritical Wing

Thomas A. Byrdsong, Richard R. Adams,  
and Maynard C. Sandford

*Langley Research Center  
Hampton, Virginia*



National Aeronautics and  
Space Administration

Office of Management  
Scientific and Technical  
Information Division

1990

## Summary

Close-range photogrammetric measurements were made for the lower surface of an aeroelastic supercritical research wing having a full-span aspect ratio of 10.3. The measurements were made during wind-tunnel tests of quasi-steady pressure distributions on the wing. The tests were conducted in the Langley Transonic Dynamics Tunnel at Mach numbers up to 0.900 and dynamic pressures up to about 300 psf. Deflection data were obtained at 57 locations on the wing lower surface with dual nonmetric still-frame cameras. Representative data are presented as a graphical overview to show variations and trends of spar deflection with test variables. Comparative data are presented for photogrammetric and cathetometric results of measurements of the wingtip deflections.

## Introduction

The Langley Research Center has conducted an aeroelastic research wing program to evaluate transonic aerodynamic computer codes for the prediction of lifting surface loadings. The research program consisted primarily of wind-tunnel measurements of steady and unsteady pressure distributions on wing models and correlation of these measurements with computational results. Quasi-rigid and flexible semispan wing models were used in the wind-tunnel tests. Thus far, three quasi-rigid models have been tested in the Langley Transonic Dynamics Tunnel: a delta wing model (ref. 1), a swept wing model with supercritical airfoil sections (ref. 2), and a rectangular wing model with a supercritical airfoil (ref. 3). These models were designed and fabricated to minimize structural dynamic effects and, accordingly, to simplify correlation of the experimental data with computational results.

More recently, wind-tunnel measurements have been completed for a fourth model of the aeroelastic research wing program (refs. 4 through 6). Both static and dynamic data were obtained for this highly flexible wing which was designed for a flight-test program to evaluate active control systems. Selected results from dynamic pressure measurements for the flexible wing are reported in references 5 and 6, and the measured static pressure data are currently being analyzed. The measured static pressure distributions were supplemented with corresponding measurements of wing surface deflections to provide for more meaningful results.

The purpose of this paper is to document the results of wing surface deflection measurements for their corresponding wing surface static pressure measurements. The documentation presented herein

graphically shows variations of the primary wing spar shapes and wingtip deflections as a function of the various test variables to provide views of the trends developed in the data. Tabulations of all wing surface deflection measurements are presented in a "Supplement to NASA Technical Memorandum 4194," which is available on request, for use in evaluation of theoretical techniques under development. A request form is included at the back of this report. Wing surface deflection measurements were obtained for a range of Mach number from 0.600 to 0.900, a range of angle of attack from  $-2^\circ$  to  $4^\circ$ , a range of control surface deflection from  $-8^\circ$  to  $8^\circ$ , and dynamic pressures up to about 300 psf. Wing deflections at 57 locations were obtained with two nonmetric still-frame cameras synchronized to an electronic flash. Cathetometric measurements of some of the wingtip deflections were also obtained. The tests were conducted in a heavy gas medium.

## Symbols

$a_0$	Y-axis intercept of linear equation
$a_1$	slope of linear equation
$b$	wing semispan, in.
$C_{cor}$	correlation coefficient
$c$	wing streamwise local chord, in.
$M$	free-stream Mach number
$p_s$	static pressure, psf
$p_t$	stagnation pressure, psf
$q$	free-stream dynamic pressure, psf
$T$	stagnation temperature, $^\circ$ R
$X_S$	streamwise spatial coordinate, in.
$X_{S,rms}$	estimated root-mean square precision of spatial coordinate $X_S$
$x_c$	streamwise station coordinate for each camera, in.
$x_l$	local streamwise distance from wing leading edge, in.
$Y_S$	spanwise spatial coordinate, in.
$Y_{S,rms}$	estimated root-mean-square precision of spatial coordinate $Y_S$
$y_c$	lateral station coordinate for each camera, in.
$y_l$	perpendicular distance from wing line of symmetry, in.
$Z_S$	vertical spatial coordinate, positive up, in.

$Z_{S,\text{avg}}$	average value of targets $Z_{S,1002}$ and $Z_{S,1004}$ relative to wind-off value of corresponding $Z_S$ , in.
$Z_{S,C}$	cathetometric measurement of vertical spatial coordinate $Z_S$ relative to wind-off condition, in.
$Z_{S,P}$	photogrammetric measurement of vertical spatial coordinate $Z_S$ relative to wind-off condition, in.
$Z_{S,\text{rms}}$	estimated root-mean-square precision of spatial coordinate $Z_S$
$Z_{S,1002}$	vertical spatial coordinate of target 1002, in.
$Z_{S,1004}$	vertical spatial coordinate of target 1004, in.
$z_c$	vertical station coordinate for each camera, in.
$\alpha$	angle of attack of model at wing root chord, positive leading edge up, deg
$\delta$	static angle of outboard control about hinge line, positive leading edge up, deg
$\eta$	wing nondimensional semispan station, $y_l/b$
$\theta$	elevation angle of orientation for each camera, deg
$\phi$	roll angle of orientation, deg
$\psi$	azimuth angle of orientation for each camera, deg

#### Abbreviations:

rms	root mean square
W.O.Z.	wind-off zero

### Model

Views of the test configuration mounted in the Langley Transonic Dynamics Tunnel are shown in figures 1 and 2, and the wing planform and photogrammetric targets mounted on the wing lower surface are shown in figures 3 through 5. The wing had a full-span aspect ratio of 10.3 and a leading-edge sweep angle of  $28.8^\circ$ . The wing was equipped with three trailing-edge control surfaces (figs. 3 through 5) that were hydraulically driven. Two of the control surfaces were located near the root chord and one was located near the tip chord. Location coordinates for

the control surfaces are shown in figure 4. The inboard control surfaces were fixed at a deflection angle of  $0^\circ$ , and the outboard control surface was deflected to predetermined static angles in the approximate range from  $-8^\circ$  to  $8^\circ$ . Only the deflection angle of the outboard control surface was varied during this study. The hinge line of the outboard control was located at 77 percent of the local wing chord. The wing front and rear spar centerlines were located on the 25-percent and 62-percent chord lines on the basic wing planform, respectively (fig. 5).

The wing contour was formed by three supercritical airfoil sections that were located at wing nondimensional semispan stations  $\eta$  of 0.071, 0.426, and 1.000, and the corresponding airfoil thickness-to-chord ratios were 15 percent, 12 percent, and 11 percent, respectively. Straight line interpolation along constant-percent chord lines defined the wing contour between the three airfoils. The airfoil coordinates and twist distribution for the wing cruise condition are defined in reference 7, and additional geometric and structural characteristics are given in reference 4.

Circular targets were located on the wing lower surface (fig. 1) to define the surface deflection (or shape). The inboard rows of targets were orientated perpendicular to the rear spar in order to facilitate comparisons with structural analysis programs. The rows near the model tip were orientated streamwise to facilitate comparisons with aerodynamic analysis programs. Sixty-five targets were provided; however, only 57 targets were visible for the deflection measurements. The visible target locations on the wing lower surface are identified in figure 3. The targets, which are commonly used for printed circuit artwork, were dark red in the shape of an annulus with an outside diameter of 1 inch and a thickness of 5 mils. The white painted wing surface visible at the center of the pads provided the required high contrast target for the photographic images. Specular reflections were minimized by use of an over-spray of clear flat lacquer. The central hole diameters in the pads were selected to present constant image sizes of about 100 micrometers on the films as photographed by the inboard cameras. The central hole diameter ranged from 65 mils for the inboard targets to 125 mils for the outboard targets. The visible targets were located on the wing in 10 semispan rows between the wing root and tip and at up to 8 chordwise positions. The wing target locations from surface table measurements are shown in table 1. The corresponding target coordinates corrected for the axis system used in the photogrammetric data reduction are shown in table 2. A description of the corrections in table 2 is discussed in the section "Data Reduction." An

additional set of 18 high-contrast targets was placed on the test-section wall opposite the model mount within the field of view of each camera. These data were used to provide a basis for image restitution in the absence of film fiducial marks.

Boundary-layer transition strips were placed on the wing upper and lower surfaces for selected test conditions. The transition strips were 0.10 inch wide and were made of No. 70 Carborundum grit embedded in a plastic adhesive. The size and location of each strip were determined from experiences gained by using transition strips on similar wind-tunnel models. The strips were located on the 5-percent chord line from root to tip of the basic wing planform. The model surface forward of the strips was kept smooth to maintain laminar flow.

## Instrumentation

Wing deflection data were recorded simultaneously on photographic film by use of two still-frame 70-millimeter square-format nonmetric cameras that were rigidly mounted behind high-strength glass windows in the test-section sidewall approximately 26 inches below  $Z_{S,\text{avg}}$  of the wing coordinates. (See fig. 1.) The cameras were separated by a distance of 41 inches and were fitted with 50-millimeter focal-length lenses focused to a distance of 5 feet. Illumination was provided by a high-intensity strobe lamp located behind a window beneath the wing. Exposures were made remotely upon command by a control room observer. A logic circuit was used to assure that both camera shutters were open before allowing the strobe lamp to trigger. Seventy frame pairs could be exposed before film magazine reloading was required.

The relative vertical deflection of the wingtip was measured by use of a cathetometer to provide quick-look information. The cathetometer was mounted in the wind-tunnel control room behind windows of high-strength safety glass which provided a direct view of the test configuration (fig. 2). A horizontal line was drawn on the wingtip that approximated the wingtip chord line. During the test an orthogonal hairline system in the cathetometer optics was focused on the wingtip chord line for relative vertical displacement measurements.

## Wind Tunnel

The test was conducted in the Langley Transonic Dynamics Tunnel (ref. 8). This facility is a single-return wind tunnel that has a 16.00-foot square test section with cropped corners. The test section walls, ceiling, and floor are equipped with streamwise longitudinal slots. The stagnation pressure can be

varied from slightly above atmospheric pressure to near vacuum over the Mach number range from 0 to 1.2. The tunnel is a continuous-operation type and is powered by a motor-driven fan. Both test section Mach number and dynamic pressure are continuously controllable. The facility has the capability to use air or heavy gas (R-12) as a test medium. Heavy gas was used as the test medium for most of these test runs.

## Data Reduction

Data reduction of the wing surface deflection measurements was accomplished by use of the theory of photogrammetry. The theory is based upon a pair of equations (referred to as the projective equations) which relate the two-dimensional measured coordinates  $(x, y)$  of a film image and the corresponding three-dimensional spatial coordinates  $(X_S, Y_S, Z_S)$  of the target photographed. For this test program, the projective equations for each camera contained a total of 14 projective parameters (or elements of orientation). The calibration required for these measurements consisted of recovery of eight internal elements of orientation (referred to as the camera parameters) for each camera and six external elements of orientation (or station parameters) for each station. The camera parameters consisted of the principal distance of the lens, the image coordinates of the principal point, and five additional parameters which include three radial and two decentering lens distortion coefficients for each camera. The station parameters consisted of three station coordinates and three pointing (or orientation) angles for each camera station. A nonstandard technique was developed for image restitution due to the use of nonmetric cameras to record wing deflections. Also, the use of such cameras prevented removal of image errors that were introduced by film dimensional changes. A detailed discussion of the theory, equations, and the self-calibration process used in close-range photogrammetry is presented in reference 9.

## Photographic Methods

Two sequences of photographs of the model (photographic calibrations) were made prior to testing. The first sequence was referred to as the self-calibration photography, and the second sequence was referred to as the angle-of-attack calibration photography. The required photographs for each sequence were obtained sequentially and only after completion of both sequences were the films removed from the cameras and processed.

***Self-calibration photography.*** The self-calibration photography sequence of photographs was used to provide the data to recover the internal elements of orientation for the two cameras and

to provide coordinates of the wing targets in a properly scaled (but arbitrary) wing coordinate system. The targeted wing ( $\alpha = 0^\circ$ ) was photographed in the test section with each camera from six locations that were circumferentially distributed beneath the wing. The cameras were rolled about their lens axes a different amount for each photograph. Finally, the self-calibration sequence was completed by mounting and locking the two cameras into their permanent test positions behind the tunnel windows beneath the wing and taking a seventh and final photograph of the targeted wing lower surface (fig. 1(b)).

**Angle-of-attack calibration photography.** The angle-of-attack calibration photography sequence of photographs was used to provide the data to transform the resulting wing coordinate system (obtained from the self-calibration photography) into a preferred wing coordinate system and to remove the rigid-body rotation component from the data. Also, image coordinate data were obtained from this sequence of photographs for the 18 additional targets that were located on the tunnel side wall. Seven pairs of photographs were taken of the test wing and wall target grid from each camera as angle of attack was varied in increments of approximately  $1^\circ$  in the interval from  $-2^\circ$  to  $4^\circ$ .

### Film Measurement

Two-dimensional coordinates from the film were obtained for each target image on each film negative subsequent to film processing. Multiple readings of each coordinate were manually obtained by a precision monocomparator that was monitored by a microcomputer. The computer was programmed to accept the data when two successive measurements of each target (both  $x$ - and  $y$ -coordinates) were repeated within 10 micrometers. Coordinates of visible frame corners were also measured. Long-term instrument drift was found to exist in the comparator system; this drift was also monitored for each negative. The data were discarded when the coordinates of the first target measured differed by more than 15 micrometers when reread after reading all other targets. Seventy-five targets were measured on each film negative. Calibration and test photography generated a total of 700 negatives which required considerable manual comparator observation.

### Image Data Preprocessing

The use of nonmetric cameras which lack discrete fiducial marks precluded the use of a direct standard two-dimensional coordinate transformation to convert raw image coordinates from an arbitrary com-

parator axis system to the conventional  $X$ - $Y$  fiducial axis system. To overcome this difficulty, the frame corner data were used for this transformation. The four square-frame corners of each negative were measured for self-calibration and angle-of-attack sequences. In these cases, the origin was established at the computed intersection of the frame diagonals. The orientation was then fixed by an in-plane rotation about the new origin to place the reference frame edge parallel to the abscissa axis.

For test photography, it was necessary to operate under reduced test section ambient lighting to insure that fast strobe illumination predominated the exposures for the moving targets. Only two corners of the reference edge of each frame were measurable. These corners were used to establish the reference edge. In this case, the origin was temporarily established at the right angle apex opposite the reference edge (hypotenuse) of a  $45^\circ$  triangle. The image quality of the frame corners was insufficient to allow scaling of image data. The image data were then corrected for systematic comparator errors.

The final step in preprocessing of the image data involved the wall target image data that were obtained from the angle-of-attack photograph sequence. The quality of the wall target image data was quite good and resulted in highly repeatable image coordinates. The good quality of the wall target images was attributed to photographic exposure under high ambient illumination levels. Since the wall target grid appeared in all subsequent test photographs, their image coordinates were utilized (in lieu of fiducial marks) for the final image plane transformation of test image data. Subsequently, all image data from each camera frame (not including self-calibration photographs) were transformed to best overlay, in a least-squares sense, the images from this target subset. Again, the transformation was confined to the image plane (two translations and one rotation) and the scale was held fixed.

### Wing Deflection Data Processing

Simultaneous Triangulation and Resection System (STARS, ref. 10) photogrammetric software was used to analyze the preprocessed image data. Individual modules of this software were utilized as follows to produce the desired results.

**Self-calibration.** Preprocessed image data from the self-calibration photographic sequence were merged, and a two-camera bundle adjustment (refs. 9 and 10) with self-calibration was performed. This procedure involved the solution of 1960 projective equations for 310 unknowns. Absolute control for this adjustment was established by use of known

$X, Y, Z$  coordinates of two inboard wing targets (102 and 105) and the  $Z$ -coordinate of an outboard wingtip target (1003) as given in table 1. These three control points (targets 102, 105, and 1003) define a unique spatial coordinate system. The STARS bundle adjustment not only recovered the internal elements of orientation (principal distance, principal point location) for each camera, but also the lens distortion coefficients and external elements of orientation (the three station coordinates and the three pointing angles) for each camera station. The  $X, Y, Z$  coordinates for all targets in the system defined by the control points were also recovered from the adjustment. However, rather than generate a reference coordinate system from three selected control points, a preferred wing coordinate system was generated with all the measured data of table 1. This was accomplished in a least-squares formulation with the STARS Rigid Body Transformation module (ref. 10).

Since the scale was allowed to adjust during the transformation and a knowledge of the external elements of orientation of the two fixed camera stations was required for subsequent steps, the bundle adjustment was repeated with the control point coordinates fixed to the values obtained from the rigid body transformation. Rigorous error propagation emerged directly from the least-squares bundle adjustment (ref. 9). The  $Z$ -coordinates for the wing targets in the preferred wing coordinate system were recovered from this 14-station least-squares adjustment to an estimated rms precision of 0.0045 inch.

**Angle-of-attack calibration.** The wing was tested at various angles of attack with the camera stations fixed in the preferred coordinate system. The resulting  $X, Y, Z$  coordinates of the wing targets contained both the desired wing deformation data and the angle-of-attack rotation component. The angle-of-attack calibration was thus used to provide a means for separating the rotational component from the deformation data.

The preprocessed image data obtained from the angle-of-attack photographic sequence were merged in pairs and the STARS Triangulation module was used to obtain  $X, Y, Z$  coordinate sets at each of seven calibration angles of attack. The projective parameters used for the triangulation were those determined from the self-calibration. Since the wing was assumed to be a rigid body for this calibration sequence, the only variable between the resulting data sets was the angle-of-attack rotation. To verify that this was the case, a rigid body transformation (with scale fixed) was performed to best overlay the triangulated data sets from the two extreme angles of attack ( $-2^\circ$  and  $4^\circ$ ). The result of this transforma-

tion showed that the differences between the transformed set and the primary set were minimal. Also, this result verified that the actual coordinate system and the preferred wing coordinate system (as previously obtained) were not precisely mutually orthogonal. The coordinate system was corrected so that the  $Y$ -axis in the wing coordinate system was parallel to the axis of rotation in the tunnel system for changes in angle of attack. Once mutual orthogonality between the two systems was established, three final translations were made to adjust the preferred wing system to the actual tunnel system. The final coordinates of the wing targets in the tunnel coordinate system at zero angle of attack and the wind-off condition are given in table 2. The  $Z$ -precision estimates (table 3) reflect the overall effect of uncorrected image measurement errors—propagated through the recovery of the projective parameters—to the triangulated results from the pretest calibrations.

The corrected target coordinates (table 2) were collectively used as a control for a final bundle adjustment, using the preprocessed image data for the seven calibration angles of attack. All targets participated equally (in a least-squares sense) in the adjustment; effectively the previously established tunnel coordinate system was preserved. Except for the camera principal points, the internal elements of orientation and lens distortion parameters were rigidly constrained to their original self-calibration values. The station parameters were allowed to freely adjust. Three station coordinates and three pointing angles were recovered for each camera at each calibration angle of attack. These parameters were linear functions of angle of attack; hence, the slope-intercept equations were used for computation of the six station parameters for each camera. The recovered station parameters and corresponding computed slope-intercept equation coefficients for both camera stations are summarized in table 4.

**Triangulation of results.** The coordinates of each wing target for the test data were triangulated with the use of the calibrated camera parameters and the computed station parameters for each tab point. The average value of the estimated rms precision for the resulting  $Z$ -coordinates for all tab points was found to be 0.011 inch varying from 0.006 (inboard targets) to 0.015 inch (outboard targets near wingtip). The rotational component of angle of attack was removed from the data, so that wing shape deformations due to aerodynamic loading could be obtained by direct subtraction of triangulated  $Z$ -values for corresponding targets given in table 2.

## Accuracy of Wind-Tunnel Parameters and Model Angles

### Mach Number and Dynamic Pressure

Wind-tunnel flow parameters are obtained by measuring four primary values. They are stagnation pressure  $p_t$ , static pressure  $p_s$ , stagnation temperature  $T$ , and the percent purity of the gas medium from which the ratio of specific heats is obtained. The stagnation and static pressures are measured by two modern laboratory quality pressure gauges. The accuracy of these gauges is 0.02 percent of full scale which is approximately 0.4 psf over the tunnel operation pressure range of 0 to 2200 psf. The values of stagnation temperature and the ratio of specific heats do not vary appreciably during most testing and do not contribute any significant errors to the calculation of flow parameters such as Mach number

$M$  and dynamic pressure  $q$ . It is well-known that  $q$  is related directly to the value of  $p_s$  and that  $M$  is a function of the square root of  $q$ . Therefore, for most testing in the Langley Transonic Dynamics Tunnel operating envelope, the Mach number is set and held to within 0.002 of the desired value, and the dynamic pressure value is accurate to well within 1.0 psf.

### Wing-Root Angle of Attack and Control Surface Angle

The model was instrumented near the wing root with a servo accelerometer and at the inboard side of the control surface shaft with a precision rotary potentiometer. The accuracy of the accelerometer allowed the wing angle of attack to be set to within  $0.01^\circ$ . The control surface angle was accurate to within  $0.1^\circ$ .

## Presentation of Results

The results of quasi-steady deflection measurements for an aeroelastic research wing are tabulated in a "Supplement to NASA Technical Memorandum 4194." Representative results from the supplement for a typical test condition are presented in table 5, which shows the spatial coordinates for the wing targets and the corresponding test conditions. In table 5, the spatial coordinate entries which are a series of 9's indicate that the data were not available or were defective. A compilation of quasi-steady test conditions is presented in table 6. The data of table 6 show the tab point, Mach number, dynamic pressure, angle of attack, and outboard control surface deflection angle. A correlation between the graphic and tabulated results is given in table 7. Unless otherwise stated, the tests were conducted in a heavy gas medium (R-12).

A graphical overview of the results in the supplement is presented in figures 6 through 30 as indicated in the following table. Data are presented in figures 6 and 7 to show a comparison of the results obtained from photogrammetric and cathetometric measurements and chordwise deflection of the model at various loadings, respectively. The front and rear spar deflections for variations of angle of attack and outboard control surface deflection are presented in figures 8 through 22. Variations of the spar tip deflection as a function of angle of attack and control surface deflection are presented in figures 23 through 28. Limited data are also presented in figures 29 and 30 to show some effects of dynamic pressure and Mach number on spar tip deflections.

### Figure

Photogrammetric and cathetometric results for wingtip measurements	6
Effect of dynamic pressure on wing chordwise deflection at selected rows of targets along the span at $M = 0.850$ , $\alpha = 1^\circ$ , and $q = 100, 200$ , and $300$ psf	7
Variation of wing front and rear spar shapes with angle of attack at four Mach numbers and $q = 100$ psf	8
Variation of wing front and rear spar shapes with control surface deflection at two angles of attack, $q = 100$ psf, and $M = 0.600$	9
Variation of wing front and rear spar shapes with control surface deflection at two angles of attack, $q = 100$ psf, and $M = 0.700$	10
Variation of wing front and rear spar shapes with control surface deflection at two angles of attack, $q = 100$ psf, and $M = 0.800$	11
Variation of wing front and rear spar shapes with control surface deflection at two angles of attack, $q = 100$ psf, and $M = 0.850$	12
Variation of wing front and rear spar shapes with control surface deflection at two angles of attack, $q = 100$ psf, and $M = 0.880$	13

Variation of wing front and rear spar shapes with angle of attack at four Mach numbers and $q = 200$ psf	14
Variation of wing front and rear spar shapes with control surface deflection at two angles of attack, $q = 200$ psf, and $M = 0.600$	15
Variation of wing front and rear spar shapes with control surface deflection at two angles of attack, $q = 200$ psf, and $M = 0.700$	16
Variation of wing front and rear spar shapes with control surface deflection at two angles of attack, $q = 200$ psf, and $M = 0.800$	17
Variation of wing front and rear spar shapes with control surface deflection at two angles of attack, $q = 200$ psf, and $M = 0.850$	18
Variation of wing front and rear spar shapes with angle of attack at $M = 0.800$ and $q = 300$ psf	19
Variation of wing front and rear spar shapes with control surface deflection at $\alpha = 0^\circ$ , $q = 300$ psf, and $M = 0.800$	20
Variation of wing front and rear spar shapes with angle of attack at $M = 0.800$ and $q = 100$ psf in air	21
Variation of wing front and rear spar shapes with control surface deflection at two angles of attack, $q = 100$ psf, and $M = 0.800$ in air	22
Variation of wing front and rear spar tip deflection with angle of attack at four Mach numbers and $q = 100$ psf	23
Variation of wing front and rear spar tip deflection with angle of attack at four Mach numbers and $q = 200$ psf	24
Variation of wing front and rear spar tip deflection with angle of attack at $M = 0.800$ and $q = 300$ psf	25
Variation of wing front and rear spar tip deflection with control surface deflection at five Mach numbers, two angles of attack, and $q = 100$ psf	26
Variation of wing front and rear spar tip deflection with control surface deflection at four Mach numbers, two angles of attack, and $q = 200$ psf	27
Variation of wing front and rear spar tip deflection with control surface deflection at $\alpha = 0^\circ$ , $M = 0.800$ , and $q = 300$ psf	28
Variation of average wing spar tip deflection with dynamic pressure at $M = 0.700, 0.800$ , and $0.850$ and three angles of attack	29
Variation of average wing spar tip deflection with Mach number at $q = 100$ and $200$ psf and three angles of attack	30

## Discussion of Results

Photogrammetric data were obtained for the test conditions when the response of the wing to the aero-dynamic loading was characterized as either static or quasi-static. Since the photogrammetric technique used in this test program generated instantaneous deflection data, care was taken to avoid recording data when the model tip response was significantly unsteady due to excessive noise, turbulence, flow separation, or other flow phenomena (ref. 11). This unsteady response was the experience for many test conditions at high dynamic pressures and/or Mach numbers. Subsequent to photography, an additional visual deflection measurement was made of the wingtip elevation by use of

a cathetometer. The cathetometric measurements were monitored over a period of about 15 seconds to obtain an average value of the relative wingtip elevation.

Photogrammetric and cathetometric results are graphically presented in figure 6. The photogrammetric results were obtained for measurements of target 1003 which is located midway between the front and rear spars on target row 10. The cathetometric results were obtained from measurements of a line on the wingtip between the projected front and rear spars. A line of agreement and a first-order regression line (least-squares fit) are included with the data as an aid for comparison. The data of figure 6 show that there was good agreement between the photogrammetric and cathetometric techniques. The slope of

the regression line is about 5 to 6 percent lower than that for the line of agreement. This difference is considered to be small and is attributed to the use of nonmetric cameras, the relative location of the target to the wingtip, and the unsteadiness of the model.

### Wing Chordwise Bending

Selected data from the photogrammetric results are presented in figure 7 to indicate the chordwise rigidity of the wing at various locations along the span (fig. 3). The data of figure 7 show variations of the net local chordwise deflections normalized by the free-stream dynamic pressure at four different stations. As indicated in the figure, results are presented for three free-stream dynamic pressures at four spanwise stations. The wing deflections are the net measured values (wind-off values removed) normalized by the dynamic pressure for targets located on rows 2, 5, 7, and 9 (fig. 3). Rows 2, 5, and 7 were approximately normal to the wing rear spar, and row 9 was streamwise. The data indicate that the local deflection along the chordwise stations was essentially linear for each row of targets and for each dynamic pressure. The data for the more inboard row of targets (row 2) show a near-zero slope, and small positive slopes are shown for the other rows. Furthermore, the slope of the chordwise deflections became larger as the location of the rows approached the wingtip. The essentially constant slope of the local chordwise deflections for these data indicates that there was sufficient chordwise rigidity of the wing to effectively prevent chordwise bending of the wing model for the range of test conditions.

### Wing Spar Deflection

A graphical overview of the photogrammetric wing surface deflection measurements in the heavy gas medium, unless otherwise noted, is presented in the form of plots which show spanwise variations of the vertical deflection (i.e., the vertical spatial coordinate) for the front and rear spars. The results are arranged according to dynamic pressure and Mach number. For increasing Mach number, figures 8 through 13 show deflection data for a dynamic pressure of 100 psf, figures 14 through 18 show deflection data for a dynamic pressure of 200 psf, and figures 19 and 20 show deflection data for 300 psf. Additional deflection data for a dynamic pressure of 100 psf obtained with air as the test medium are shown in figures 21 and 22. Figures 8, 14, 19, and 21 show variations of the wing spar deflections of shapes for various angles of attack and Mach numbers; the remainder of the figures in each group show variations of wing spar deflections for various control surface deflections

at angles of attack of approximately  $0^\circ$  and  $2^\circ$ . The variations of the front and rear spar shapes with angle of attack and control surface deflections (figs. 8 through 22) show the expected characteristic shape typical of a similar cantilever beam. Generally, the spar deflections along the span increased as angle of attack and control surface deflection were increased in the range of test conditions. The expected peak deflections occurred at the spar tips. The influence of control surface deflection on the spar shapes was small compared with that of angle of attack. The influence of control surface deflection in some tests was smaller than that of the unsteady motion of the wing. A typical indication of this condition is shown in figures 13(a) and 13(b) where the magnitude of the vertical deflections does not necessarily increase with control surface deflection (angle of attack of  $0^\circ$  and control surface deflections from  $-2^\circ$  to  $-1^\circ$  and  $4^\circ$  to  $6^\circ$ ).

Variations of the outboard chordwise target vertical positions (targets 1002 and 1004) with angle of attack and control surface deflection are shown in figures 23 through 25 and figures 26 through 28, respectively, for dynamic pressures of 100, 200, and 300 psf. These plots are companion ones of the results in figures 8 through 23 and are generated to show the linearity of the spar tip deflection with angle of attack and control surface deflection. Variations of the spar tip deflection with angle of attack and control surface deflection were somewhat linear for the ranges of test conditions. The scatter in the results for control surface deflection indicates an effect of occasional random deflection errors mentioned in the discussion of figures 8 through 22.

### Effect of Dynamic Pressure

The effect of dynamic pressure on the average tip deflection of the two wing spars relative to the wind-off test condition is indicated in the results presented in figure 29. The wingtip deflection was approximated as the average deflection of targets 1002 and 1004. The data show variations of the average tip deflection of the wing spars with dynamic pressure for angles of attack of  $-1^\circ$ ,  $0^\circ$ , and  $1^\circ$  at Mach numbers of 0.700, 0.800, and 0.850 and with control surface deflection of  $0^\circ$ . The data (fig. 29) show that the wingtip deflection increases with dynamic pressure as it was varied from about 40 to 300 psf. The variations of wingtip deflection with dynamic pressure indicate that for certain conditions, the wingtip deflection may approach maximum or asymptotic values at high dynamic pressures. Such a maximum value of wingtip deflection is indicated for an angle of attack of  $1^\circ$  at Mach numbers of 0.800 and 0.850. Although

dynamic pressure increased wingtip deflection, as expected, this effect was accentuated by increasing the angle of attack.

### Effect of Mach Number

The effect of Mach number on the average wing spar tip deflection of the two wing spars relative to the wind-off test condition is indicated in the results presented in figure 30. The data of figure 30 show that for a given Mach number the angle of attack has a significant uniform effect. The data of figure 30 also show that Mach number has an insignificant effect on the wingtip deflection up to a value of about 0.800; above this value, the wingtip deflection may increase or decrease depending on angle of attack. Figure 30(a) for which the dynamic pressure is 100 psf shows that wingtip deflection increased with Mach number regardless of the angle of attack but the trend is inconsistent for the higher dynamic pressure of 200 psf as shown in figure 30(b).

### Concluding Remarks

Photogrammetric measurements of the static (quasi-static) wing surface deflections for a flexible aeroelastic supercritical research wing are presented herein. Wing deflection data were obtained at Mach numbers up to 0.900, angles of attack in the range from  $-2^\circ$  to  $4^\circ$ , control surface deflections in the range from  $-8^\circ$  to  $8^\circ$ , and dynamic pressures in the range from 42 psf to 312 psf.

A comparison of photogrammetric and cathetometric measurements of wingtip deflection shows very good agreement. A graphical overview of the photogrammetric measurements shows significant variations of the wing spars and wingtip vertical deflections. The trends of the variations were quite consistent over the range of test conditions. There were significant variations of wingtip deflection with dynamic pressure that increased with angle of attack. The data indicated the development of a possible maximum or asymptotic value of wingtip deflection in the range of dynamic pressures from about 200 to 300 psf. The effect of Mach number on the wingtip deflection was generally insignificant for Mach numbers up to 0.800. A trend toward larger wingtip deflections was indicated for Mach numbers above 0.800 at the lower dynamic pressure of 100 psf. However, this effect of Mach number at a dynamic pressure of 200 psf was not as consistent.

NASA Langley Research Center  
Hampton, VA 23665-5225  
September 26, 1990

### References

1. Hess, R. W.; Wynne, E. C.; and Cazier, F. W., Jr.: *Static and Unsteady Pressure Measurements on a 50 Degree Clipped Delta Wing at M = 0.9*. NASA TM-83297, 1982.
2. Sandford, M. C.; Ricketts, R. H.; Cazier, F. W., Jr.; and Cunningham, H. J.: Transonic Unsteady Airloads on an Energy Efficient Transport Wing With Oscillating Control Surfaces. *J. Aircr.*, vol. 18, no. 7, July 1981, pp. 557-561.
3. Ricketts, Rodney H.; Sandford, Maynard C.; Seidel, David A.; and Watson, Judith J.: Transonic Pressure Distributions on a Rectangular Supercritical Wing Oscillating in Pitch. *J. Aircr.*, vol. 21, no. 8, Aug. 1984, pp. 576-582.
4. Sandford, Maynard C.; Seidel, David A.; Eckstrom, Clinton V.; and Spain, Charles V.: Geometrical and Structural Properties of an Aeroelastic Research Wing. NASA TM-4110, 1989.
5. Seidel, David A.; Sandford, Maynard C.; and Eckstrom, Clinton V.: Measured Unsteady Transonic Aerodynamic Characteristics of an Elastic Supercritical Wing. *J. Aircr.*, vol. 24, no. 4, Apr. 1987, pp. 225-230.
6. Seidel, David A.; Eckstrom, Clinton V.; and Sandford, Maynard C.: Investigation of Transonic Region of High Dynamic Response Encountered on an Elastic Supercritical Wing. *Technical Papers, Part 2A, 28th Structures, Structural Dynamics and Materials Conference and AIAA Dynamics Specialists Conference*, Apr. 1987, pp. 66-75. (Available as AIAA-87-0735.)
7. Byrdsong, Thomas A.; and Brooks, Cuyler W., Jr.: *Wind-Tunnel Investigation of Longitudinal and Lateral-Directional Stability and Control Characteristics of a 0.237-Scale Model of a Remotely Piloted Research Vehicle With a Thick, High-Aspect-Ratio Supercritical Wing*. NASA TM-81790, 1980.
8. Reed, Wilmer H., III: *Aeroelasticity Matters: Some Reflections on Two Decades of Testing in the NASA Langley Transonic Dynamics Tunnel*. NASA TM-83210, 1981.
9. Brown, Duane C.: *Application of Close-Range Photogrammetry to Measurements of Structures in Orbit*, Volumes 1 and 2. GSI Tech. Rep. No. 80-012 (Contract No. MOM7DNS-895942), Geodetic Services Inc., Sept. 15, 1980.
10. Brown, Duane C.: STARS (Simultaneous Triangulation And Resection System), A Turnkey System for Close Range Photogrammetry. Presented at Symposium: Precision and Speed in Close Range Photogrammetry (York, England), Sept. 1982.
11. Ross, R.; and Rohne, P. B.: The Character of Flow Unsteadiness and Its Influence on Steady State Transonic Wind Tunnel Measurements. *Windtunnel Design and Testing Techniques*, AGARD-CP-174, 1976, pp. 45-1-45-5.

Table 1. Spatial Coordinates of Target Locations on Wing Lower Surface  
in Tunnel Axis System

[All coordinates are in inches]

Target	$x_s$	$y_s$	$z_s^a$	Target	$x_s$	$y_s$	$z_s^a$
101	256.329	40.470	57.918	601	281.550	87.052	56.333
102	259.464	39.067	57.344	602	283.416	86.221	55.995
103				603	286.047	85.048	55.883
104	267.214	35.600	57.258	604	288.740	83.848	56.046
105	271.163	33.838	57.849	605	290.969	82.855	56.457
106				606	293.700	81.637	56.942
b 107	276.026	31.668	58.503	701	286.899	96.930	55.662
b 108	278.925	30.374	58.420	702	288.494	96.220	55.328
201	262.163	51.243	57.880	703	290.869	95.161	55.210
202	265.009	49.975	57.514	704	293.299	94.078	55.320
203	268.557	48.364	57.433	705			
204	272.195	46.737	57.656	b 706	295.752	92.949	55.752
205	274.206	45.837	57.975	b 707	297.777	92.082	56.132
206				b 801	298.505	93.948	55.977
b 207	278.225	44.046	58.675	901	290.781	104.389	55.335
b 208	280.617	42.979	58.661	902	292.589	104.283	54.757
301	277.437	50.676	58.230	903	295.192	104.228	54.569
302	280.996	49.090	58.701	904	297.821	104.223	54.574
401	268.944	63.767	57.498	905			
402	271.447	62.652	57.144	b 906	300.521	104.223	54.860
403	274.682	61.210	57.070	b 907	302.447	104.047	55.137
404	277.992	59.735	57.359	1001	293.212	108.591	54.851
405	280.732	58.514	57.908	1002	294.983	108.998	54.421
406	284.090	57.017	58.385	1003	297.466	108.998	54.229
501	275.247	75.410	56.981	1004	299.949	108.998	54.215
502	277.432	74.437	56.643	1005	301.963	108.998	54.393
503	280.365	73.129	56.549	1006	304.379	108.998	54.721
504	283.366	71.792	56.769				
505	285.850	70.684	57.256				
506	288.895	69.327	57.746				

<sup>a</sup>Estimated 1g value.

<sup>b</sup>Targets on control surfaces.

Table 2. Corrected Spatial Coordinates of Target Locations on Wing Lower Surface

[All coordinates are in inches]

Target	$x_s$	$y_s$	$z_s$	Target	$x_s$	$y_s$	$z_s$
a101	255.480	40.507	60.904	601	280.511	86.830	59.042
b102	258.641	39.109	60.405	602	282.378	86.000	58.876
b103	263.393	37.023	60.219	603	285.043	84.908	58.860
a104	266.405	35.675	60.416	604	287.754	83.792	59.160
a105	270.375	33.867	61.022	605	290.036	82.900	59.636
b106	273.771	32.321	61.522	606	292.784	81.788	59.855
c107	275.159	31.670	61.603	701	285.837	96.627	58.307
c108	278.070	30.395	61.426	702	287.423	95.987	58.176
201	261.293	51.310	60.836	703	289.839	94.966	58.180
202	264.164	50.026	60.542	b704	292.349	93.948	58.433
203	267.699	48.446	60.498	b705	293.855	93.289	58.728
204	271.458	46.783	60.875	c706	294.798	92.960	58.950
205	273.309	45.940	61.215	c707	296.868	92.049	59.087
b206	275.933	44.899	61.660	c801	297.586	93.930	58.939
c207	277.303	44.193	61.779	901	289.789	104.190	57.731
c208	279.696	43.157	61.643	902	291.532	104.166	57.585
301	276.578	50.746	61.426	903	294.148	104.105	57.508
302	280.062	49.179	61.731	b904	296.757	104.107	57.664
401	268.018	63.769	60.389	b905	298.466	104.123	57.935
402	270.484	62.676	60.146	c906	299.395	104.037	58.055
403	273.738	61.239	60.117	c907	301.383	104.008	58.155
404	277.094	59.807	60.508	1001	292.293	108.825	57.365
405	279.825	58.581	61.084	1002	293.871	108.790	57.214
406	283.171	57.127	61.351	a1003	296.405	108.831	57.160
501	274.348	75.278	59.773	1004	298.799	108.910	57.284
502	276.475	74.365	59.576	1005	300.827	108.929	57.583
503	279.417	73.080	59.574	1006	303.276	108.856	57.676
504	282.389	71.785	59.903				
505	284.929	70.699	60.443				
506	287.970	69.400	60.683				

<sup>a</sup>Bundle adjustment control points.<sup>b</sup>Targets added after self-calibration.<sup>c</sup>Targets located on control surfaces.

Table 3. rms Estimated Measurement Precision for Target Spatial Coordinates  
 [All coordinates are in inches]

Target	$X_{S, \text{rms}}$	$Y_{S, \text{rms}}$	$Z_{S, \text{rms}}$	Target	$X_{S, \text{rms}}$	$Y_{S, \text{rms}}$	$Z_{S, \text{rms}}$
<sup>a</sup> 101	0.0045	0.0050	0.0048	601	0.0182	0.0170	0.0046
<sup>a</sup> 102				602	0.0182	0.0170	0.0043
<sup>b</sup> 103				603	0.0183	0.0169	0.0041
104	0.0030	0.0037	0.0035	604	0.0183	0.0169	0.0041
<sup>a</sup> 105				605	0.0185	0.0170	0.0043
<sup>b</sup> 106				606	0.0187	0.0171	0.0046
<sup>c</sup> 107	0.0041	0.0051	0.0049	701	0.0220	0.0205	0.0046
<sup>c</sup> 108	0.0049	0.0060	0.0059	702	0.0220	0.0205	0.0044
201	0.0059	0.0061	0.0046	703	0.0220	0.0205	0.0042
202	0.0055	0.0056	0.0040	<sup>b</sup> 704	0.0221	0.0205	0.0043
203	0.0052	0.0052	0.0036	<sup>c</sup> 705	0.0222	0.0205	0.0045
204	0.0052	0.0052	0.0035	<sup>c</sup> 706	0.0223	0.0206	0.0048
<sup>b</sup> 205	0.0053	0.0053	0.0037	<sup>c</sup> 707	0.0229	0.0212	0.0048
<sup>c</sup> 206				901	0.0248	0.0233	0.0048
<sup>c</sup> 207	0.0057	0.0058	0.0043	902	0.0250	0.0234	0.0046
<sup>c</sup> 208	0.0061	0.0062	0.0049	903	0.0254	0.0237	0.0046
301	0.0071	0.0067	0.0039	<sup>b</sup> 904	0.0257	0.0241	0.0047
302	0.0074	0.0071	0.0044	<sup>c</sup> 905	0.0261	0.0244	0.0049
401	0.0098	0.0094	0.0047	<sup>c</sup> 906	0.0265	0.0247	0.0052
402	0.0096	0.0092	0.0042	1001	0.0265	0.0249	0.0048
403	0.0096	0.0090	0.0039	1002	0.0267	0.0251	0.0047
404	0.0096	0.0090	0.0038	<sup>a</sup> 1003	0.0271	0.0254	
405	0.0098	0.0090	0.0040	1004	0.0275	0.0257	0.0048
406	0.0101	0.0093	0.0045	1005	0.0278	0.0260	0.0050
501	0.0139	0.0131	0.0046	1006	0.0282	0.0263	0.0054
502	0.0139	0.0130	0.0042				
503	0.0139	0.0129	0.0039				
504	0.0139	0.0129	0.0039				
505	0.0141	0.0129	0.0041				
506	0.0143	0.0131	0.0046				

<sup>a</sup>Bundle adjustment control points

<sup>b</sup>Targets added after self-calibration

<sup>c</sup>Targets located on control surfaces

Table 4. Summary of Angle-of-Attack Calibration Results

Station parameters	Angle of attack, deg							Least-squares results		
	-2.0288	-1.0150	-0.0612	1.0349	2.0357	3.0510	4.0271	$a_1$	$a_0$	$C_{\text{cor}}$
Forward camera station										
$x_c$ , in. . . . .	261.1423	261.6075	262.0370	262.5255	262.9913	263.4311	263.8687	0.4508	262.0582	0.9999
$y_c$ , in. . . . .	-3.5917	-3.6370	-3.6448	-3.6088	-3.6057	-3.6202	-3.5936	0.0024	-3.6169	0.2531
$z_c$ , in. . . . .	31.5574	31.6652	31.8048	31.9645	32.0994	32.2561	32.4258	0.1439	31.8218	0.9983
$\psi$ , deg . . . . .	2.1495	1.8100	1.4963	1.1327	0.7821	0.4519	0.1127	-0.3365	1.4744	-0.9999
$\theta$ , deg . . . . .	18.6309	18.6742	18.6824	18.7162	18.7417	18.7462	18.7567	0.0205	18.6861	0.9722
$\phi$ , deg . . . . .	1.8746	0.8324	-0.2070	-1.3443	-2.4020	-3.4500	-4.5027	-1.0543	-0.2464	-0.9999
Aft camera station										
$x_c$ , in. . . . .	302.9109	303.3734	303.7989	304.2812	304.7209	305.0942	305.5056	0.4286	303.8065	0.9996
$y_c$ , in. . . . .	-6.3497	-6.3765	-6.3773	-6.3815	-6.3901	-6.4246	-6.4043	-0.0096	-6.3766	-0.8918
$z_c$ , in. . . . .	30.6329	31.5041	32.3214	33.2495	34.1697	35.0182	35.9238	0.8729	32.3759	0.9999
$\psi$ , deg . . . . .	-25.6405	-25.8889	-26.1203	-26.3855	-26.6297	-26.8240	-27.0622	-0.2344	-26.1271	-0.9995
$\theta$ , deg . . . . .	16.1339	15.6699	15.2693	14.7995	14.3135	13.8911	-13.4282	-0.4455	15.2376	-0.9998
$\phi$ , deg . . . . .	3.4554	2.4625	1.6067	0.5936	-0.3706	-1.2651	-2.1730	-0.9283	1.5557	-0.9999

Table 5. Wing Deflection Measurements for Typical Test Condition

$$\left[ \begin{array}{l} \text{Tab point} = 108; M = 0.791; q = 99.796 \text{ psf}; \\ \alpha = 1.024^\circ; \delta = -0.065^\circ \end{array} \right]$$

Target	X <sub>S</sub>	Y <sub>S</sub>	Z <sub>S</sub>	Target	X <sub>S</sub>	Y <sub>S</sub>	Z <sub>S</sub>
101	255.507	40.399	61.101	601	280.601	86.709	60.884
102	258.669	39.017	60.611	602	282.459	85.984	60.757
103	263.414	36.919	60.407	603	285.125	84.866	60.748
104	266.430	35.572	60.600	604	287.832	83.751	61.053
105	270.391	33.785	61.228	605	290.118	82.855	61.555
106	273.797	32.220	61.721	606	292.859	81.695	61.762
<sup>a</sup> 107	999.999	99.999	99.999	701	285.930	96.652	60.723
<sup>a</sup> 108	999.999	99.999	99.999	702	287.524	95.949	60.596
201	261.330	51.190	61.243	703	289.938	94.922	60.606
202	264.206	49.886	60.926	704	292.442	93.942	60.897
203	267.731	48.321	60.898	705	293.951	93.239	61.187
204	271.484	46.664	61.283	706	294.872	92.862	61.394
205	273.344	45.790	61.585	707	296.979	91.987	61.554
206	275.962	44.755	62.038	801	297.688	93.904	61.516
207	277.329	44.073	62.175				
208	279.721	43.017	62.027	901	289.890	104.200	60.605
301	276.610	50.607	61.944	902	291.641	104.103	60.476
302	280.091	49.062	62.267	903	294.265	104.054	60.477
401	268.076	63.628	61.162	904	296.865	104.061	60.679
402	270.534	62.555	60.923	905	298.585	104.060	60.994
403	273.780	61.153	60.901	906	299.510	104.073	61.166
404	277.129	59.690	61.286	907	301.487	103.952	61.284
405	279.869	58.452	61.858				
406	283.213	57.026	62.154	1001	292.418	108.764	60.477
501	274.405	75.226	61.061	1002	293.993	108.936	60.432
502	276.539	74.284	60.858	1003	296.534	108.821	60.392
503	279.487	72.953	60.849	1004	298.928	108.992	60.611
504	282.456	71.716	61.210	1005	300.927	108.892	60.944
505	284.981	70.622	61.751	1006	303.378	108.830	61.088
506	288.029	69.277	61.986				

<sup>a</sup>Target spatial coordinates were not available.

Table 6. Quasi-Steady Test Conditions for Wing Deflection Measurements

Tab point	M	q, psf	$\alpha$ , deg	$\delta$ , deg	Remarks
001	0.000	0.000	0.000	0.000	Wind-off zero
210	0.600	100.518	-2.014	0.008	$\alpha$ sweep
211	0.600	99.982	-1.029	-0.044	
212	0.600	100.400	0.023	-0.019	
213	0.600	99.805	1.019	0.006	
214	0.600	101.192	2.027	-0.018	
215	0.600	100.599	3.005	-0.013	
216	0.600	100.457	4.024	-0.009	
217	0.600	100.913	0.006	-7.979	$\delta$ sweep
218	0.600	102.756	0.006	-6.003	
219	0.600	101.851	0.004	-3.996	
220	0.600	100.887	0.005	-3.031	
221	0.600	101.218	0.005	-2.051	
222	0.600	100.827	0.004	-1.006	
223	0.600	99.957	0.004	-0.052	
224	0.600	101.487	0.004	1.001	
225	0.600	101.037	0.003	2.010	
226	0.600	101.390	0.003	3.001	
227	0.600	101.434	0.004	4.020	
228	0.600	101.204	0.003	5.983	
229	0.600	101.354	0.002	8.021	
230	0.600	101.028	2.000	-8.034	$\delta$ sweep
231	0.600	100.636	1.999	-5.963	
232	0.600	100.864	2.000	-4.042	
233	0.600	101.678	1.999	-2.991	
234	0.600	101.097	1.999	-1.966	
235	0.600	101.137	1.999	-1.003	
236	0.600	100.625	1.999	0.050	
237	0.600	100.979	1.999	1.042	
238	0.600	100.829	2.000	2.034	
239	0.600	100.958	1.999	3.027	
240	0.600	100.956	1.999	4.031	
241	0.600	100.381	1.999	6.042	
242	0.600	101.127	1.998	8.059	
148	0.700	99.441	-2.022	-0.083	$\alpha$ sweep
149	0.700	99.366	-1.023	-0.032	
150	0.700	100.149	-0.027	-0.073	
151	0.700	100.003	0.997	-0.004	
152	0.700	100.488	2.005	-0.045	
153	0.700	99.594	2.998	-0.069	
154	0.700	100.195	4.024	-0.066	

Table 6. Continued

Tab Point	M	q, psf	$\alpha$ , deg	$\delta$ , deg	Remarks
168	0.700	100.240	-0.008	-8.026	$\delta$ sweep
170	0.700	99.800	-0.009	-4.033	
172	0.700	100.371	-0.010	-2.027	
176	0.700	100.680	-0.010	2.017	
179	0.700	100.112	-0.010	3.990	
181	0.700	100.517	-0.011	8.022	
155	0.700	100.361	2.009	-8.014	$\delta$ sweep
156	0.700	100.978	2.009	-5.994	
157	0.700	100.284	2.009	-4.012	
159	0.700	100.092	2.009	-1.985	
161	0.700	100.121	2.009	0.021	
163	0.700	100.375	2.009	2.011	
165	0.700	99.718	2.008	4.037	
80	0.800	100.879	-2.003	-0.028	$\alpha$ sweep
81	0.800	100.473	-1.023	-0.050	
82	0.800	100.828	0.000	-0.039	
108	0.800	99.796	1.024	-0.065	
109	0.800	99.854	2.009	-0.063	
110	0.800	100.537	2.992	-0.063	
111	0.800	101.735	3.998	-0.064	
105	0.800	101.206	0.002	-8.001	$\delta$ sweep
106	0.800	100.103	0.001	-5.990	
107	0.800	99.419	0.001	-4.075	
86	0.800	100.395	0.001	-3.045	
87	0.800	101.471	0.000	-2.040	
88	0.800	99.910	0.000	-1.045	
90	0.800	100.106	-0.001	1.021	
91	0.800	100.268	0.000	1.984	
92	0.800	99.694	0.000	3.043	
94	0.800	100.093	-0.001	4.063	
95	0.800	98.901	-0.001	6.018	
96	0.800	100.250	-0.001	8.053	
115	0.800	101.305	2.009	-8.032	$\delta$ sweep
116	0.800	101.868	2.011	-6.025	
117	0.800	101.968	2.010	-4.027	
118	0.800	101.803	2.010	-2.981	
119	0.800	102.238	2.009	-2.030	
120	0.800	102.029	2.009	-1.035	
122	0.800	101.450	2.018	0.002	
123	0.800	101.049	2.018	1.026	
124	0.800	102.573	2.018	2.014	
125	0.800	102.273	2.018	3.020	

Table 6. Continued

Tab Point	M	q, psf	$\alpha$ , deg	$\delta$ , deg	Remarks
126	0.800	101.966	2.018	4.004	$\delta$ sweep
127	0.800	102.336	2.018	6.011	
128	0.800	101.803	2.018	8.027	
783	0.850	99.778	-2.008	0.033	$\alpha$ sweep
784	0.850	99.555	-1.019	0.026	
785	0.850	99.731	-0.003	0.013	
788	0.850	100.169	1.020	0.011	
789	0.850	100.344	1.998	0.025	
790	0.850	100.099	2.992	0.007	
791	0.850	100.160	4.027	0.000	
801	0.850	100.293	-0.001	-3.043	$\delta$ sweep
802	0.850	100.137	0.000	-1.993	
803	0.850	100.860	-0.001	-1.037	
804	0.850	100.341	-0.001	1.031	
805	0.850	100.564	-0.001	2.003	
806	0.850	100.618	-0.001	3.021	
807	0.850	100.339	-0.001	6.041	
792	0.850	100.435	2.021	-6.068	$\delta$ sweep
793	0.850	100.334	2.020	-2.998	
794	0.850	100.743	2.020	-1.996	
795	0.850	100.994	2.021	-1.031	
796	0.850	100.334	2.020	0.993	
797	0.850	100.735	2.019	2.057	
798	0.850	100.396	2.019	3.057	
799	0.850	100.588	2.019	6.011	
268	0.880	100.628	-0.023	-7.998	$\delta$ sweep
270	0.880	100.401	-0.023	-4.003	
272	0.880	100.143	-0.023	-2.981	
273	0.880	100.873	-0.024	-1.996	
274	0.880	100.538	-0.024	-1.037	
276	0.880	100.771	-0.024	1.027	
277	0.880	100.642	-0.024	2.032	
278	0.880	100.265	-0.024	2.993	
280	0.880	101.182	-0.024	3.998	
281	0.880	101.251	-0.024	6.026	
283	0.880	101.093	2.025	-4.004	$\delta$ sweep
284	0.880	99.964	2.026	-3.004	
285	0.880	99.799	2.024	-1.983	
286	0.880	100.577	2.024	-1.003	
287	0.880	101.147	2.024	1.011	
288	0.880	101.228	2.023	2.071	
289	0.880	101.516	2.024	2.988	

Table 6. Continued

Tab Point	M	q, psf	$\alpha$ , deg	$\delta$ , deg	Remarks
290	0.880	101.144	2.024	3.987	$\delta$ sweep
291	0.880	101.085	2.023	6.002	
292	0.880	101.167	2.023	7.987	
293	0.880	100.972	2.024	0.048	
476	0.600	200.356	-2.032	-0.052	$\alpha$ sweep
477	0.600	199.231	-1.018	-0.025	
479	0.600	199.838	1.006	-0.014	
481	0.600	200.093	2.011	-0.035	
548	0.600	200.334	0.008	-5.990	$\delta$ sweep
567	0.600	202.296	-0.021	-1.984	
568	0.600	202.321	-0.023	-1.010	
570	0.600	202.380	-0.023	1.077	
572	0.600	203.313	-0.023	2.030	
573	0.600	203.768	-0.023	3.050	
574	0.600	203.612	-0.025	5.972	
482	0.600	199.566	2.021	-5.994	$\delta$ sweep
483	0.600	200.161	2.020	-2.987	
484	0.600	199.282	2.019	-2.019	
485	0.600	200.379	2.019	-1.055	
486	0.600	199.522	2.019	1.048	
487	0.600	198.999	2.018	2.027	
446	0.700	200.791	-2.012	-0.048	$\alpha$ sweep
449	0.700	200.373	-1.032	-0.052	
450	0.700	199.582	0.015	-0.060	
451	0.700	200.345	1.021	-0.056	
452	0.700	200.136	2.004	-0.050	
465	0.700	199.957	-0.014	-6.015	$\delta$ sweep
466	0.700	200.971	0.008	-3.023	
467	0.700	199.635	0.006	-2.008	
468	0.700	201.693	0.006	-1.041	
469	0.700	201.081	0.006	1.037	
471	0.700	200.462	0.005	2.002	
473	0.700	201.172	0.005	3.032	
474	0.700	200.870	0.004	6.024	
453	0.700	199.792	2.006	-6.018	$\delta$ sweep
455	0.700	201.403	2.005	-3.030	
456	0.700	201.251	2.005	-2.029	
459	0.700	199.607	2.029	1.027	
460	0.700	200.688	2.028	2.030	
461	0.700	200.384	2.028	3.011	
462	0.700	200.494	2.028	6.008	

Table 6. Continued

Tab Point	M	q, psf	$\alpha$ , deg	$\delta$ , deg	Remarks
423	0.800	200.865	-2.029	-0.055	
424	0.800	199.907	-1.030	-0.037	
425	0.800	201.393	0.001	-0.024	
426	0.800	200.616	1.026	-0.035	
427	0.800	200.337	2.024	-0.028	
437	0.800	204.280	0.011	-6.032	$\delta$ sweep
438	0.800	203.288	0.011	-2.994	
439	0.800	203.492	0.010	-2.008	
440	0.800	202.202	0.010	-1.007	
441	0.800	201.853	0.009	1.015	
442	0.800	204.732	0.010	2.012	
443	0.800	203.387	0.010	3.030	
444	0.800	204.540	0.009	6.036	
428	0.800	202.119	2.024	-5.963	$\delta$ sweep
429	0.800	201.354	2.024	-3.042	
431	0.800	202.829	2.024	-2.024	
432	0.800	199.750	2.023	-1.065	
433	0.800	201.244	2.023	1.023	
434	0.800	200.533	2.024	2.032	
435	0.800	203.957	2.021	3.064	
436	0.800	203.772	2.022	6.042	
911	0.850	199.727	-2.022	-0.048	$\alpha$ sweep
912	0.850	200.654	-1.032	-0.039	
913	0.850	200.556	0.006	-0.068	
914	0.850	200.871	1.005	-0.070	
915	0.850	202.492	2.021	-0.065	
916	0.850	202.039	-0.011	-6.062	$\delta$ sweep
917	0.850	200.945	-0.012	-3.019	
918	0.850	201.597	-0.013	-2.009	
919	0.850	200.681	-0.013	-1.021	
920	0.850	202.207	-0.013	1.037	
921	0.850	200.895	-0.014	2.024	
922	0.850	199.740	-0.014	3.015	
923	0.850	203.088	-0.014	5.999	
924	0.850	202.528	2.020	-6.007	$\delta$ sweep
925	0.850	202.815	2.019	-3.024	
926	0.850	200.509	2.020	-2.033	
927	0.850	202.695	2.020	-1.010	
928	0.850	202.545	2.019	1.056	
929	0.850	200.369	2.019	2.020	
930	0.850	204.826	2.020	3.067	

Table 6. Continued

Tab Point	M	q, psf	$\alpha$ , deg	$\delta$ , deg	Remarks
931	0.850	202.482	2.019	5.979	$\delta$ sweep
932	0.850	202.730	2.019	0.056	
948	0.800	299.589	-1.036	0.029	$\alpha$ sweep
951	0.800	297.697	0.000	-0.048	
952	0.800	298.743	1.024	-0.044	
953	0.800	297.301	0.006	-3.005	$\delta$ sweep
955	0.800	299.726	0.015	-1.928	
957	0.800	295.817	0.014	-0.892	
958	0.800	298.955	0.011	2.993	
959	0.800	297.900	0.012	2.067	
960	0.800	298.602	0.011	0.964	
961	0.800	300.477	0.011	6.090	
977	0.800	103.502	-2.022	-0.072	$\alpha$ sweep in air
978	0.800	102.518	-1.019	0.049	
979	0.800	102.772	-0.009	-0.034	
980	0.800	102.729	1.009	-0.033	
981	0.800	102.983	2.017	-0.025	
982	0.800	103.579	2.968	-0.029	
983	0.800	103.658	3.996	-0.051	
1004	0.800	104.793	0.006	-6.004	$\delta$ sweep in air
1005	0.800	104.693	0.005	-3.039	
1006	0.800	104.757	0.005	-2.026	
1007	0.800	104.682	0.005	-1.036	
1008	0.800	104.854	0.004	1.019	
1009	0.800	105.420	0.004	2.001	
1010	0.800	105.108	0.004	2.975	
1011	0.800	105.001	0.004	6.016	
1012	0.800	105.217	2.015	-6.020	$\delta$ sweep in air
1013	0.800	105.121	2.015	-3.006	
1014	0.800	105.293	2.015	-2.039	
1015	0.800	105.501	2.014	-1.008	
1016	0.800	105.530	2.015	1.013	
1018	0.800	105.611	2.014	2.004	
1019	0.800	105.743	2.013	3.010	
1020	0.800	105.720	2.012	6.004	
665	0.700	100.443	-0.012	-0.013	Transition strips installed
667	0.750	111.908	-0.014	-0.021	
669	0.800	123.682	-0.016	-0.020	
671	0.850	135.351	-0.017	-0.030	
673	0.870	139.763	-0.018	-0.022	

Table 6. Concluded

Tab Point	M	q, psf	$\alpha$ , deg	$\delta$ , deg	Remarks
680	0.700	100.216	-0.010	-0.044	
685	0.750	111.773	-0.015	-0.034	
689	0.800	123.632	-0.013	-0.047	
691	0.850	133.431	-0.015	-0.043	Air data ↓

Table 7. Correlation of Graphic and Tabulated Results

Figure (a)	Tab point
8(aT)	Angle-of-attack variation: 001, 211, 212, 213, 214, 215, 216
8(bT)	001, 148, 149, 150, 151, 152, 153, 154
8(cT)	001, 80, 81, 82, 108, 109, 110, 111
8(dT)	001, 783, 784, 785, 788, 789, 790, 791
9(aT)	Control surface deflection variation: 001, 218, 219, 220, 221, 222, 223, 224, 225, 226, 227, 228, 229
9(bT)	001, 218, 219, 220, 221, 222, 223, 224, 225, 226, 227, 228, 229
9(cT)	001, 231, 232, 233, 234, 235, 236, 237, 238, 239, 240, 241, 242
9(dT)	001, 231, 232, 233, 234, 235, 236, 237, 238, 239, 240, 241, 242
10(aT)	001, 155, 156, 157, 159, 161, 163, 165
10(aB)	001, 155, 156, 157, 159, 161, 163, 165
10(bT)	001, 168, 170, 172, 176, 179, 181
10(bB)	001, 168, 170, 172, 176, 179, 181
11(a)	001, 82, 86, 87, 88, 90, 91, 92, 94, 95, 96, 105, 106, 107
11(b)	001, 82, 86, 87, 88, 90, 91, 92, 94, 95, 96, 105, 106, 107
11(c)	001, 115, 116, 117, 118, 119, 120, 122, 123, 124, 125, 126, 127, 128
11(d)	001, 115, 116, 117, 118, 119, 120, 122, 123, 124, 125, 126, 127, 128
12(aT)	001, 801, 802, 803, 804, 805, 806, 807
12(aB)	001, 801, 802, 803, 804, 805, 806, 807
12(bT)	001, 792, 793, 794, 795, 796, 797, 798, 799
12(bB)	001, 792, 793, 794, 795, 796, 797, 798, 799
13(a)	001, 270, 272, 273, 274, 276, 277, 278, 280, 281
13(b)	001, 270, 272, 273, 274, 276, 277, 278, 280, 281
13(c)	001, 283, 284, 285, 286, 287, 288, 289, 290, 291, 292
13(d)	001, 283, 284, 285, 286, 287, 288, 289, 290, 291, 292
14(aT)	Angle-of-attack variation: 001, 476, 477, 479, 481
14(bT)	001, 446, 449, 450, 451, 452
14(cT)	001, 423, 424, 425, 426, 427
14(dT)	001, 911, 912, 913, 914, 915

<sup>a</sup>T indicates top plot on page; B indicates bottom plot on page.

Table 7. Continued

Figure (a)	Tab point
15(aT)	Control surface deflection variation: 001, 548, 567, 568, 570, 572, 573, 574
15(aB)	001, 548, 567, 568, 570, 572, 573, 574
15(bT)	001, 482, 483, 484, 485, 486, 487
15(bB)	001, 482, 483, 484, 485, 486, 487
16(a)	001, 465, 466, 467, 468, 469, 471, 473, 474
16(b)	001, 465, 466, 467, 468, 469, 471, 473, 474
16(c)	001, 453, 455, 456, 459, 460, 461, 462
16(d)	001, 453, 455, 456, 459, 460, 461, 462
17(a)	001, 437, 438, 439, 440, 441, 442, 443, 444
17(b)	001, 437, 438, 439, 440, 441, 442, 443, 444
17(c)	001, 428, 429, 431, 432, 433, 434, 435, 436
17(d)	001, 428, 429, 431, 432, 433, 434, 435, 436
18(a)	001, 916, 917, 918, 919, 920, 921, 922, 923
18(b)	001, 916, 917, 918, 919, 920, 921, 922, 923
18(c)	001, 924, 925, 926, 927, 928, 929, 930, 931
18(d)	001, 924, 925, 926, 927, 928, 929, 930, 931
19(a)	Angle-of-attack variation: 001, 948, 951, 952
19(b)	001, 948, 951, 952
20(a)	Control surface deflection variation: 001, 953, 955, 957, 958, 959, 960, 961
20(b)	001, 953, 955, 957, 958, 959, 960, 961
21(a)	Angle-of-attack variation in air: 001, 977, 978, 979, 980, 981, 982, 983
21(b)	001, 977, 978, 979, 980, 981, 982, 983
22(a)	Control surface deflection variation in air: 001, 1004, 1005, 1006, 1007, 1008, 1009, 1010, 1011
22(b)	001, 1004, 1005, 1006, 1007, 1008, 1009, 1010, 1011
22(c)	001, 1012, 1013, 1014, 1015, 1016, 1018, 1019, 1020
22(d)	001, 1012, 1013, 1014, 1015, 1016, 1018, 1019, 1020

<sup>a</sup>T indicates top plot on page; B indicates bottom plot on page.

Table 7. Concluded

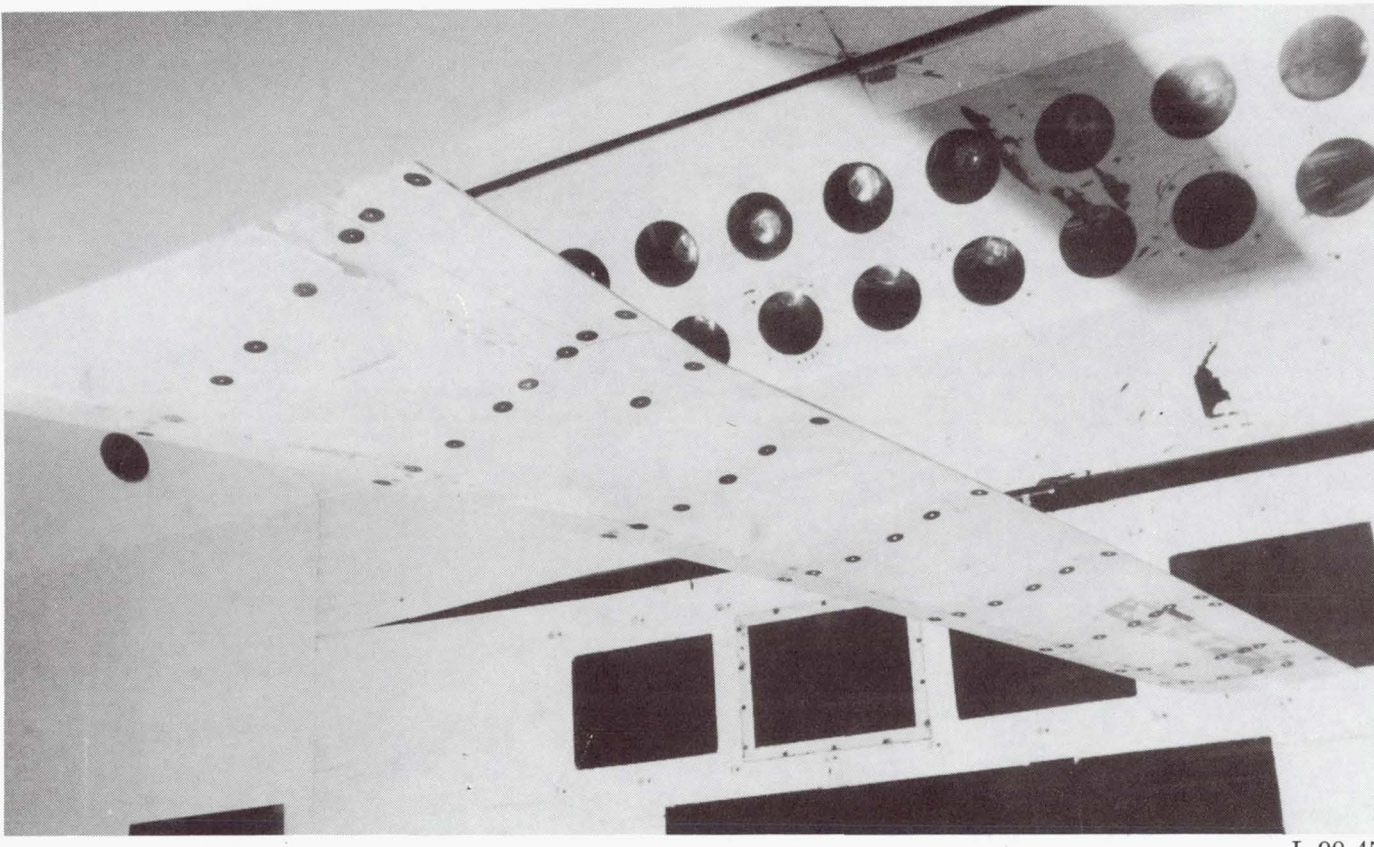
Figure	Tab point
23(a)	Angle-of-attack variation: 211, 212, 213, 214, 215, 216
23(b)	148, 149, 150, 151, 152, 153, 154
23(c)	80, 81, 82, 108, 109, 110, 111
23(d)	783, 784, 785, 788, 789, 790, 791
24(a)	476, 477, 479, 481
24(b)	446, 449, 450, 451, 452
24(c)	423, 424, 425, 426, 427
24(d)	911, 912, 913, 914, 915
25	948, 951, 952
26(a)	Control surface deflection variation: 217, 218, 219, 220, 221, 222, 223, 224, 225, 226, 227, 228, 229
26(b)	230, 231, 232, 233, 234, 235, 236, 237, 238, 239, 240, 241, 242
26(c)	168, 170, 172, 176, 179, 181, 155, 156, 157, 159, 161, 163, 165
26(d)	82, 86, 87, 88, 90, 91, 92, 94, 95, 96, 105, 106, 107
26(e)	115, 116, 117, 118, 119, 120, 122, 123, 124, 125, 126, 127, 128
27(a)	792, 793, 794, 795, 796, 797, 798, 801, 802, 803, 804, 805, 806, 807
27(b)	268, 270, 272, 273, 274, 276, 277, 278, 280, 281
27(c)	283, 284, 285, 286, 287, 288, 289, 290, 291, 292, 293
27(d)	548, 566, 567, 568, 570, 572, 573, 574, 482, 483, 484, 485, 486, 487
28	465, 466, 467, 468, 469, 471, 473, 474, 453, 455, 456, 459, 460, 461, 462
	428, 429, 431, 432, 433, 434, 435, 436, 437, 438, 439, 440, 441, 442, 443, 444
	916, 917, 918, 919, 920, 921, 922, 923, 924, 925, 926, 927, 928, 929, 930, 931, 932
	953, 955, 957, 958, 959, 960, 961



L-90-44

(a) Wing-fuselage assembly in test section.

Figure 1. Test configuration in Langley Transonic Dynamics Tunnel.



(b) Aft-camera view of test wing.

Figure 1. Concluded.

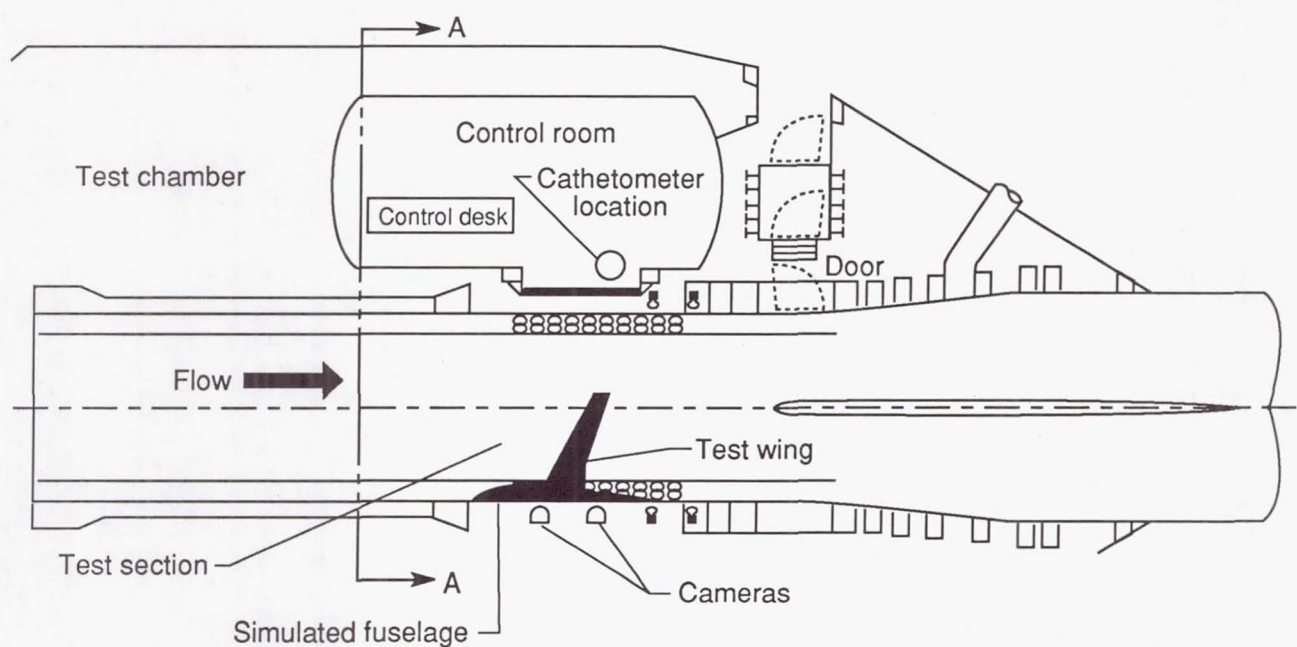
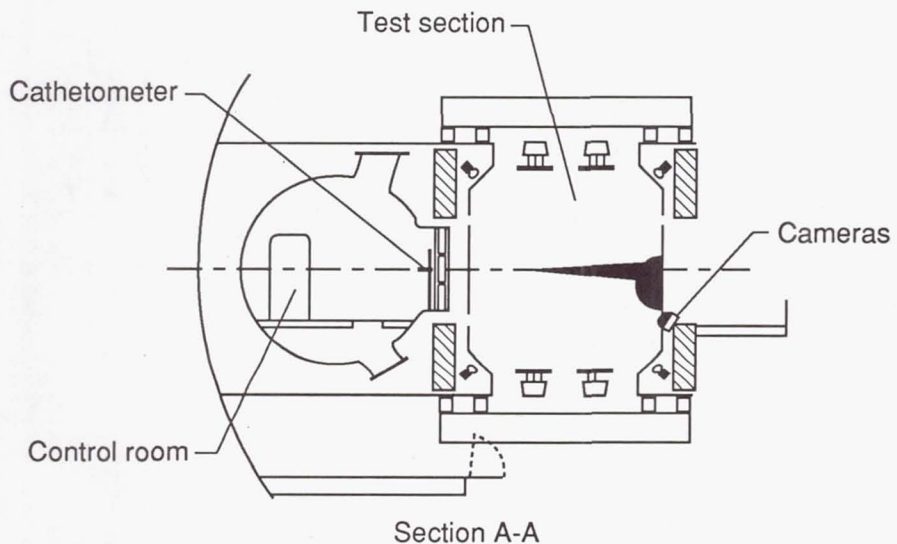


Figure 2. Plan view of wing-fuselage assembly, test section, and control room in test chamber of Langley Transonic Dynamics Tunnel.

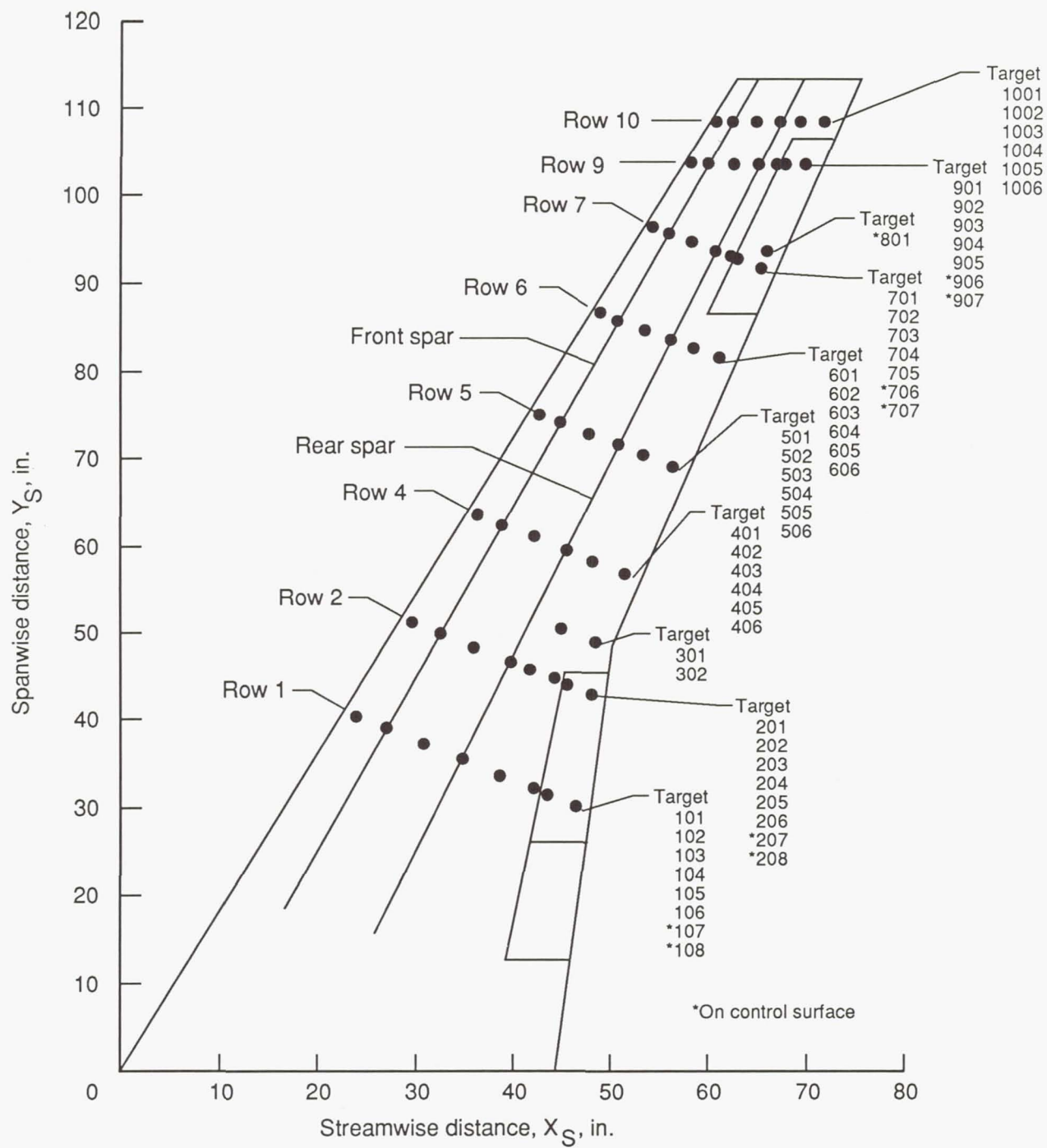


Figure 3. Wing planform showing relative location of targets on wing lower surface. Targets are numbered from leading edge to trailing edge.

Outboard control surface coordinates:

72.857,107.700  
69.712,107.700  
62.161,89.700  
65.962,89.700

(62.600,113.920) (75.240,113.920)

Outboard control

Inboard control surface coordinates:

49.759,45.000  
46.004,45.000  
47.387,25.670  
42.396,25.670  
40.031,13.000  
45.854,13.000

(50.190,48.530)

Inboard control

(0,0) (44.240,0.000)

Figure 4. Wing planform and control surfaces locations.

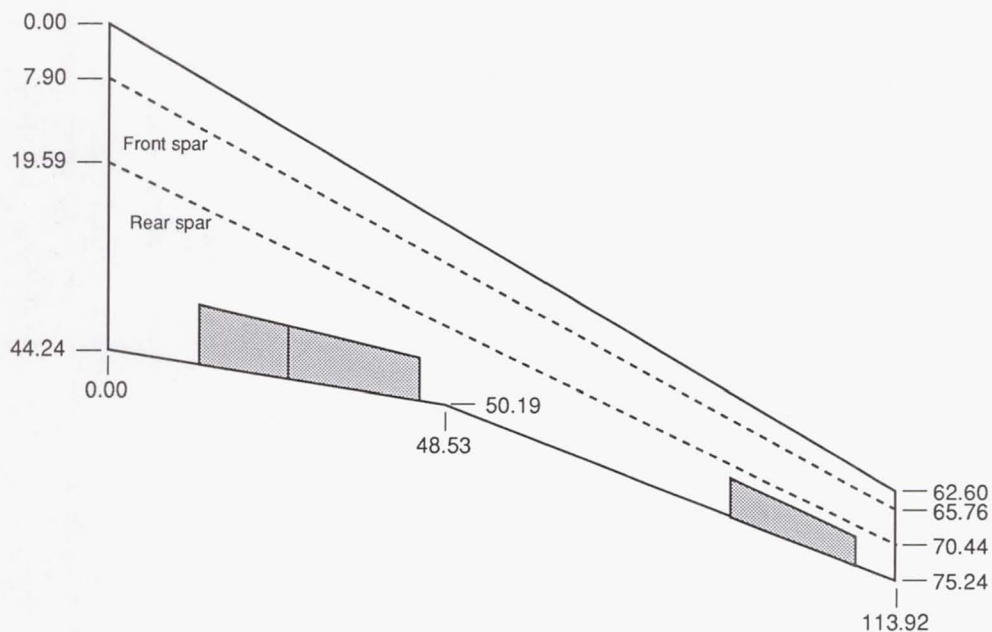


Figure 5. Front and rear spar centerline locations on wing planform. Dimensions are in inches.

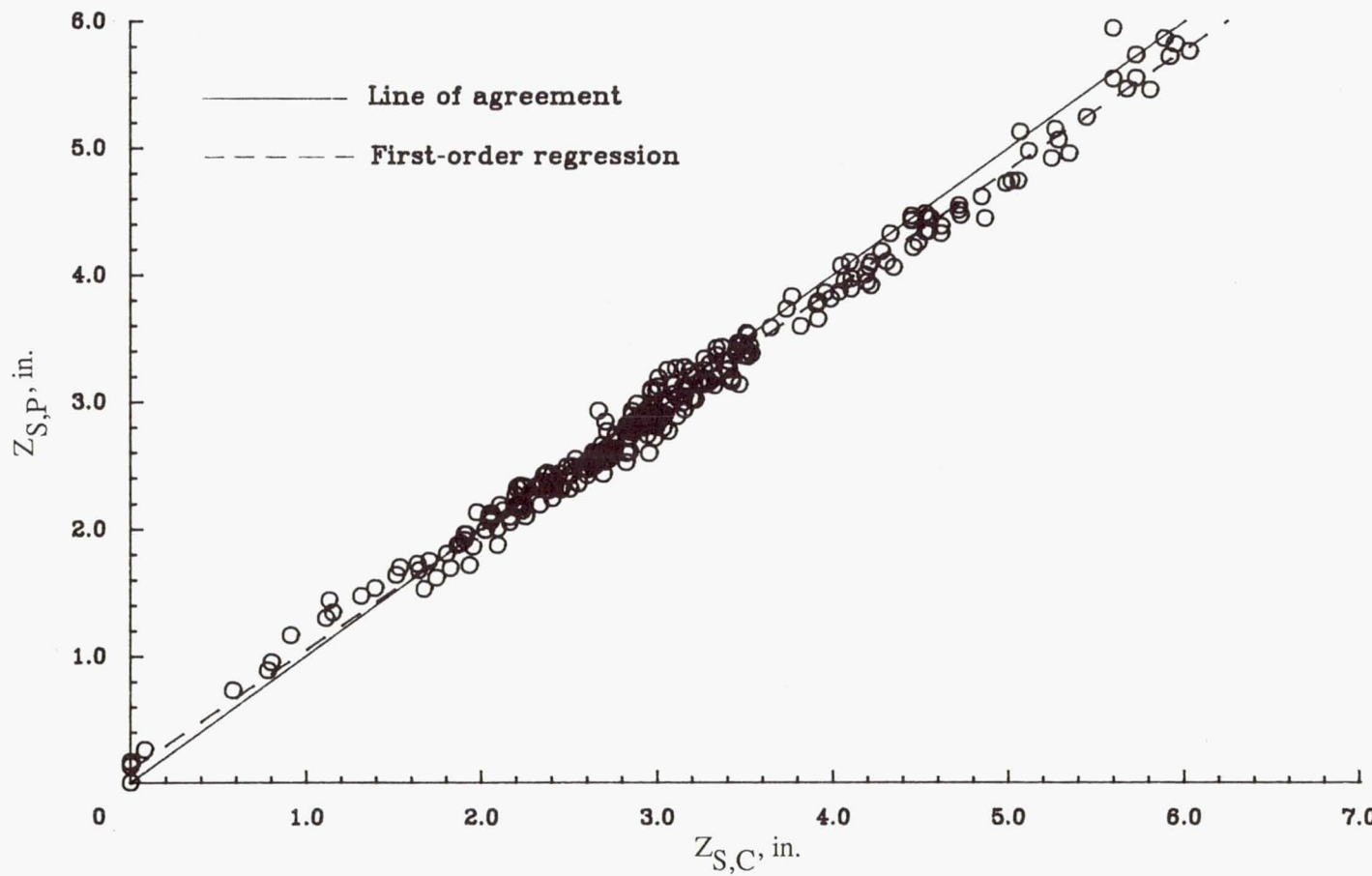
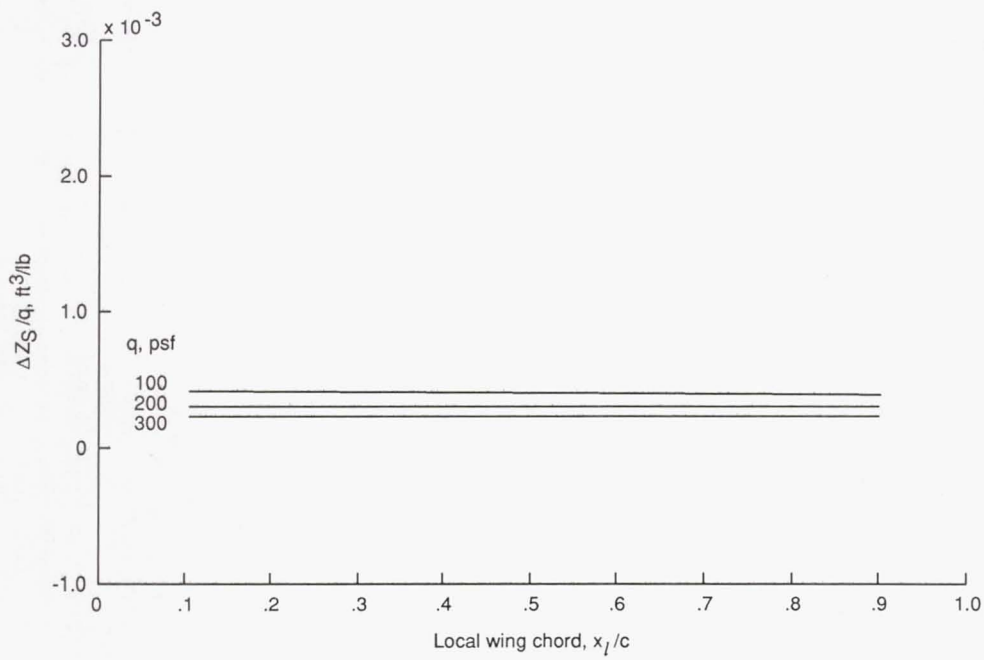
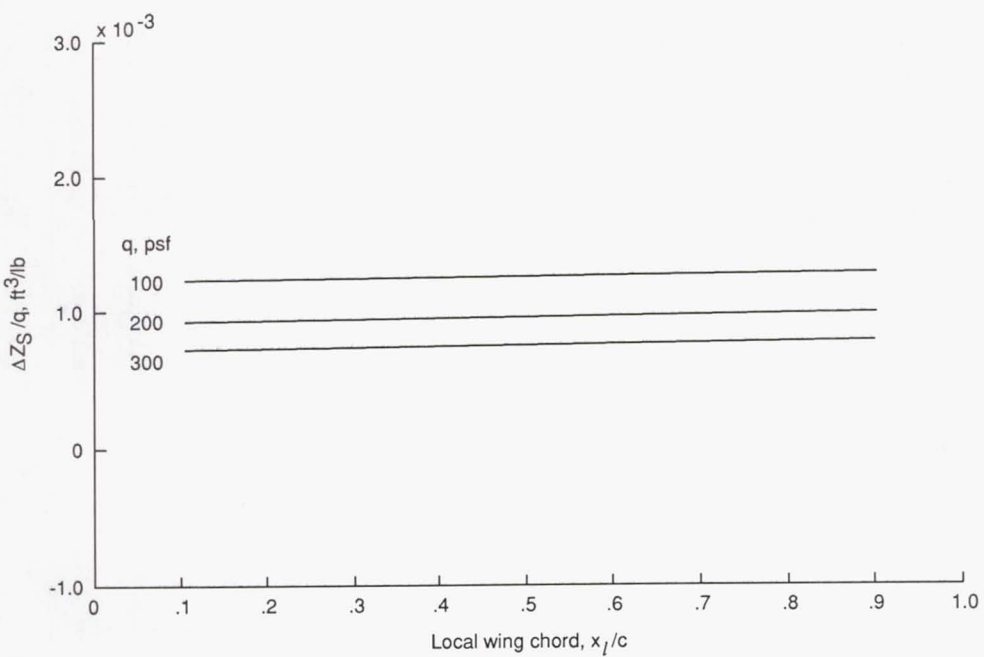


Figure 6. Photogrammetric and cathetometric results for wingtip measurements.  $a_0 = 0.10260$ ;  
 $a_1 = 0.94540$ ;  $C_{\text{cor}} = 0.99445$ .

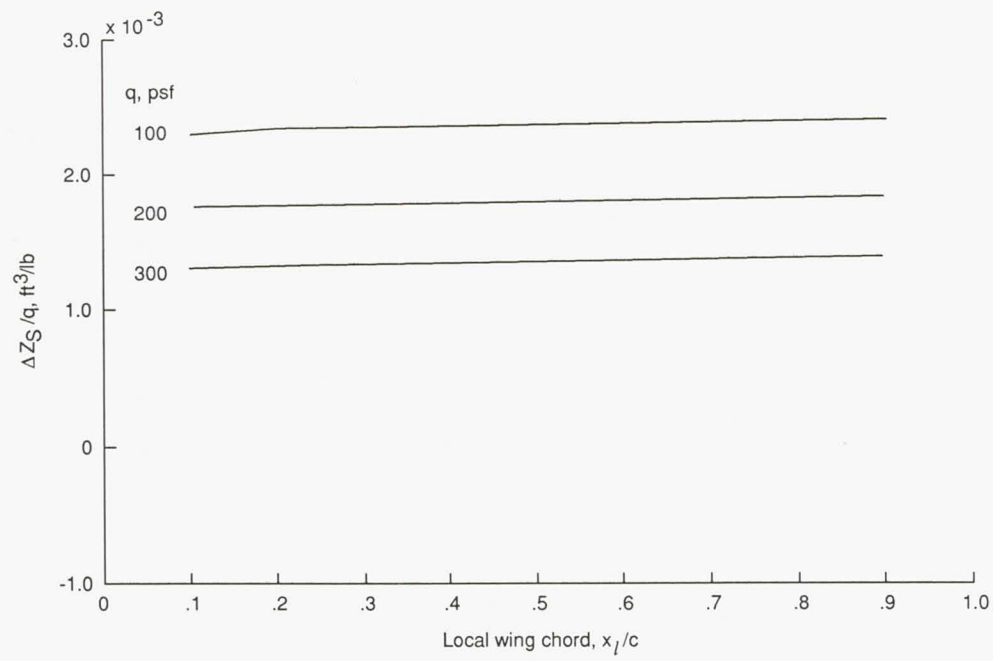


(a) Target row 2.

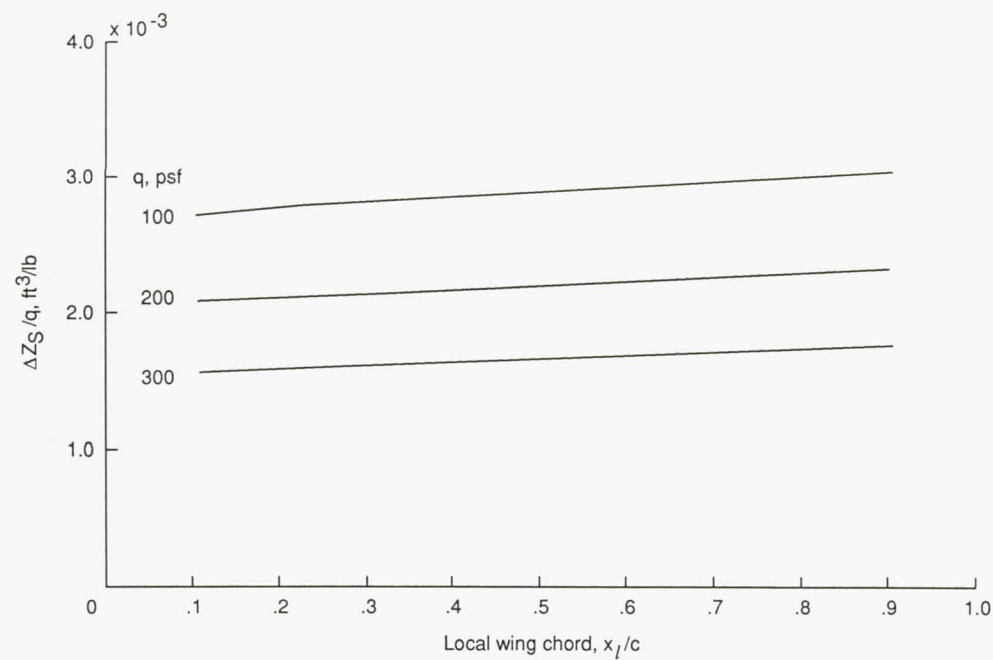


(b) Target row 5.

Figure 7. Effect of dynamic pressure on wing chordwise deflection at selected rows of targets along span at  $M = 0.850$  and  $\alpha = 1^\circ$ .

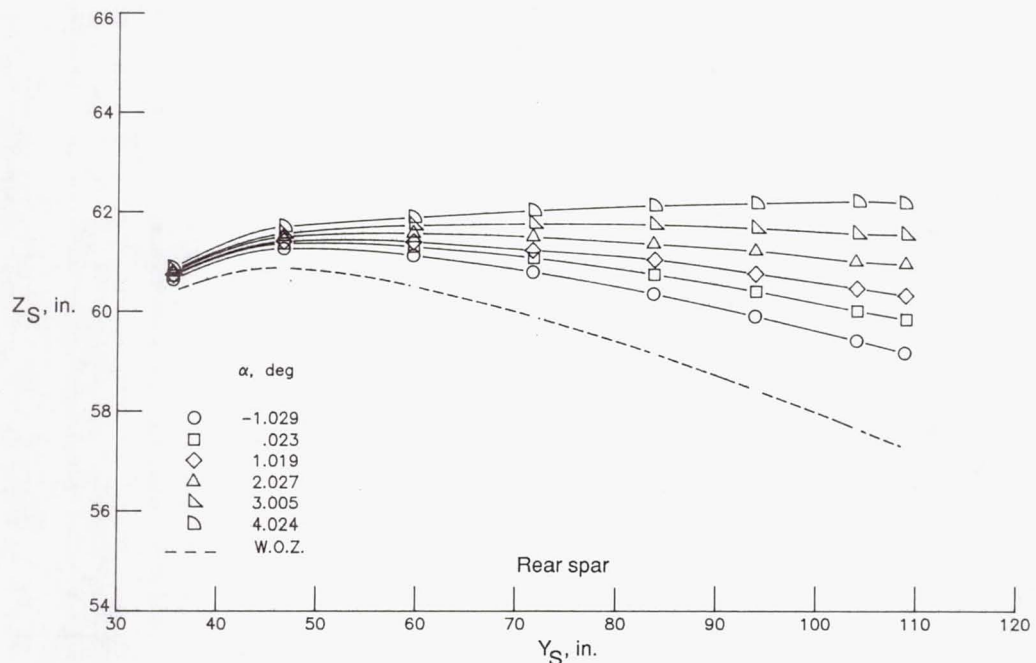
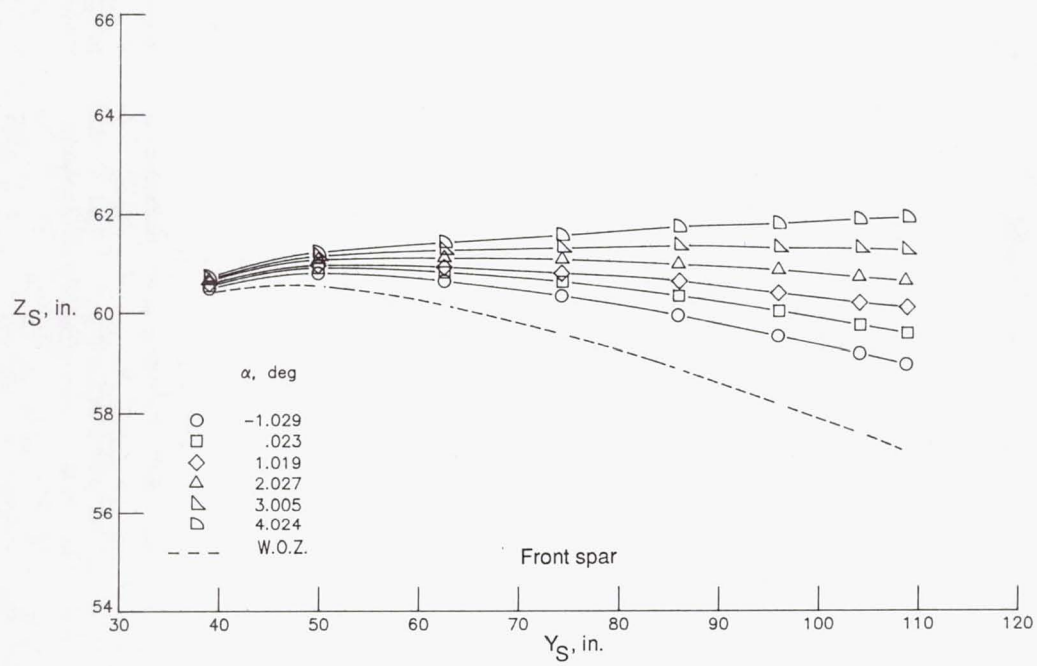


(c) Target row 7.



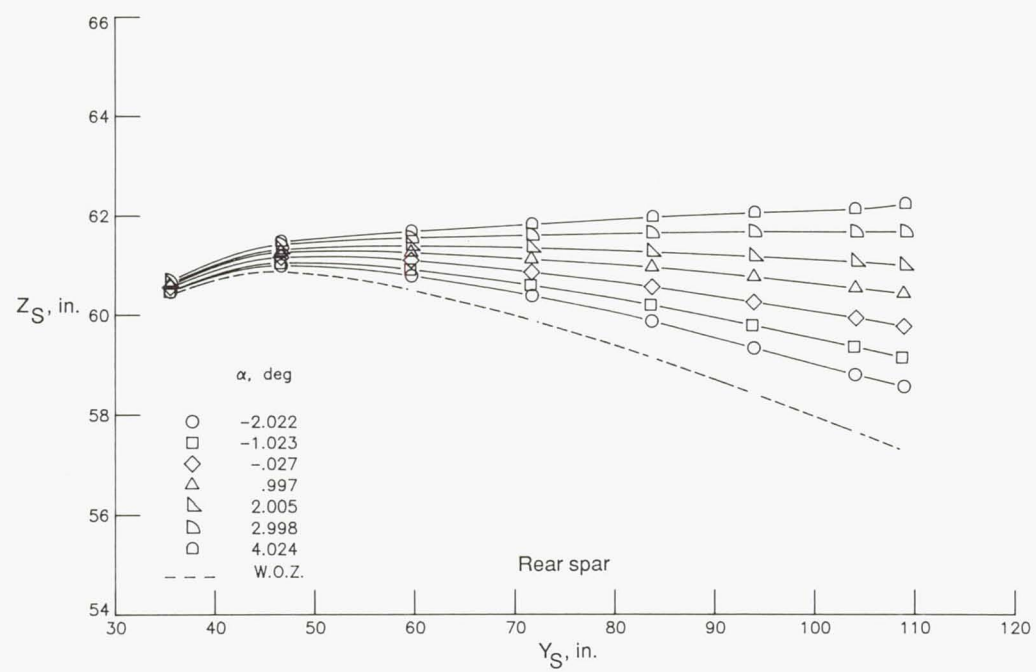
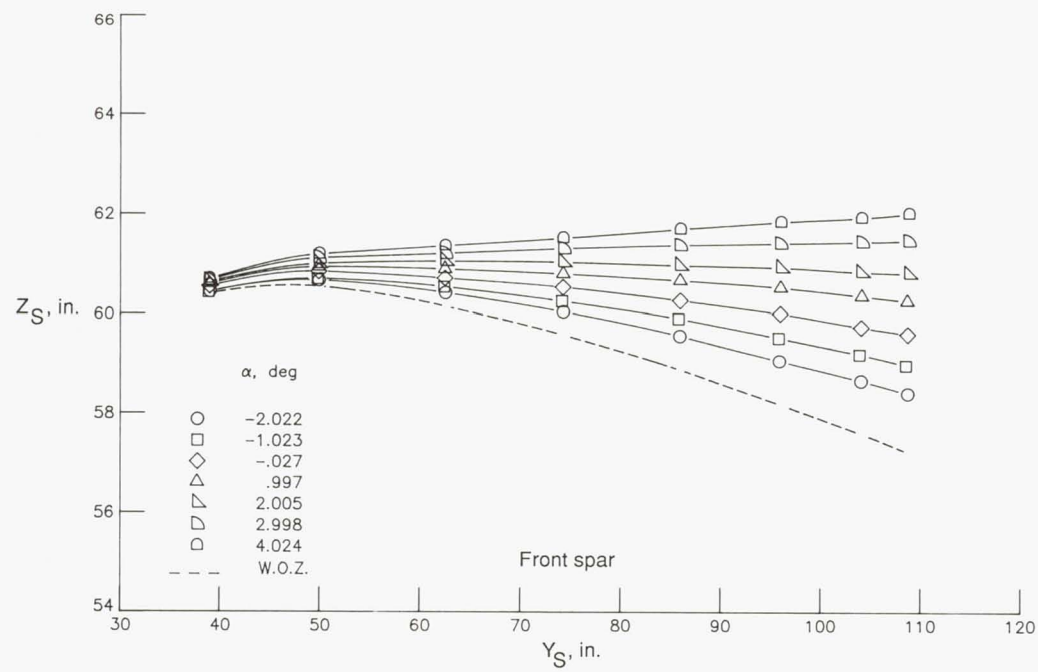
(d) Target row 9.

Figure 7. Concluded.



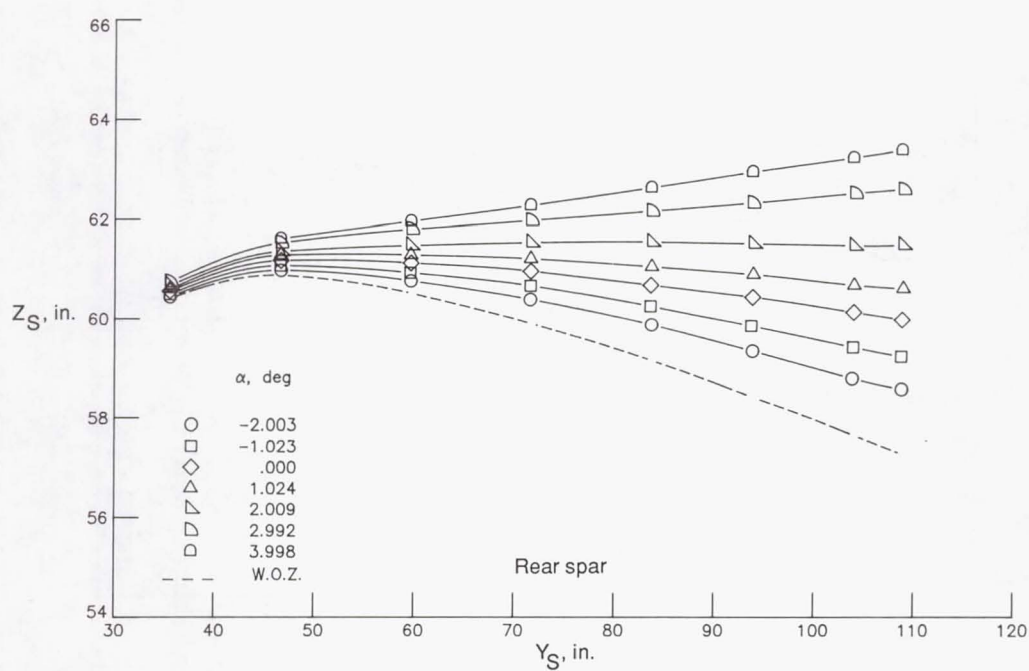
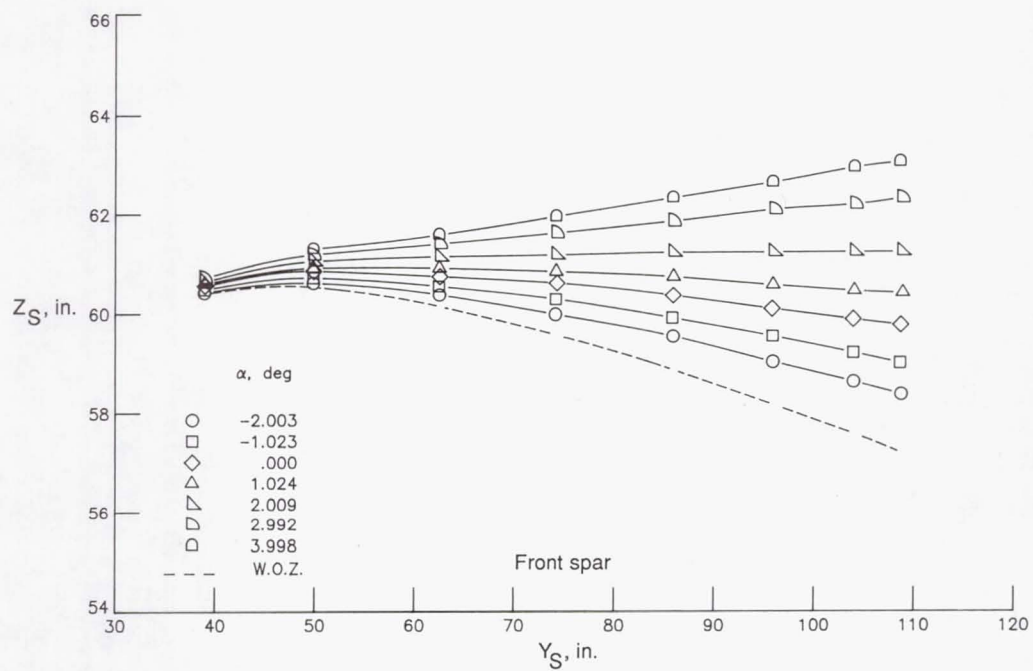
(a)  $M = 0.600$ .

Figure 8. Variation of wing front and rear spar shapes with angle of attack at four Mach numbers and  $q = 100$  psf.



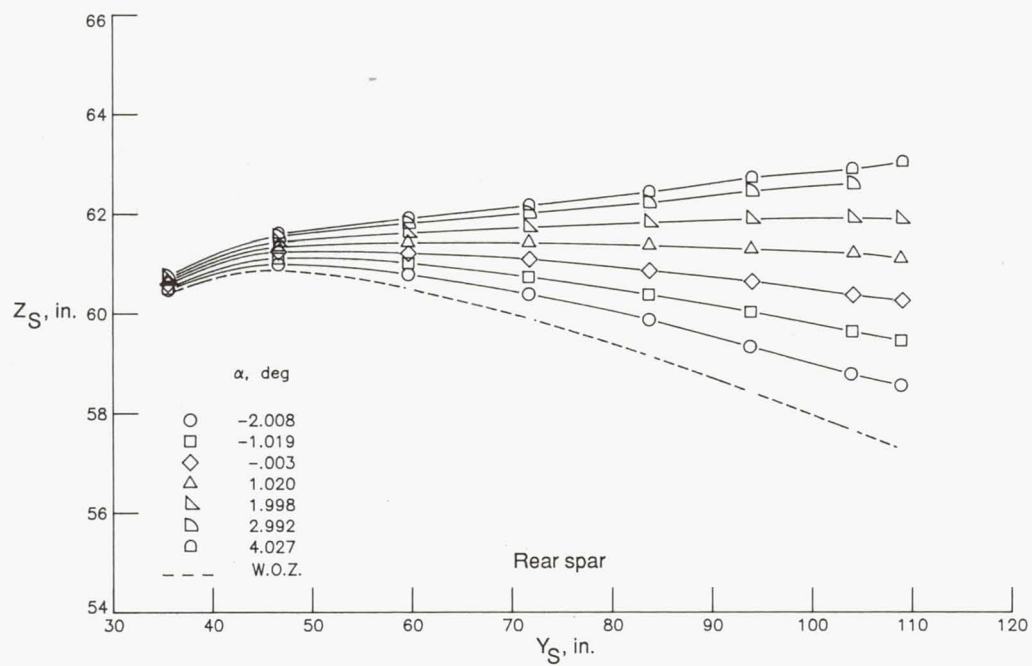
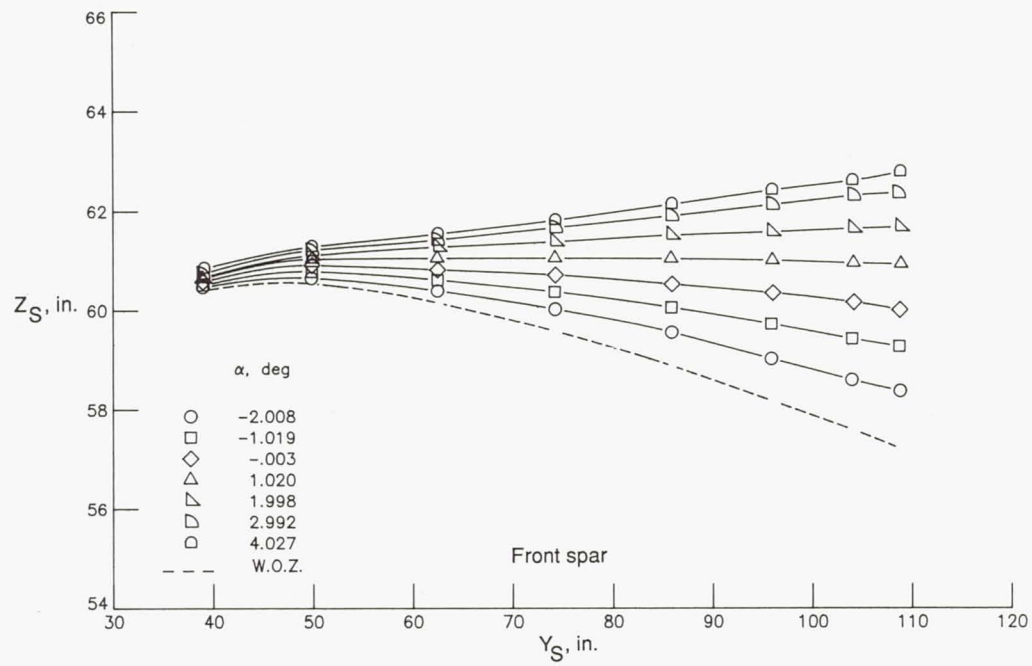
(b)  $M = 0.700$ .

Figure 8. Continued.



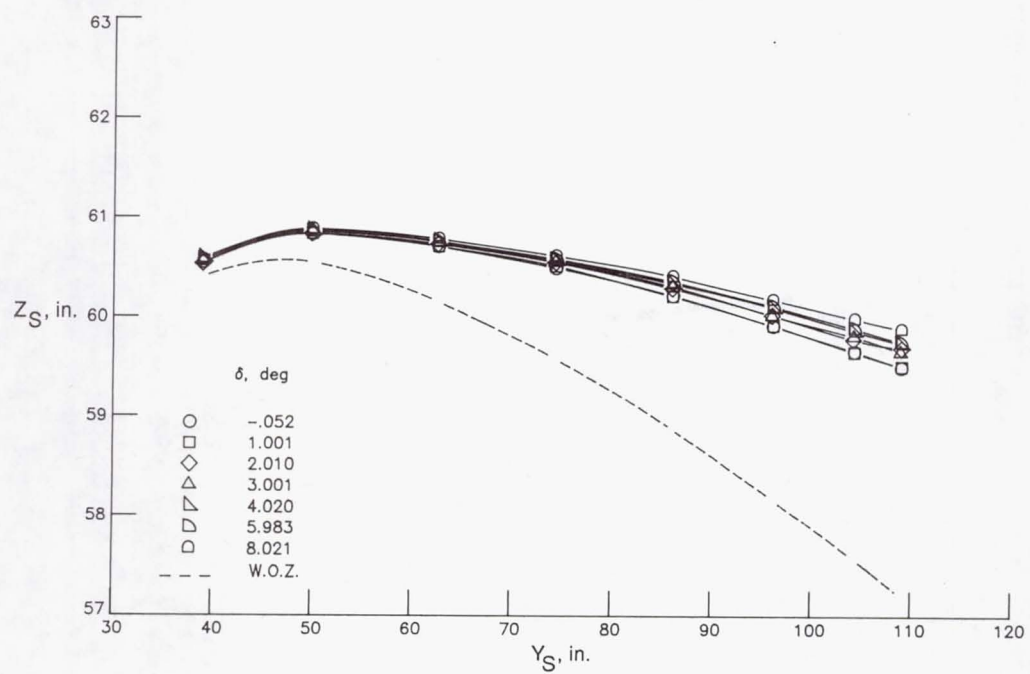
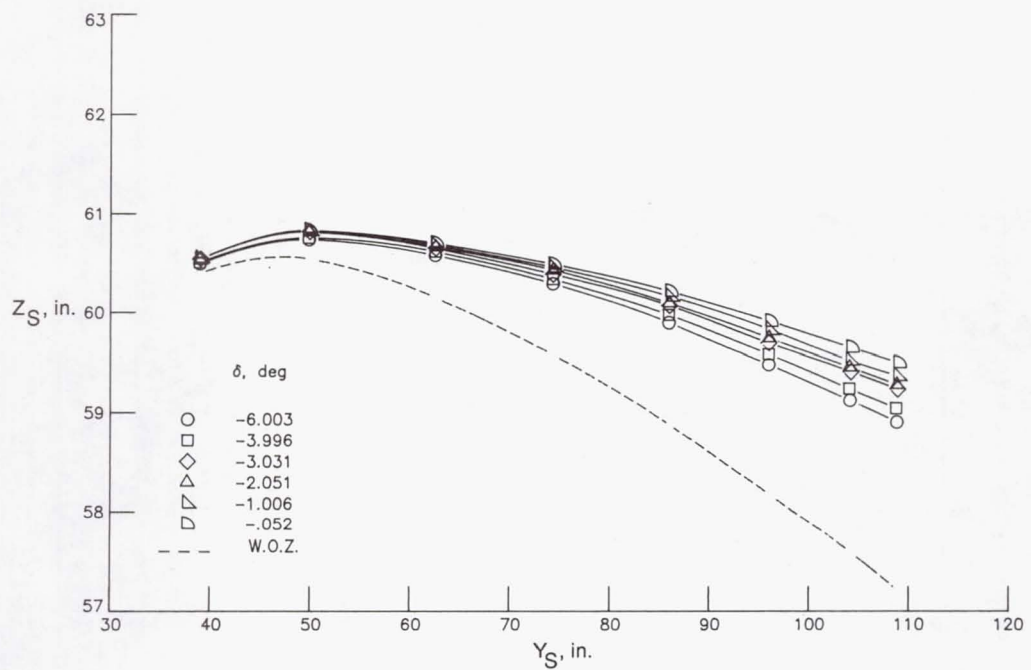
(c)  $M = 0.800$ .

Figure 8. Continued.



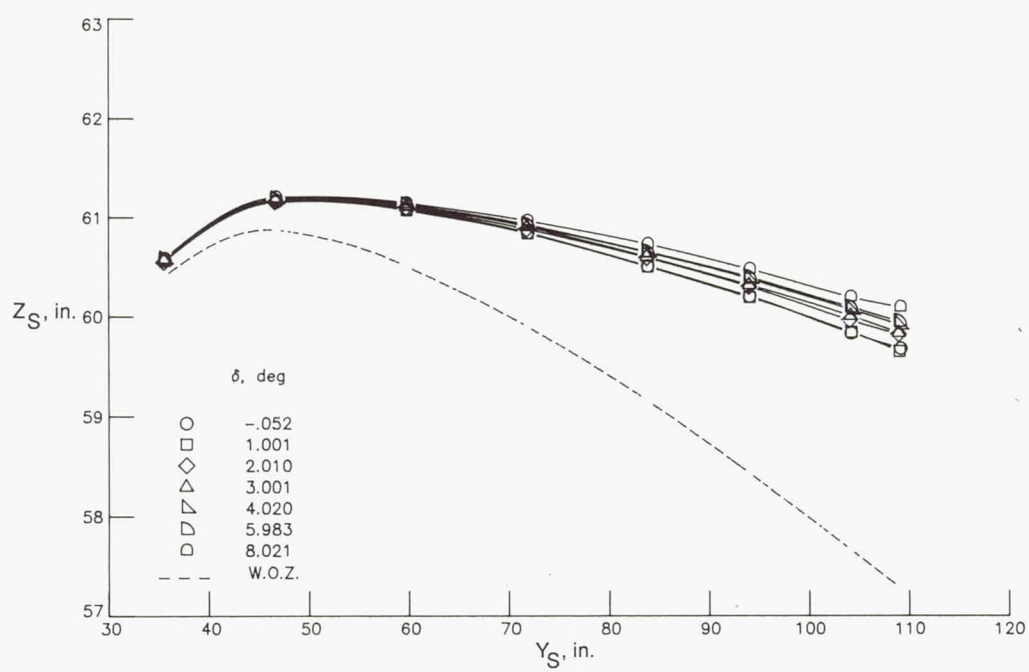
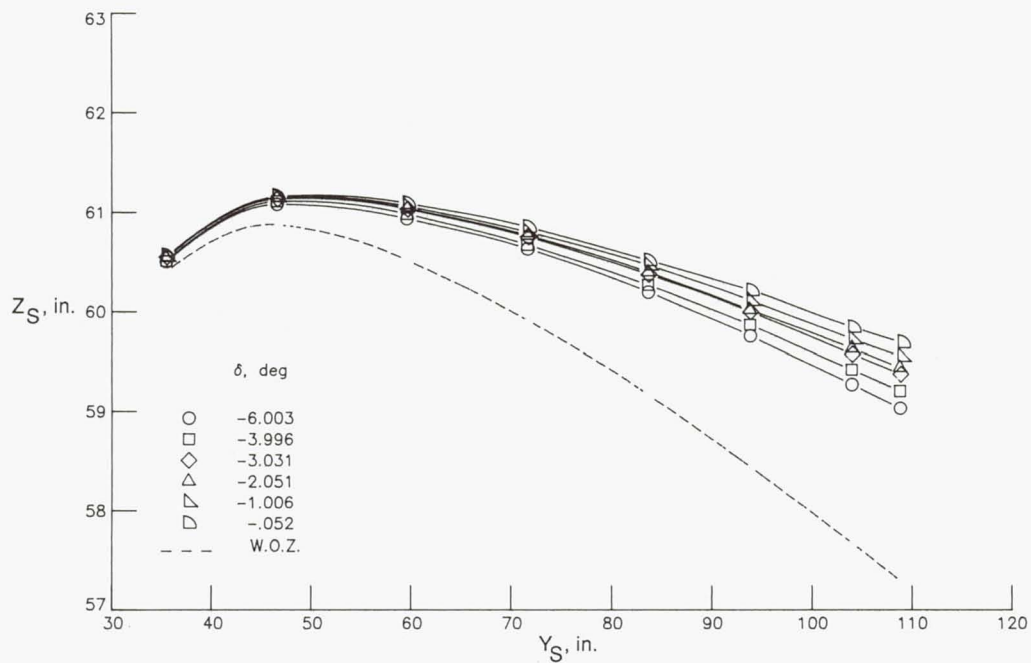
(d)  $M = 0.850$ .

Figure 8. Concluded.



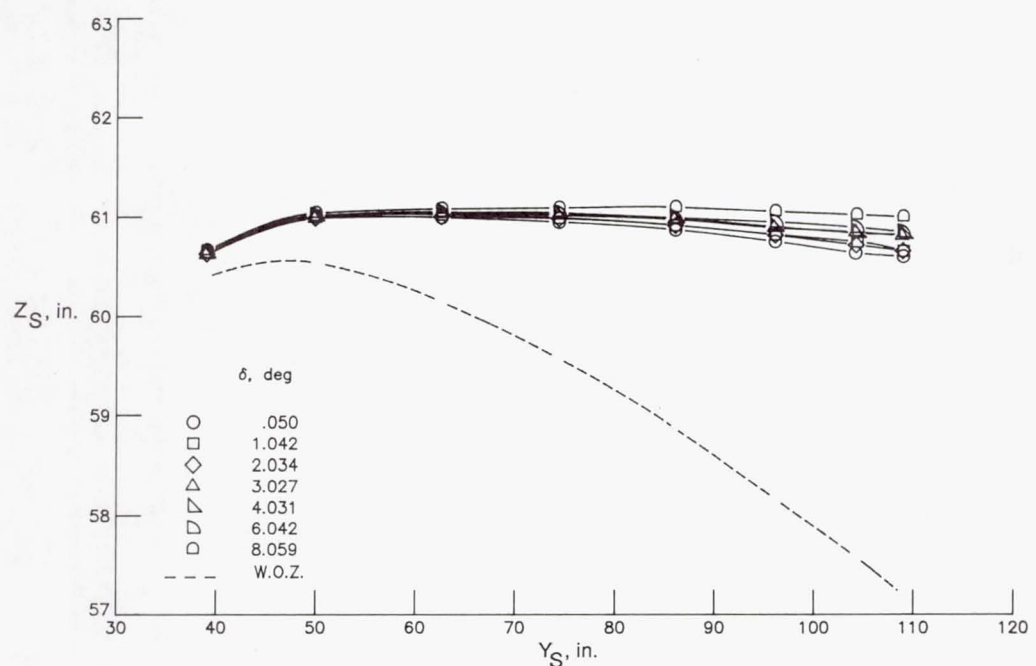
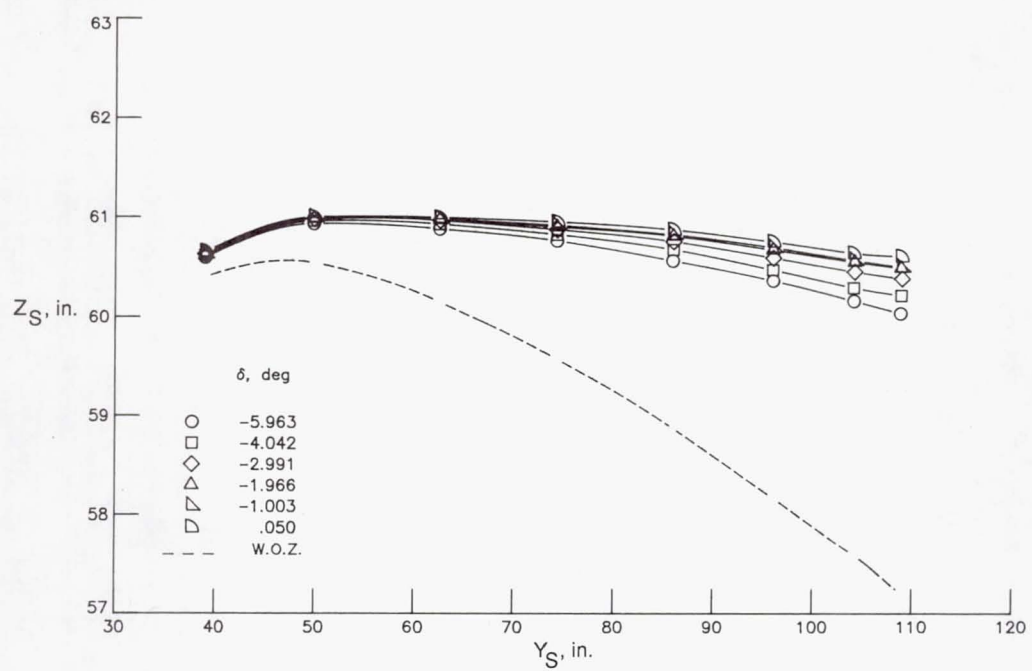
(a) Front spar;  $\alpha = 0^\circ$ .

Figure 9. Variation of wing front and rear spar shapes with control surface deflection at two angles of attack,  $q = 100$  psf, and  $M = 0.600$ .



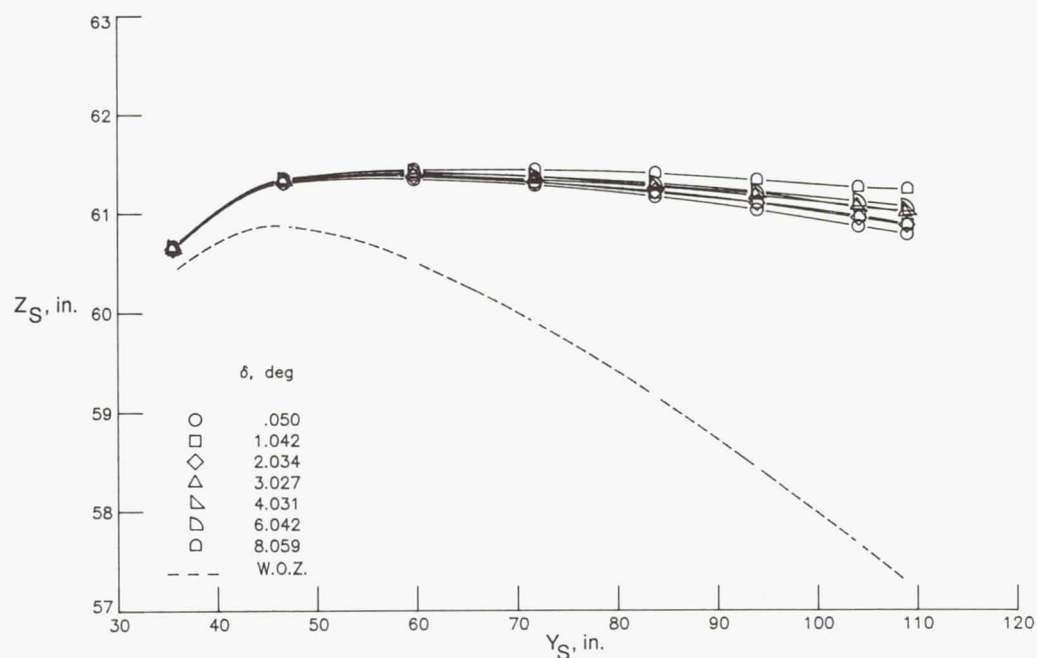
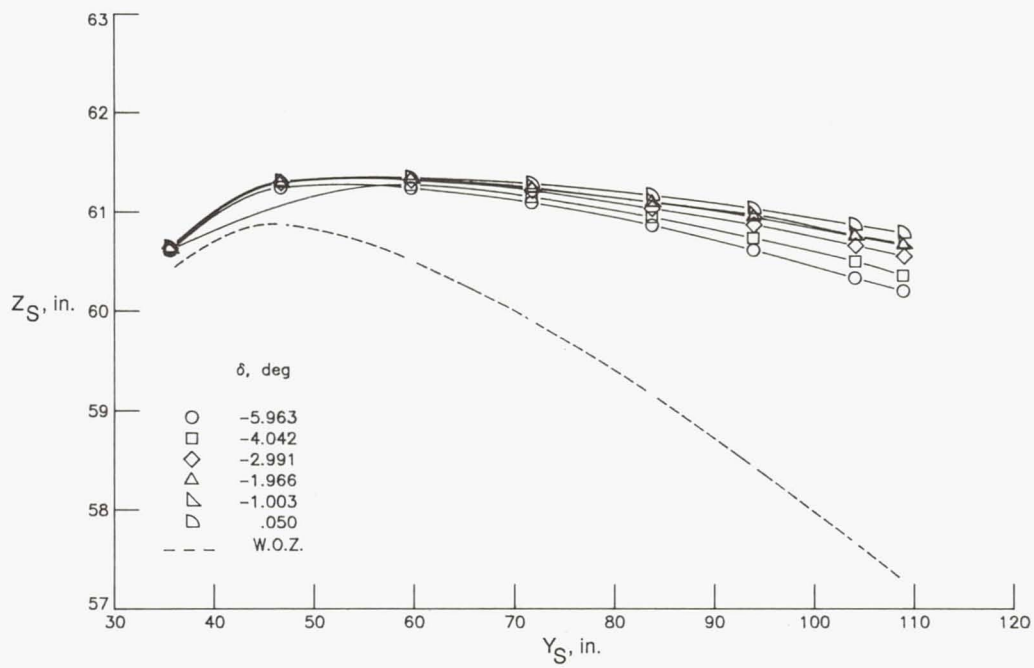
(b) Rear spar;  $\alpha = 0^\circ$ .

Figure 9. Continued.



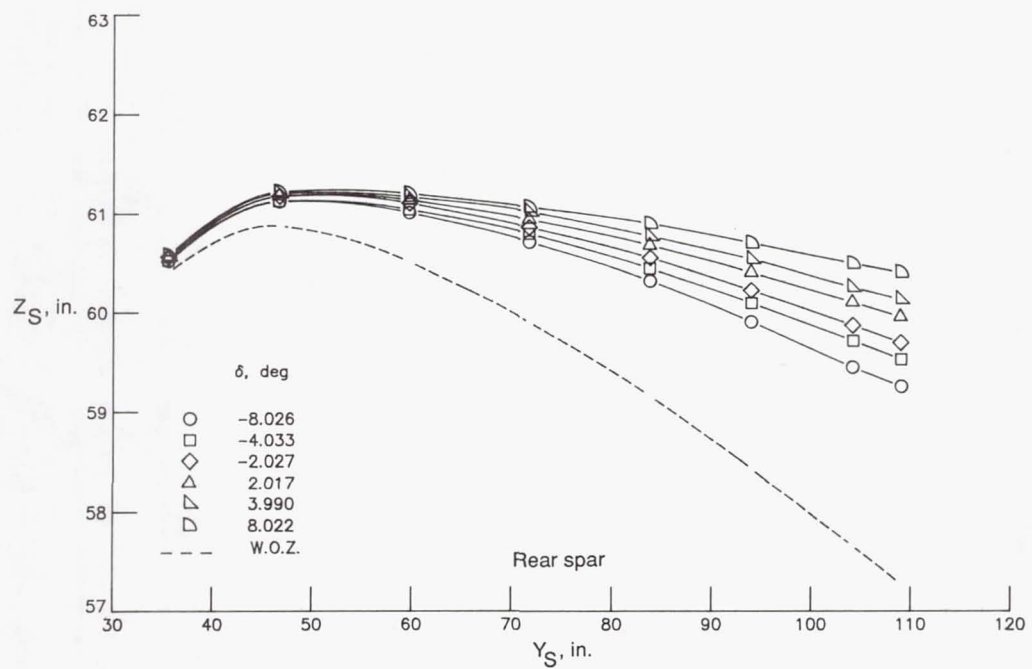
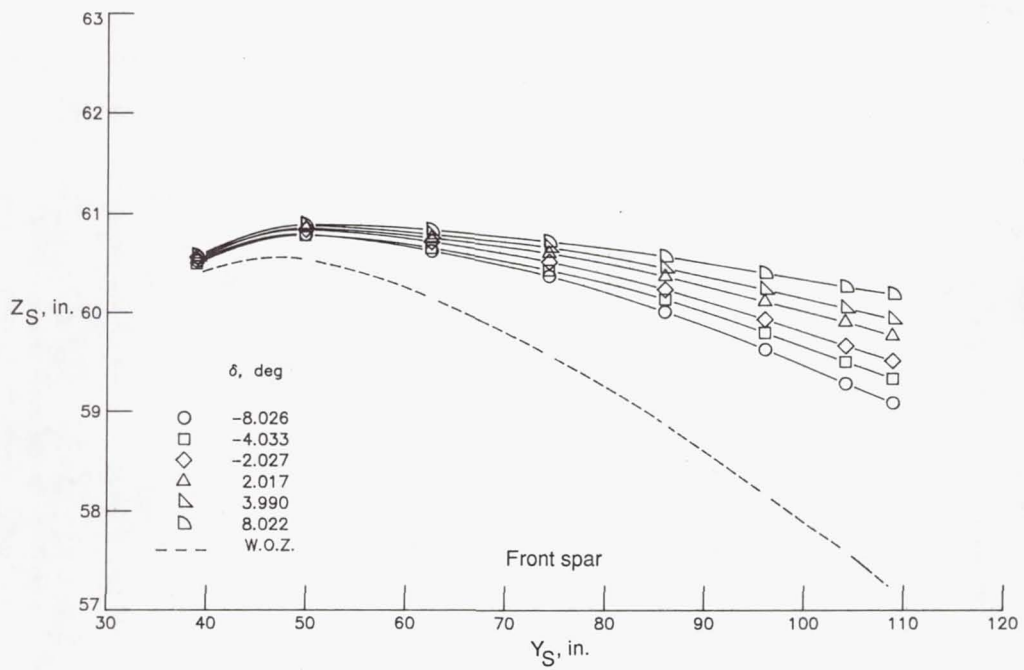
(c) Front spar;  $\alpha = 2^\circ$ .

Figure 9. Continued.



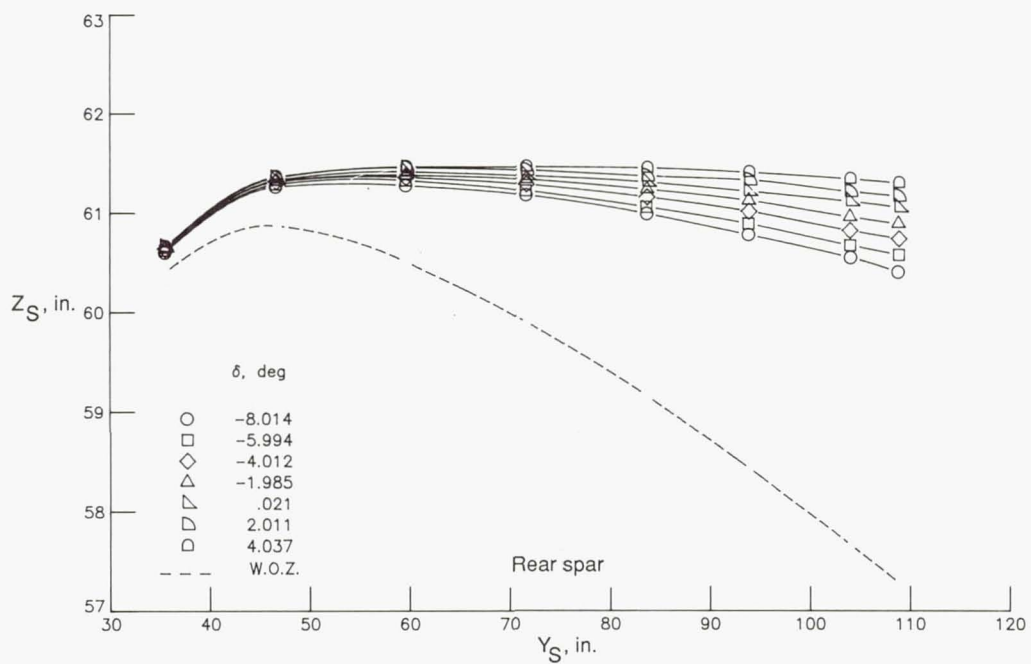
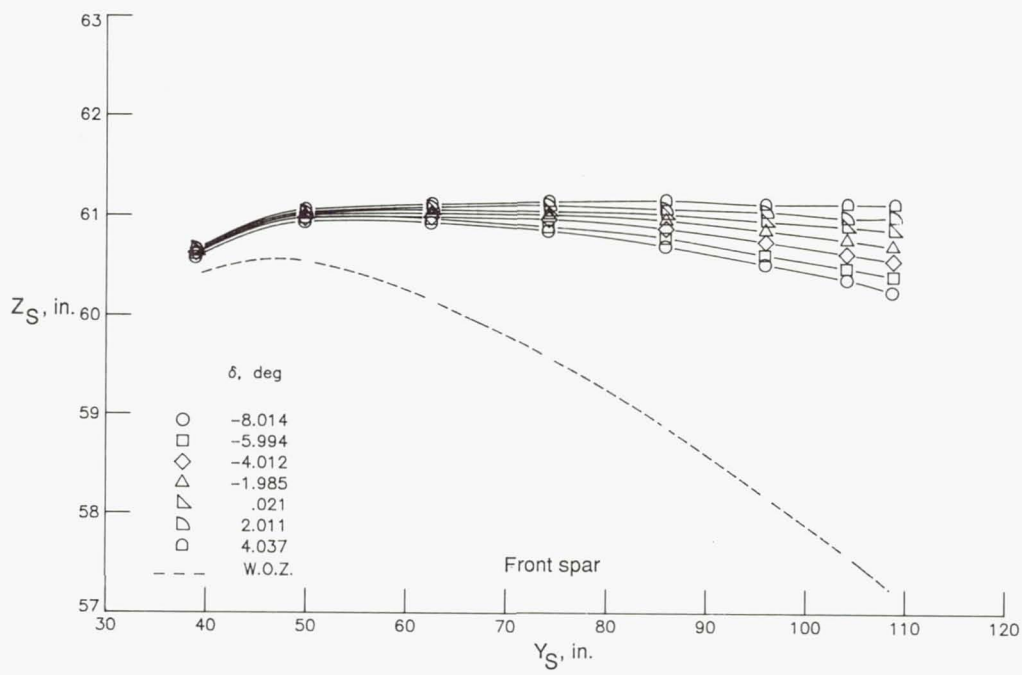
(d) Rear spar;  $\alpha = 2^\circ$ .

Figure 9. Concluded.



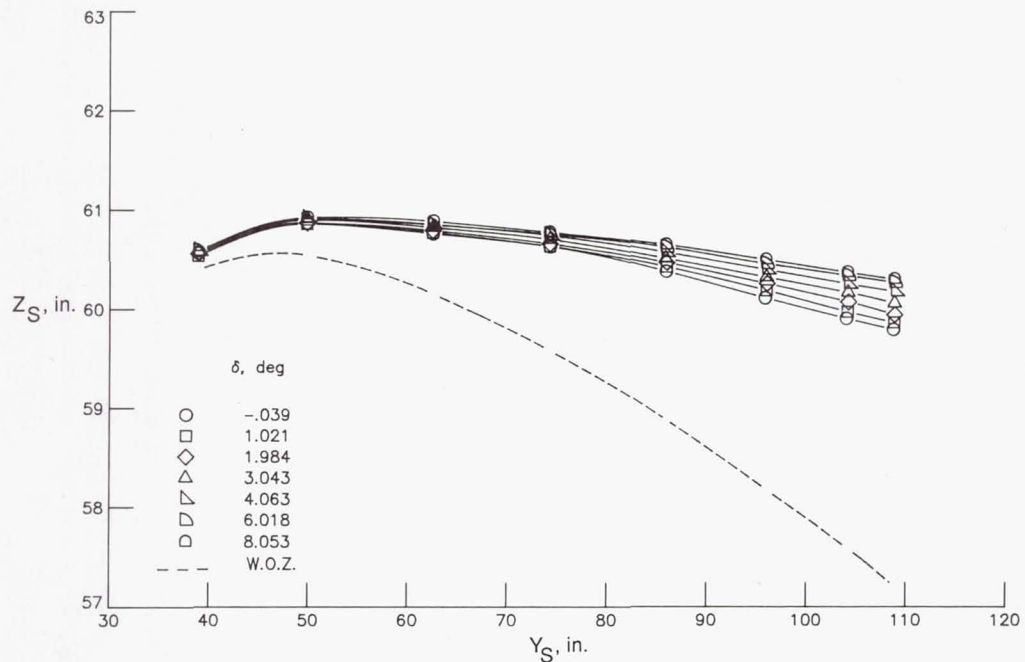
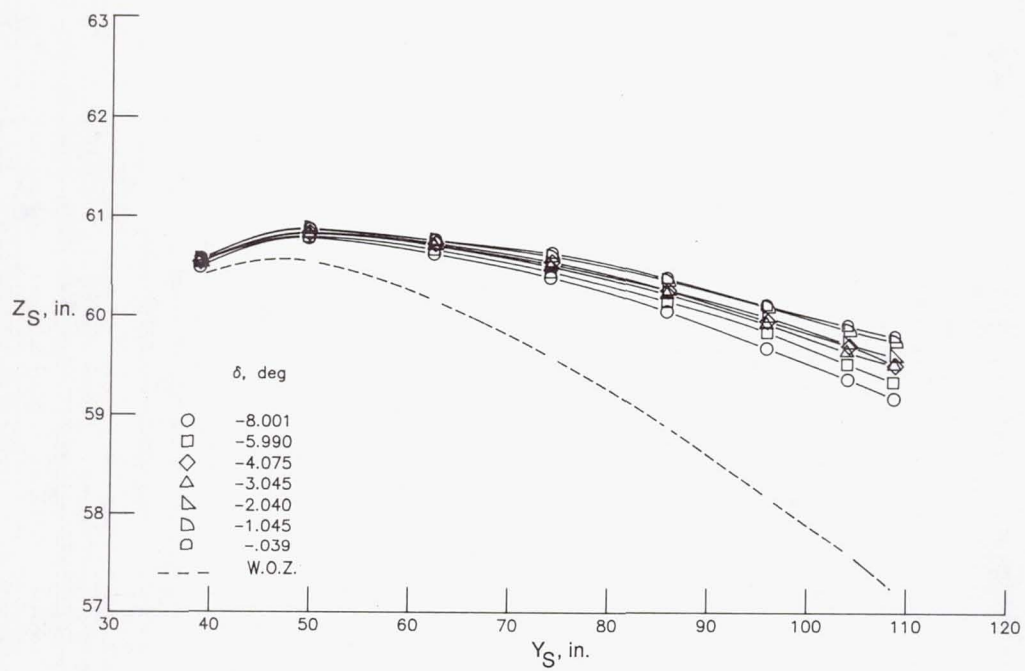
(a)  $\alpha = 0^\circ$ .

Figure 10. Variation of wing front and rear spar shapes with control surface deflection at two angles of attack,  $q = 100$  psf, and  $M = 0.700$ .



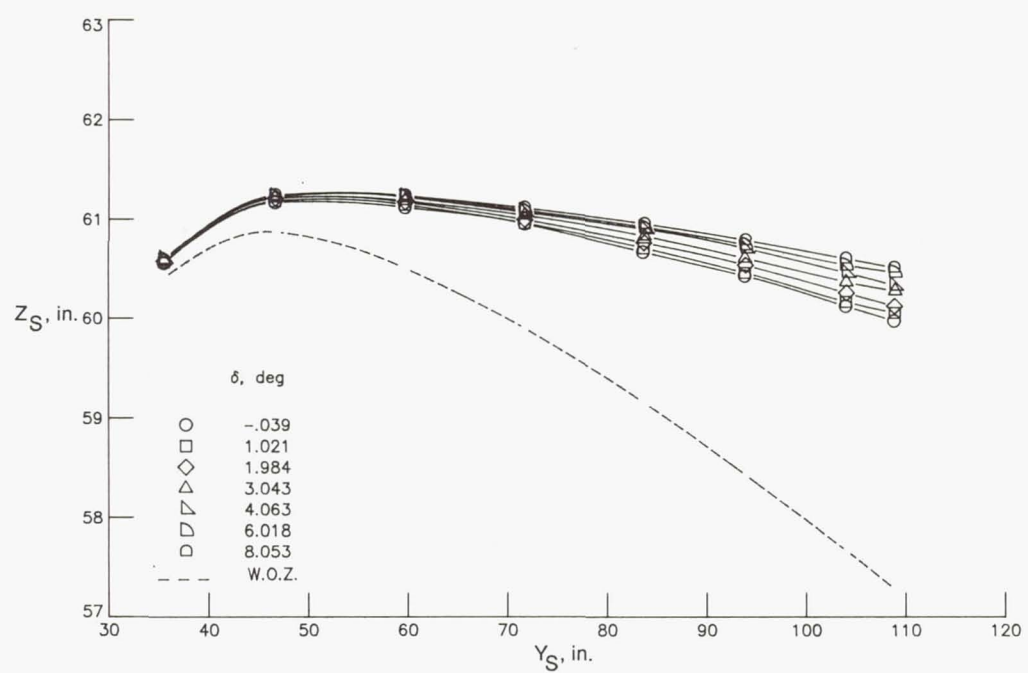
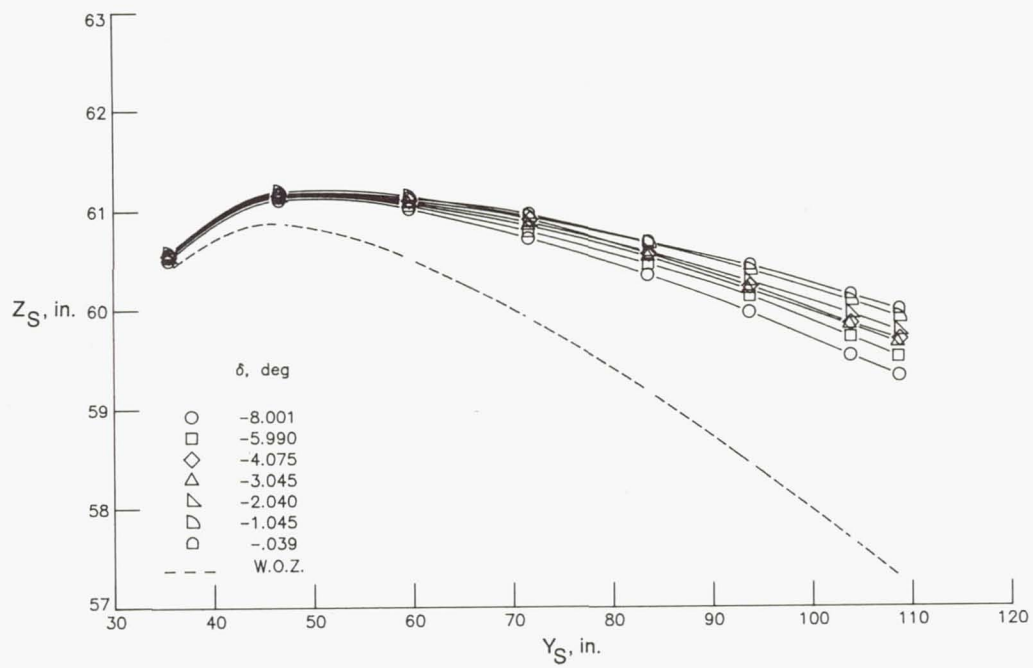
(b)  $\alpha = 2^\circ$ .

Figure 10. Concluded.



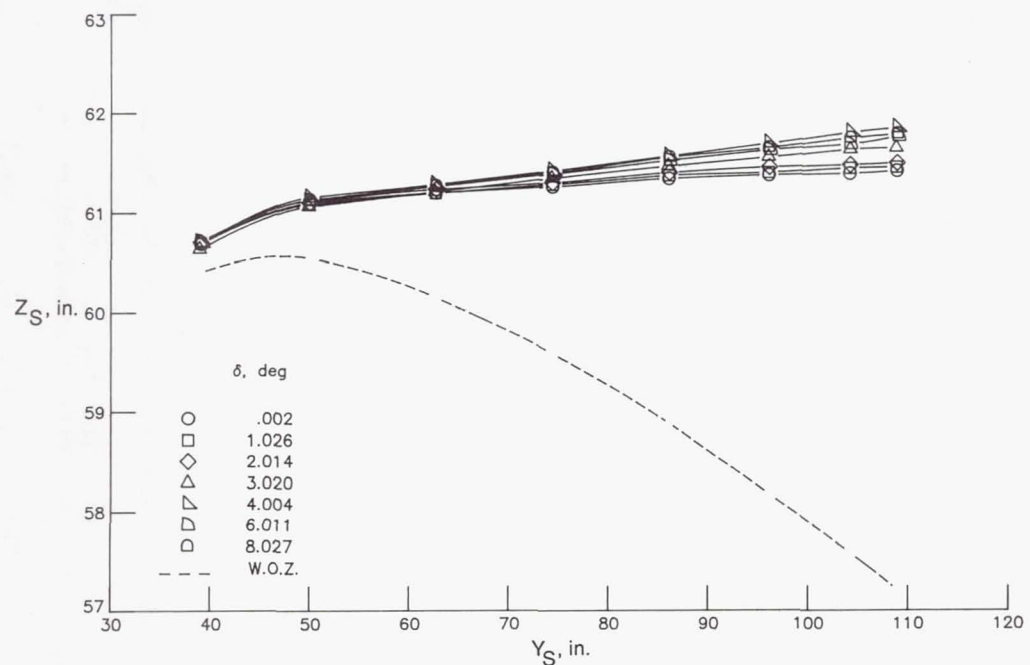
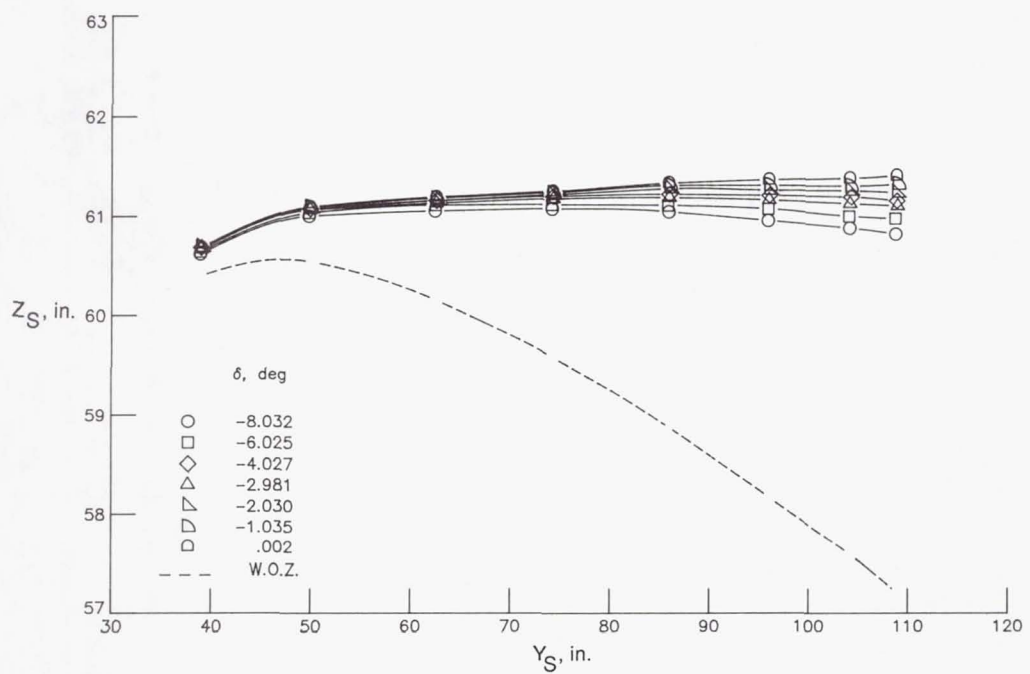
(a) Front spar;  $\alpha = 0^\circ$ .

Figure 11. Variation of wing front and rear spar shapes with control surface deflection at two angles of attack,  $q = 100$  psf, and  $M = 0.800$ .



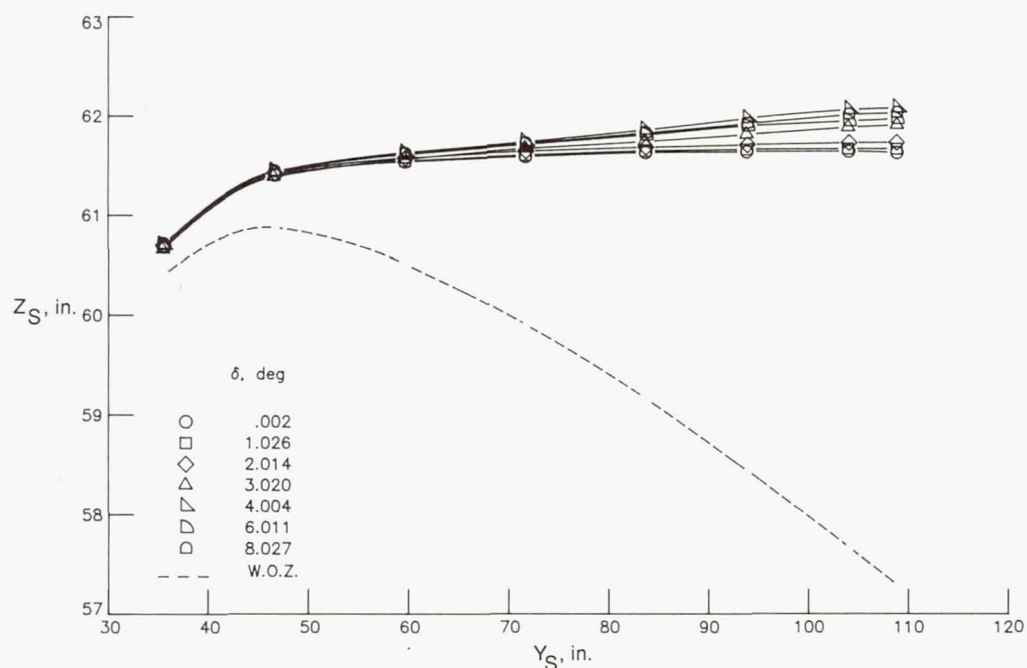
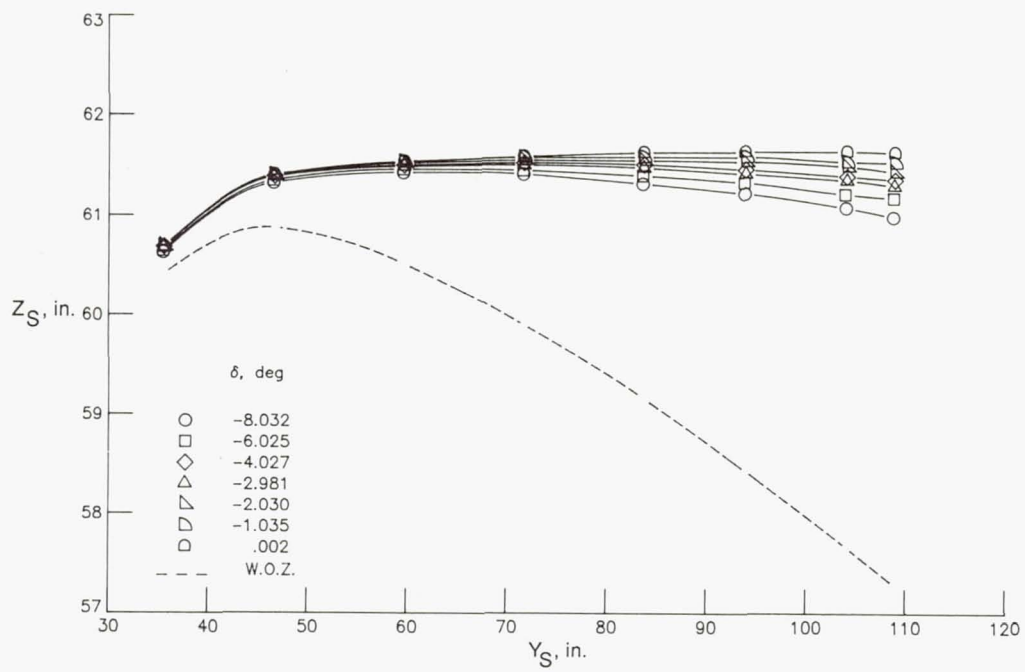
(b) Rear spar;  $\alpha = 0^\circ$ .

Figure 11. Continued.



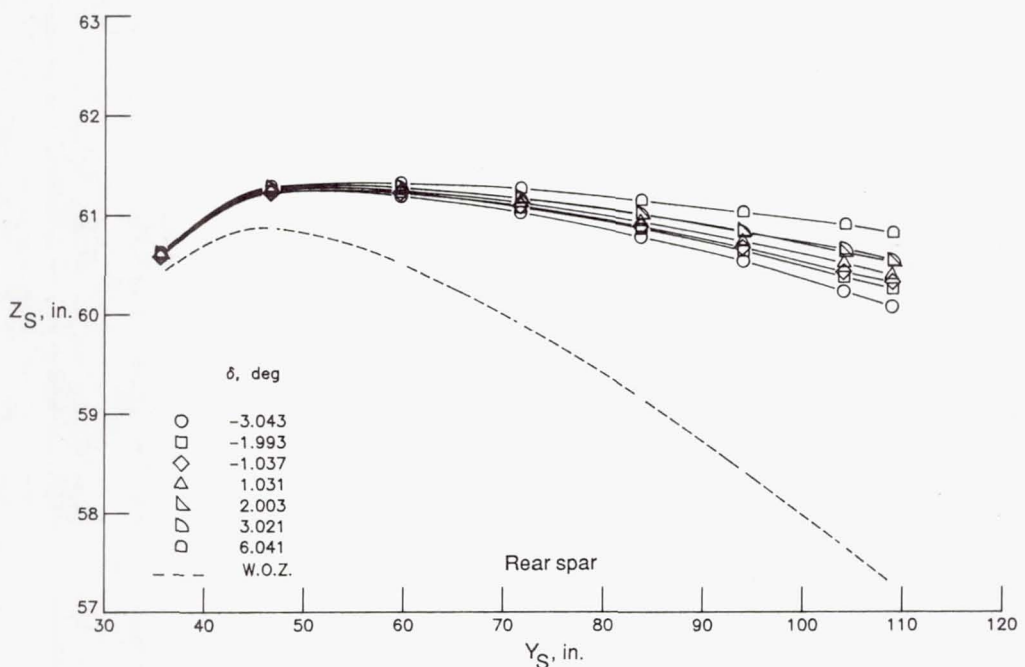
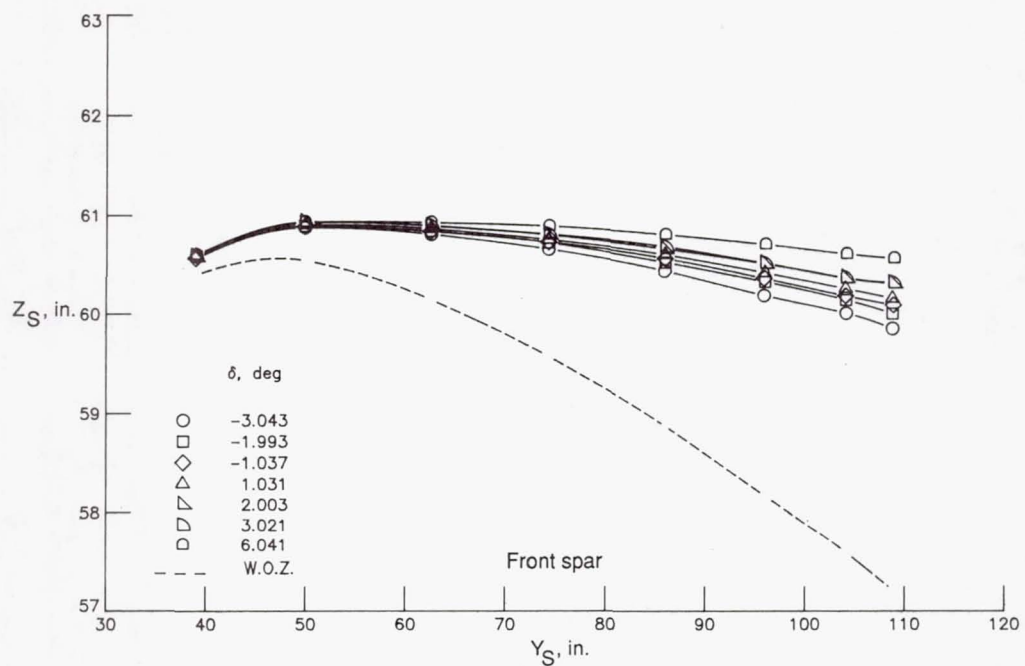
(c) Front spar;  $\alpha = 2^\circ$ .

Figure 11. Continued.



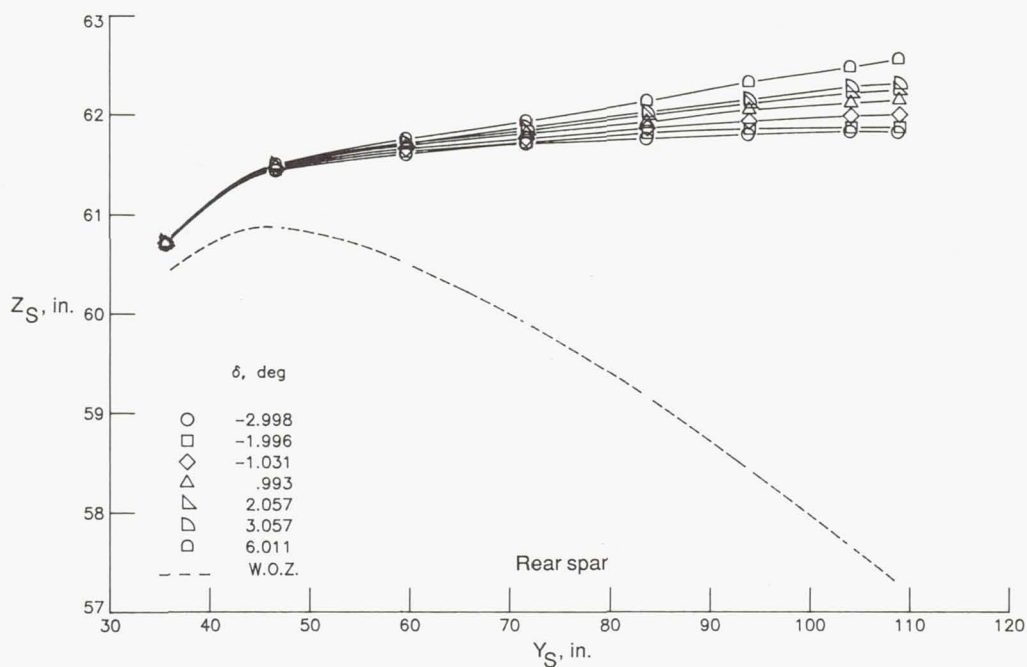
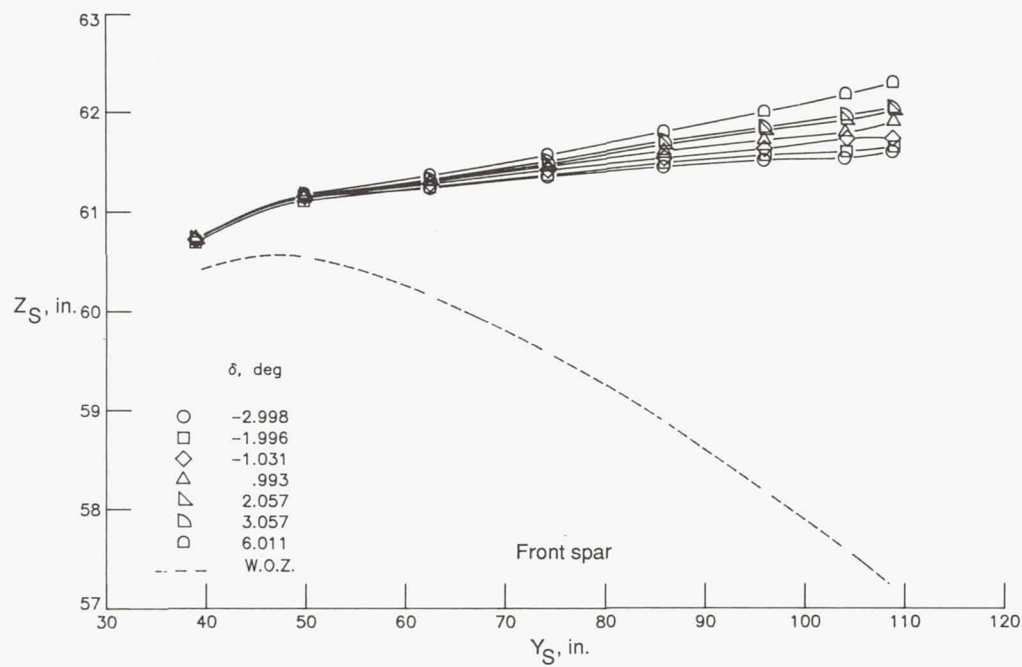
(d) Rear spar;  $\alpha = 2^\circ$ .

Figure 11. Concluded.



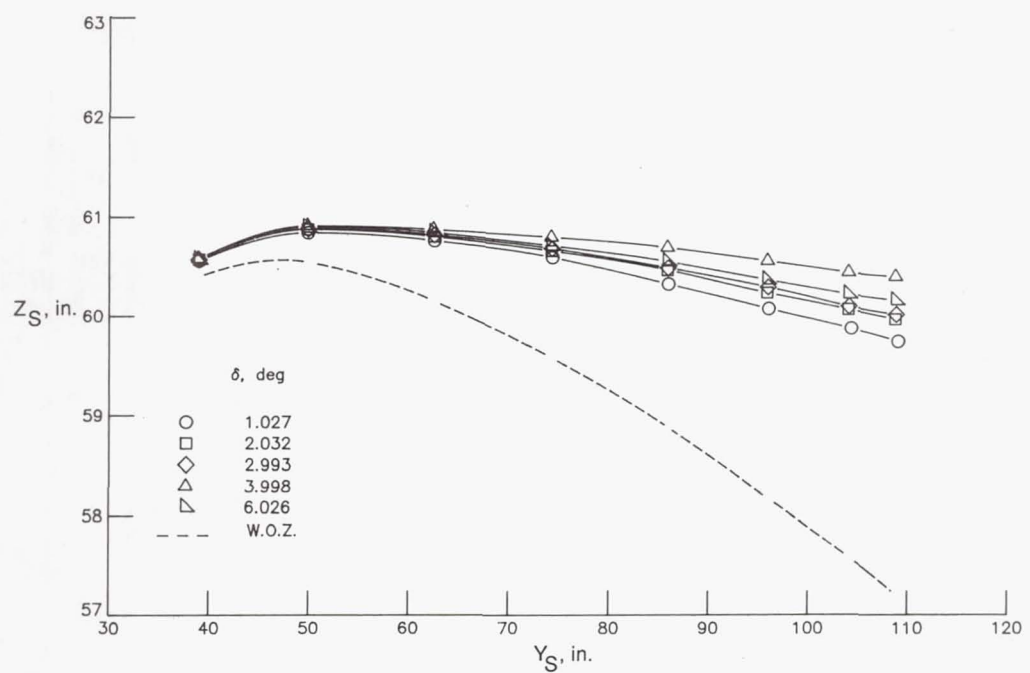
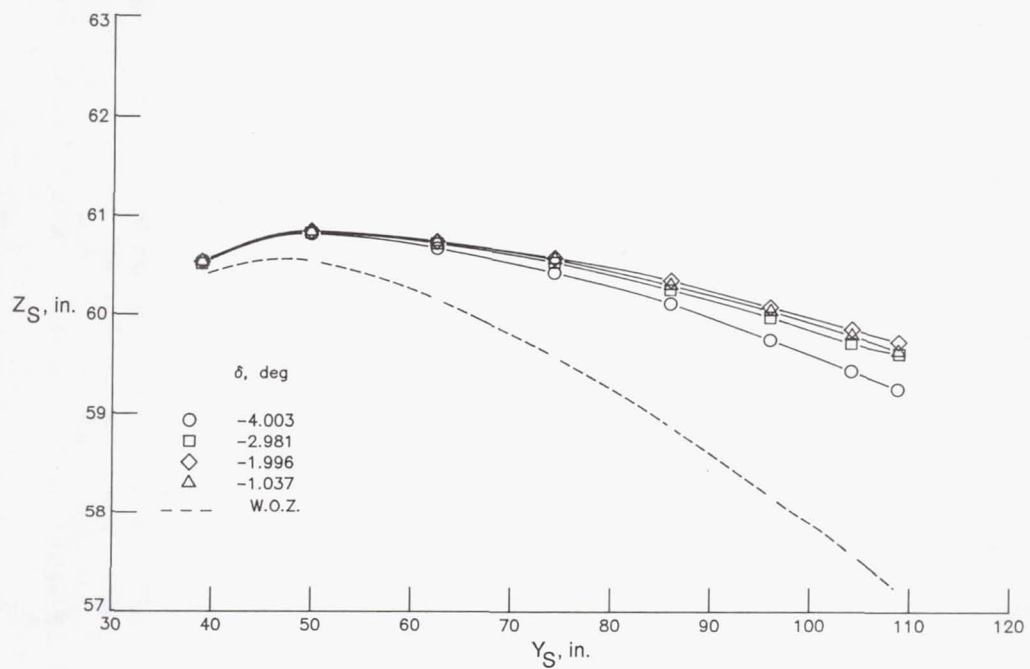
(a)  $\alpha = 0^\circ$ .

Figure 12. Variation of wing front and rear spar shapes with control surface deflection at two angles of attack,  $q = 100$  psf, and  $M = 0.850$ .



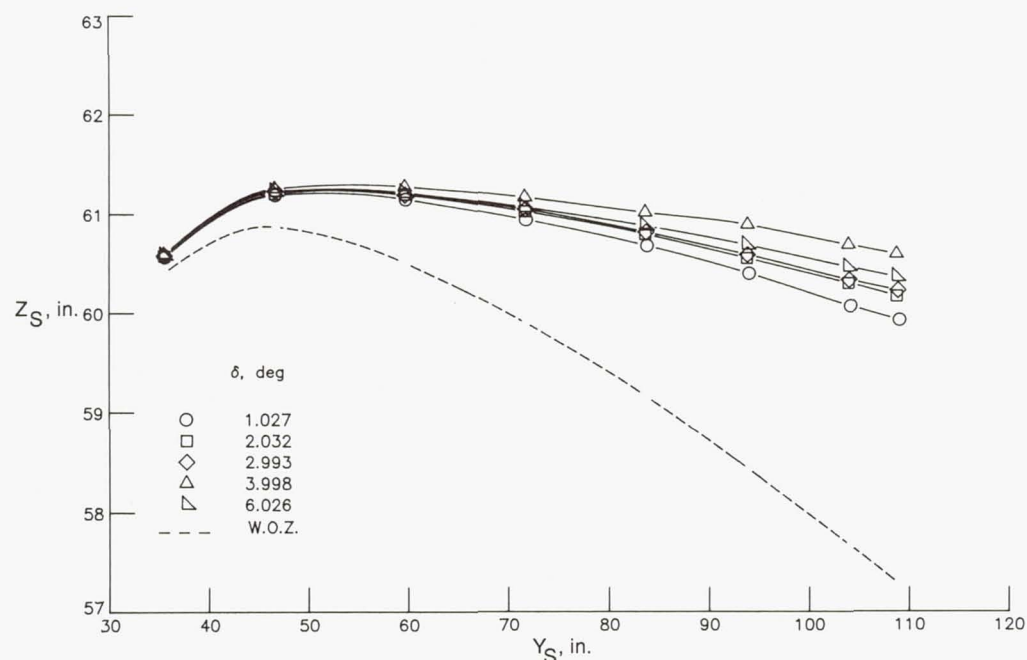
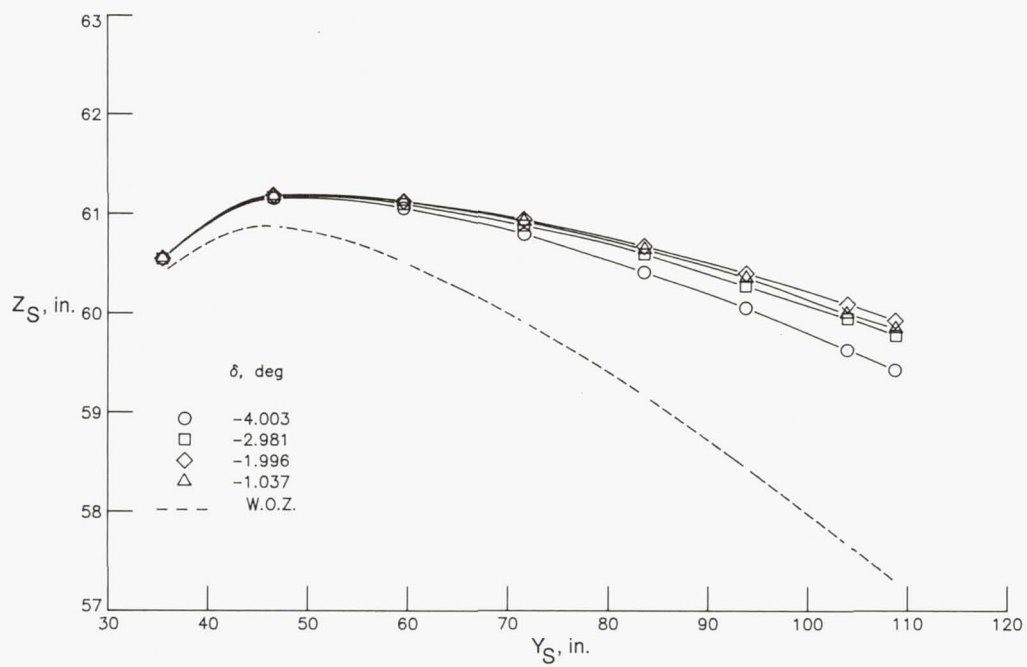
(b)  $\alpha = 2^\circ$ .

Figure 12. Concluded.



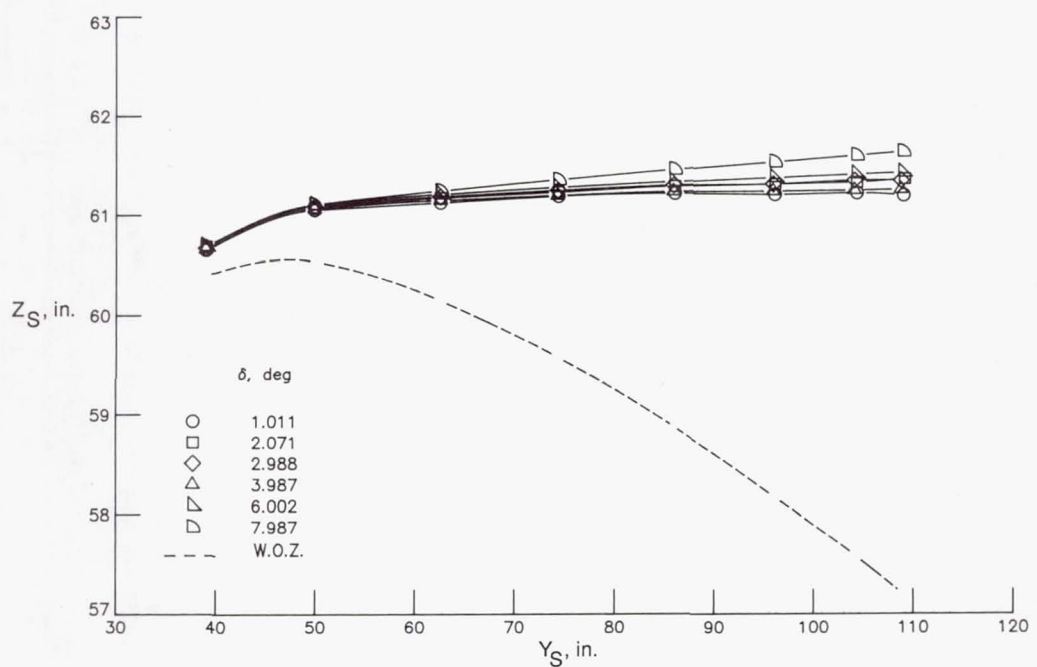
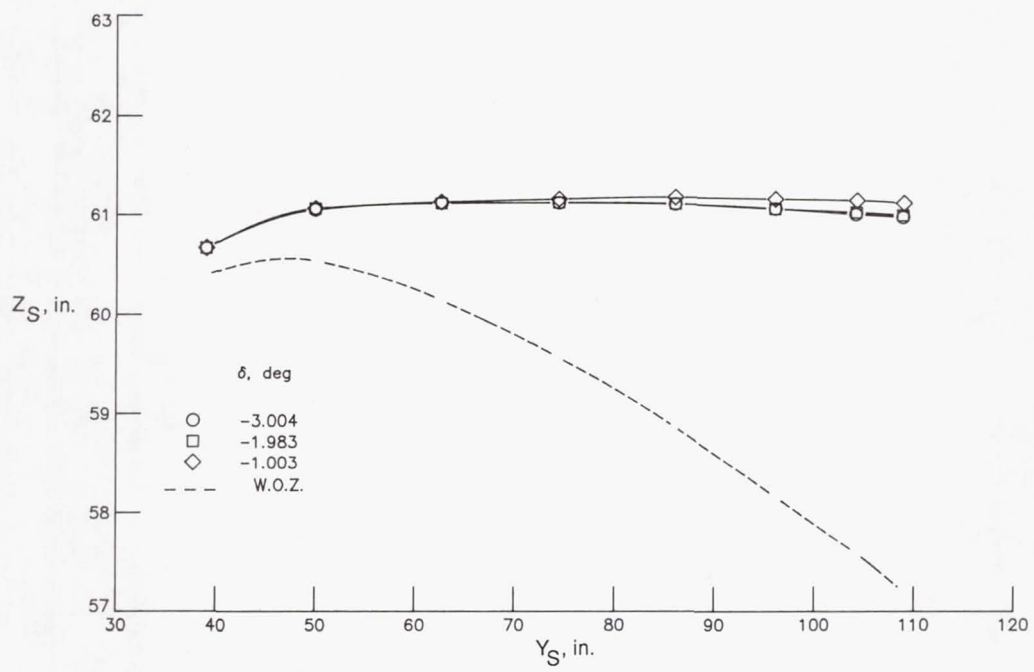
(a) Front spar;  $\alpha = 0^\circ$ .

Figure 13. Variation of wing front and rear spar shapes with control surface deflection at two angles of attack,  $q = 100$  psf, and  $M = 0.880$ .



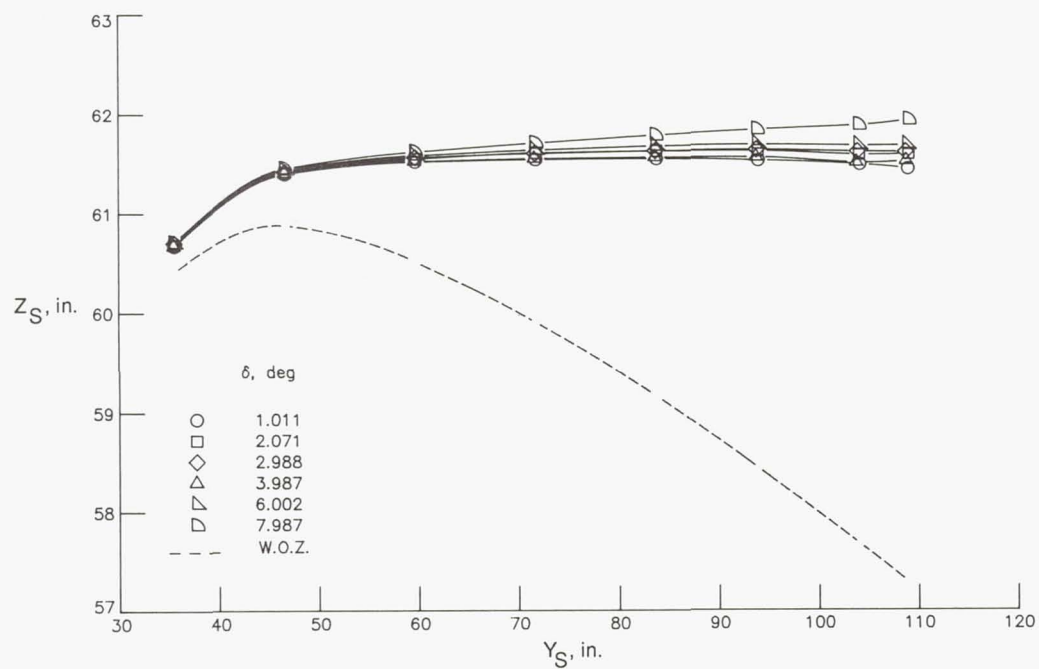
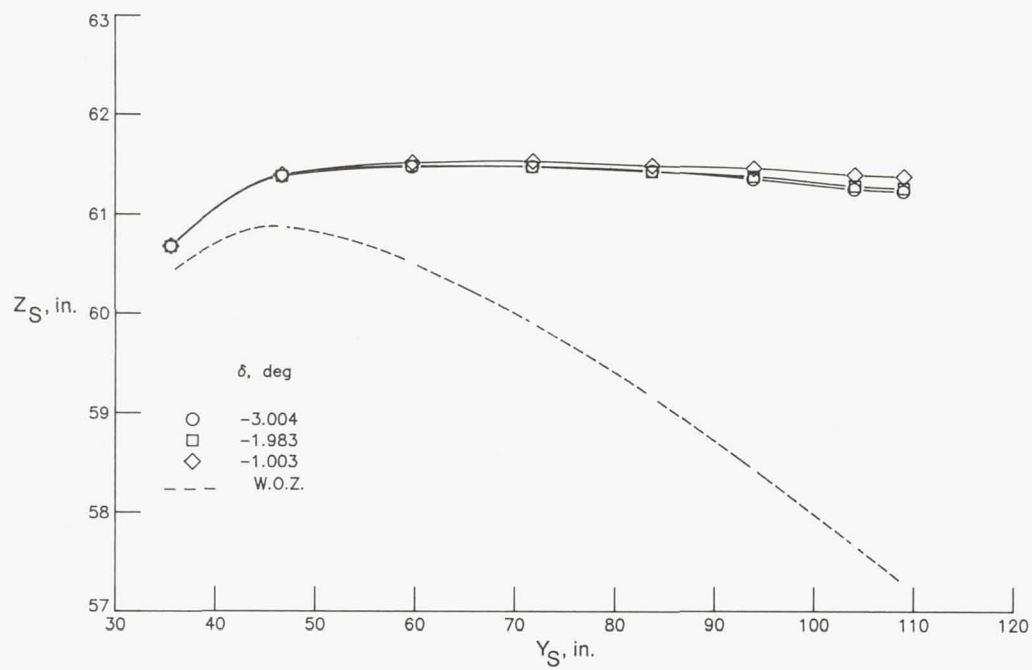
(b) Rear spar;  $\alpha = 0^\circ$ .

Figure 13. Continued.



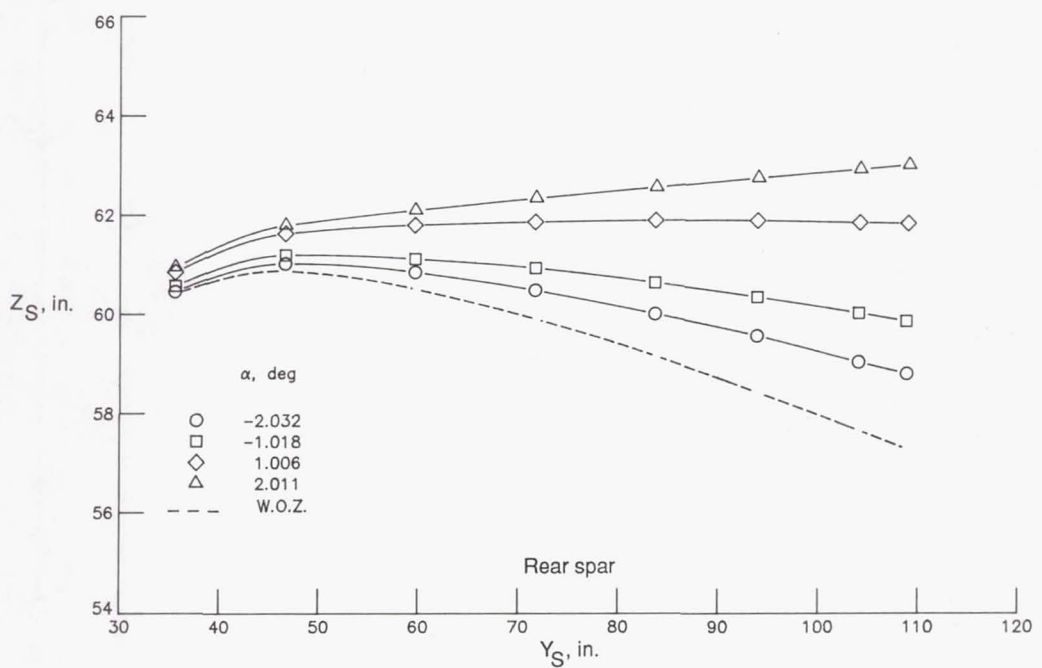
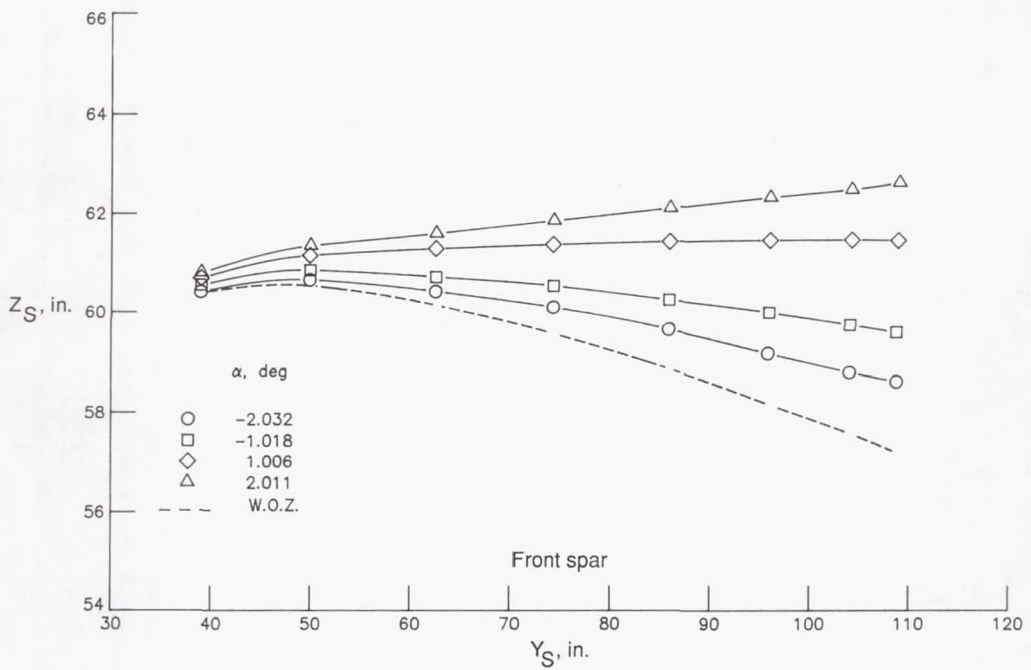
(c) Front spar;  $\alpha = 2^\circ$ .

Figure 13. Continued.



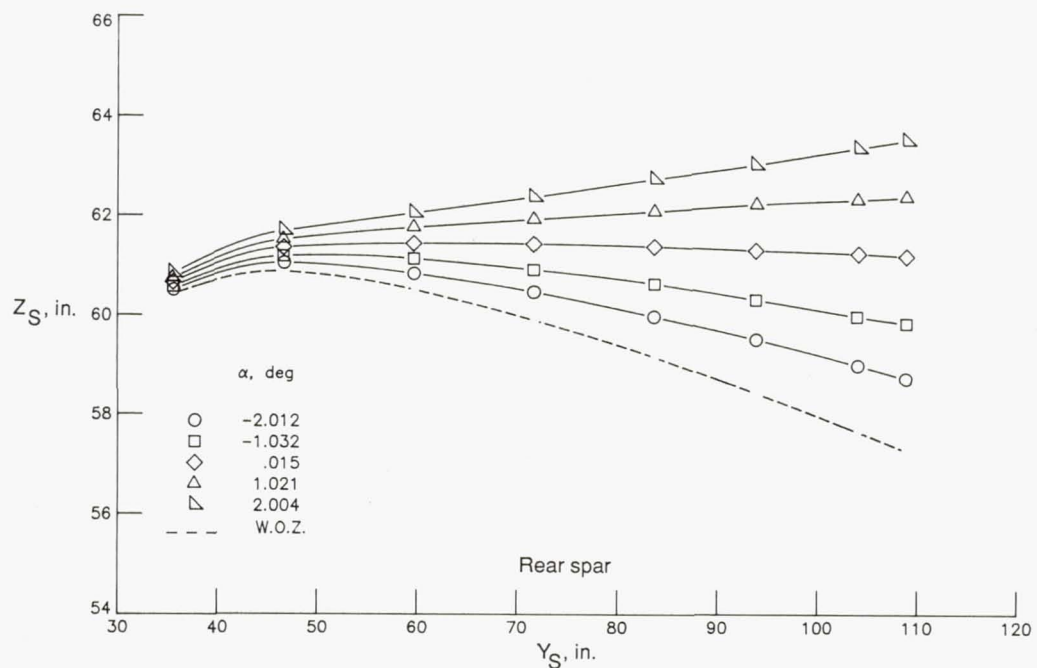
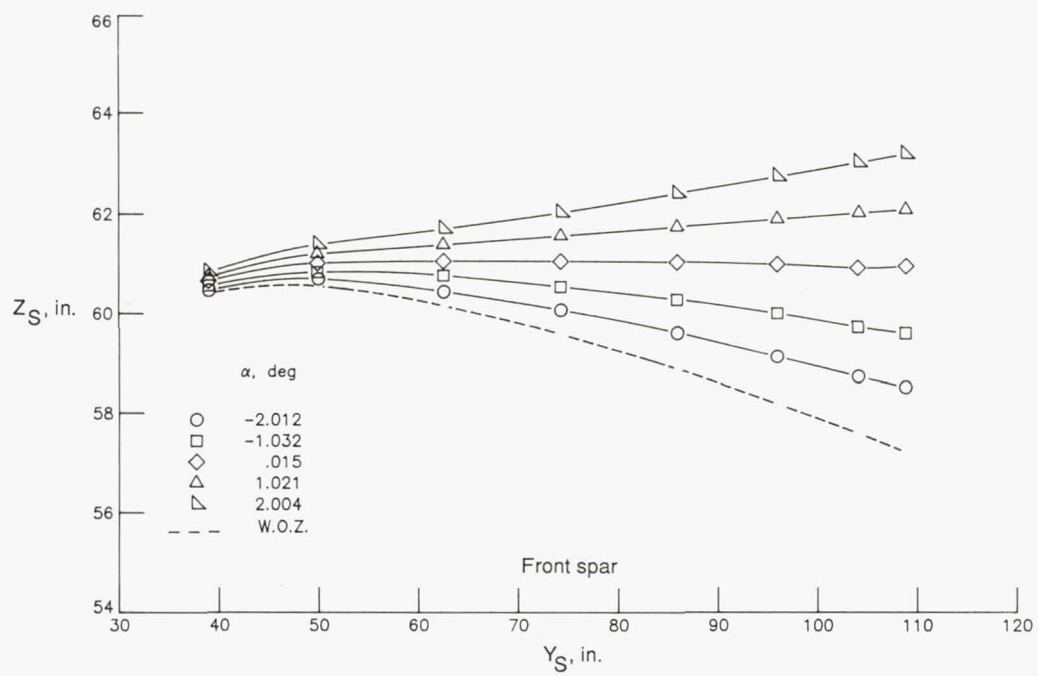
(d) Rear spar;  $\alpha = 2^\circ$ .

Figure 13. Concluded.



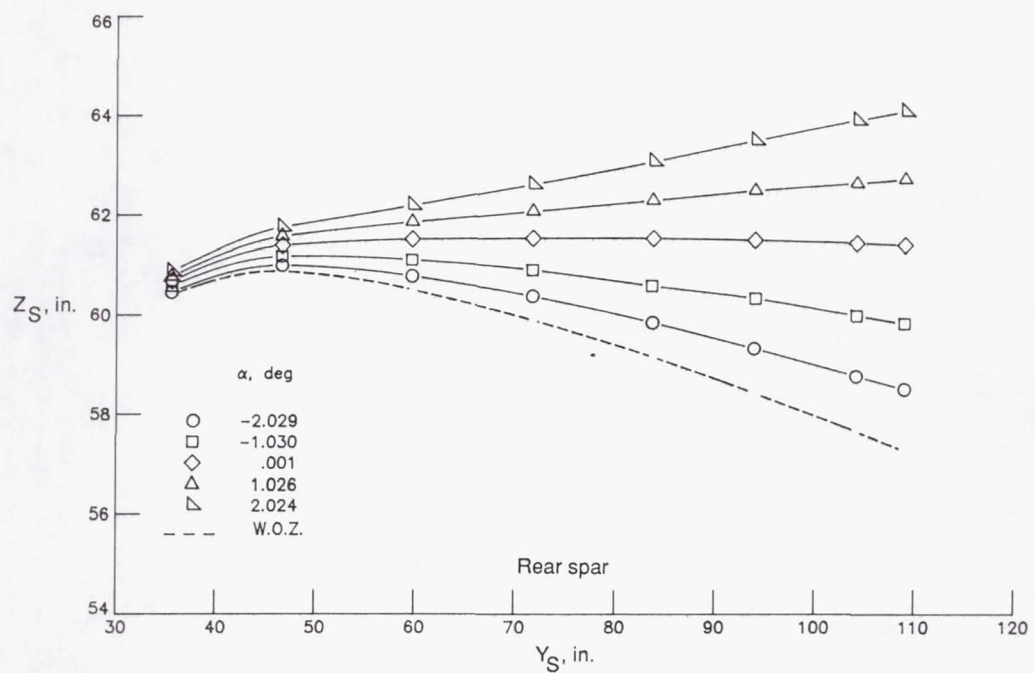
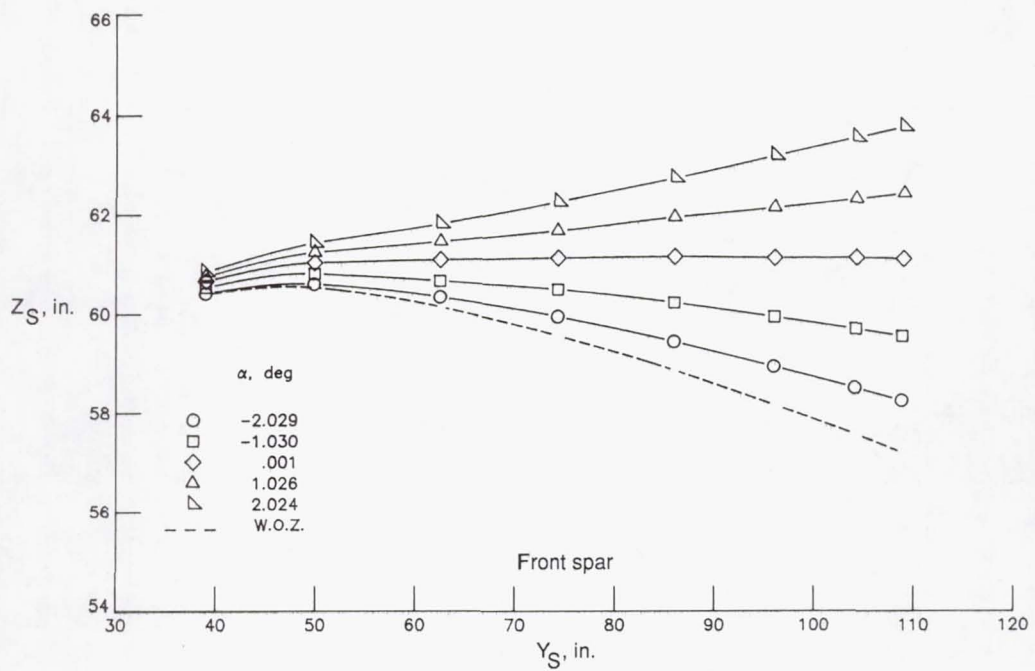
(a)  $M = 0.600$ .

Figure 14. Variation of wing front and rear spar shapes with angle of attack at four Mach numbers and  $q = 200$  psf.



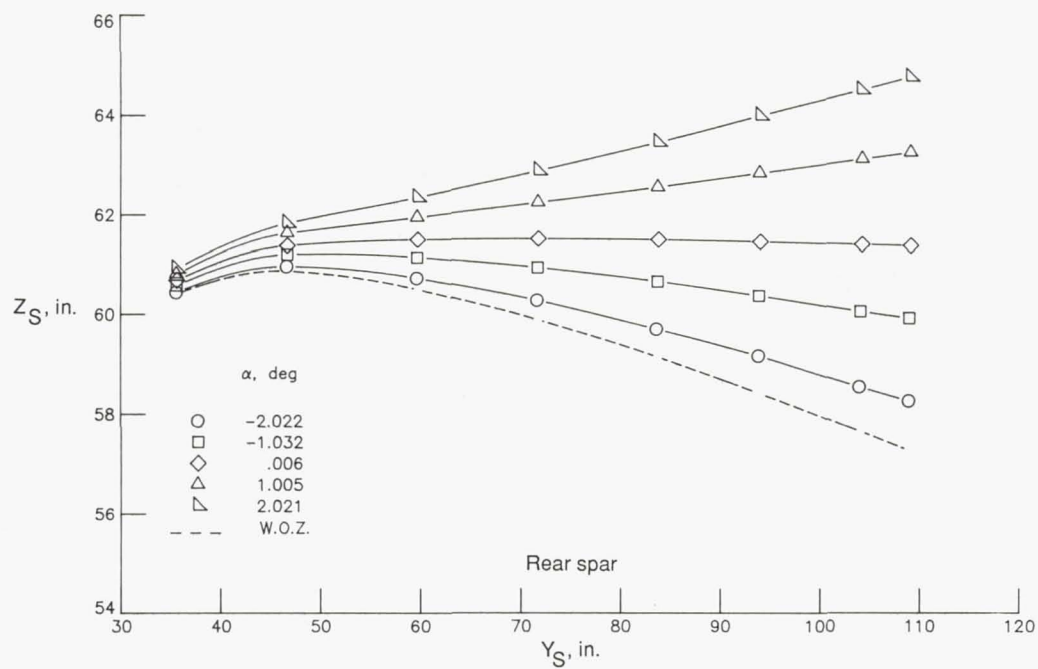
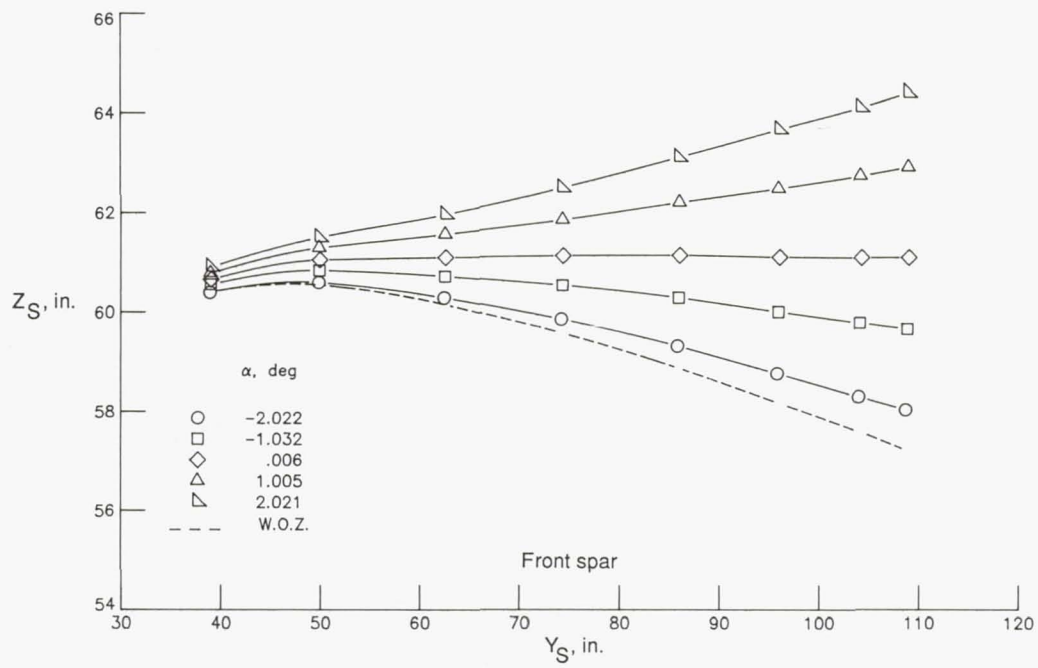
(b)  $M = 0.700$ .

Figure 14. Continued.



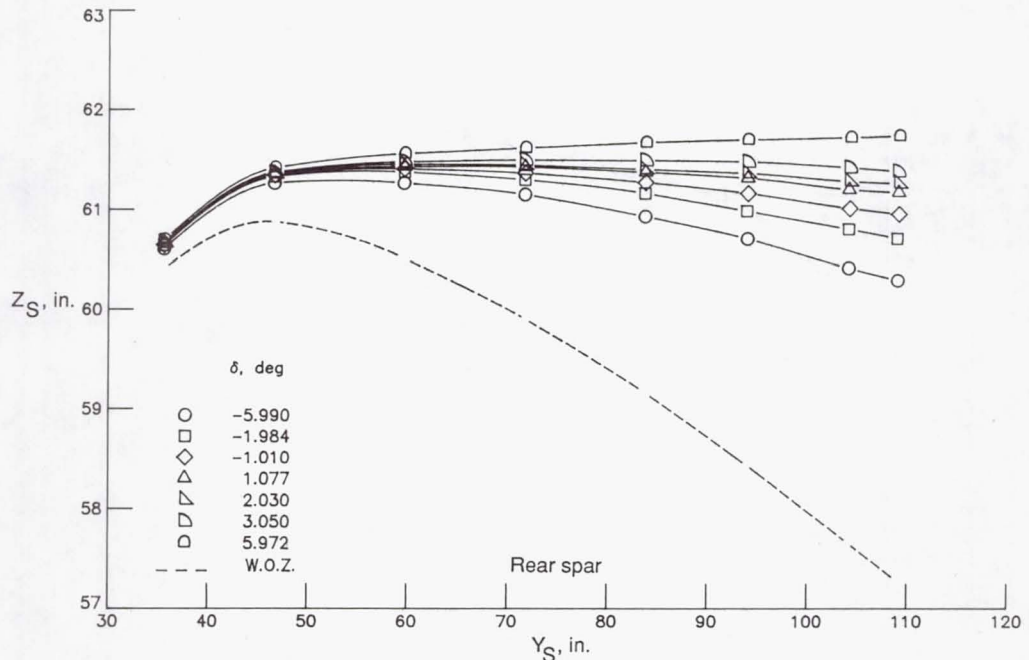
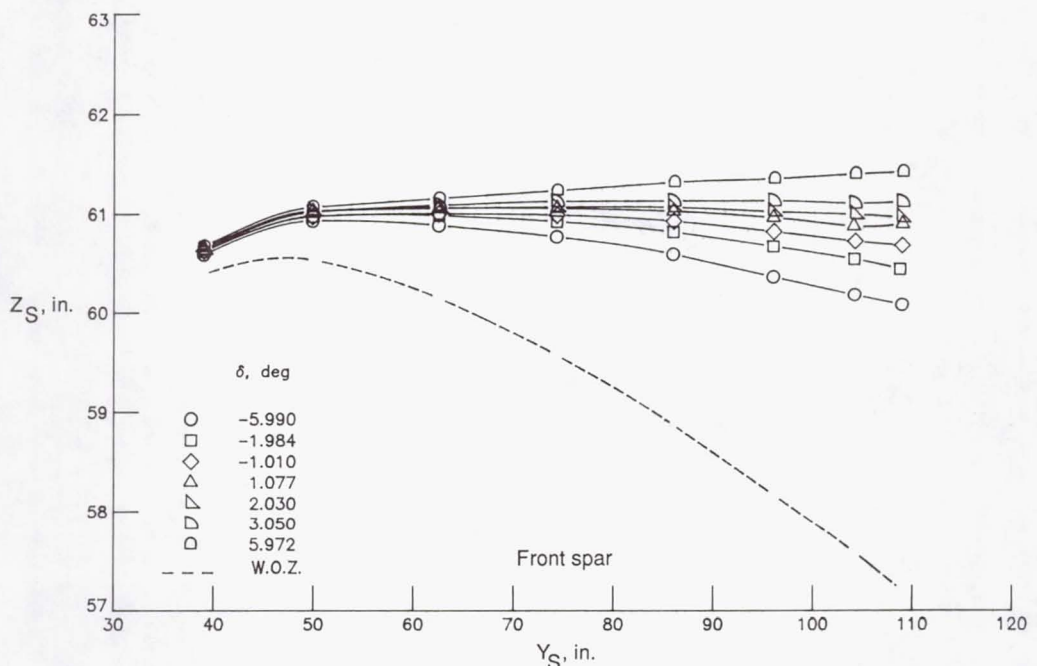
(c)  $M = 0.800$ .

Figure 14. Continued.



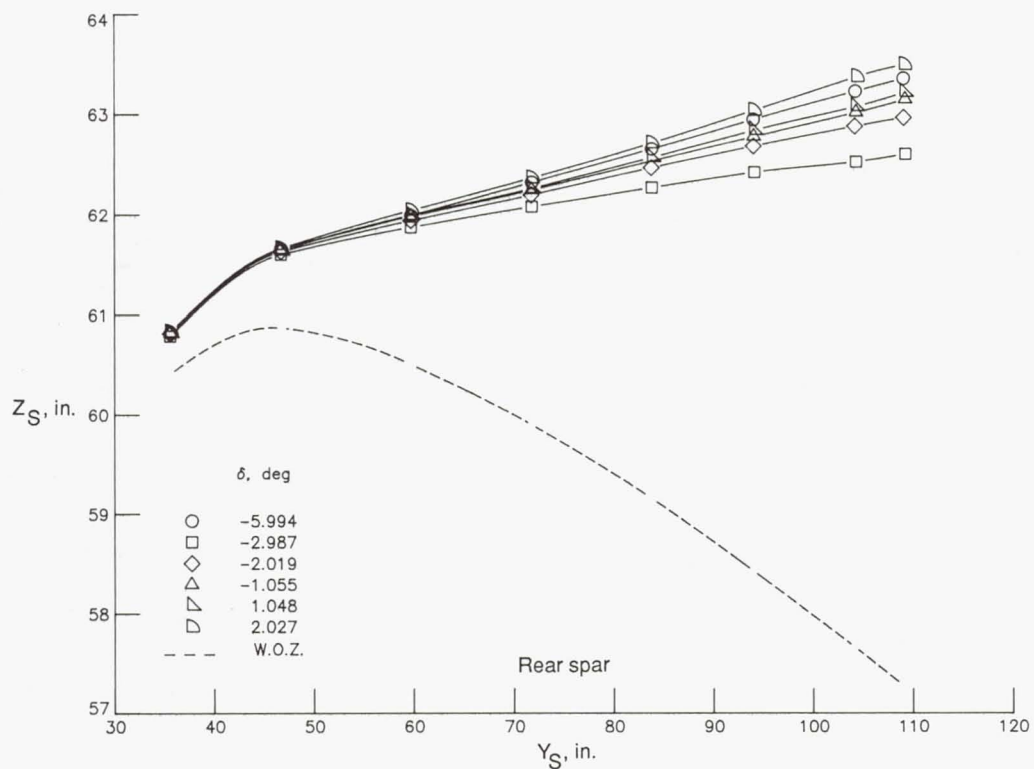
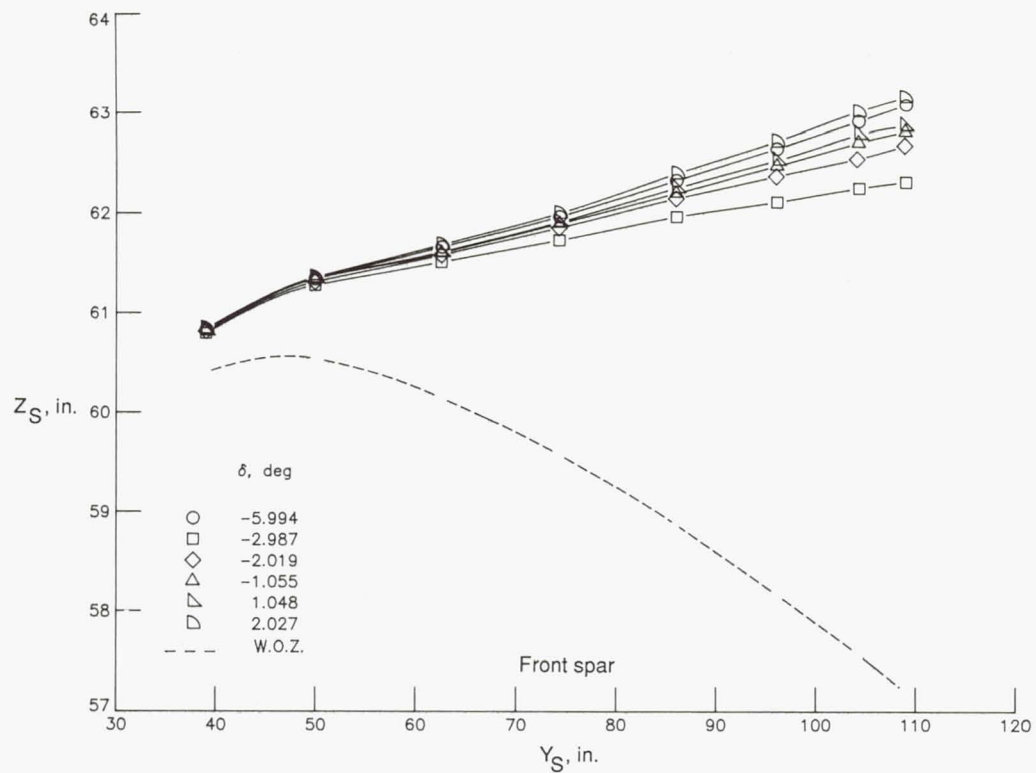
(d)  $M = 0.850$ .

Figure 14. Concluded.



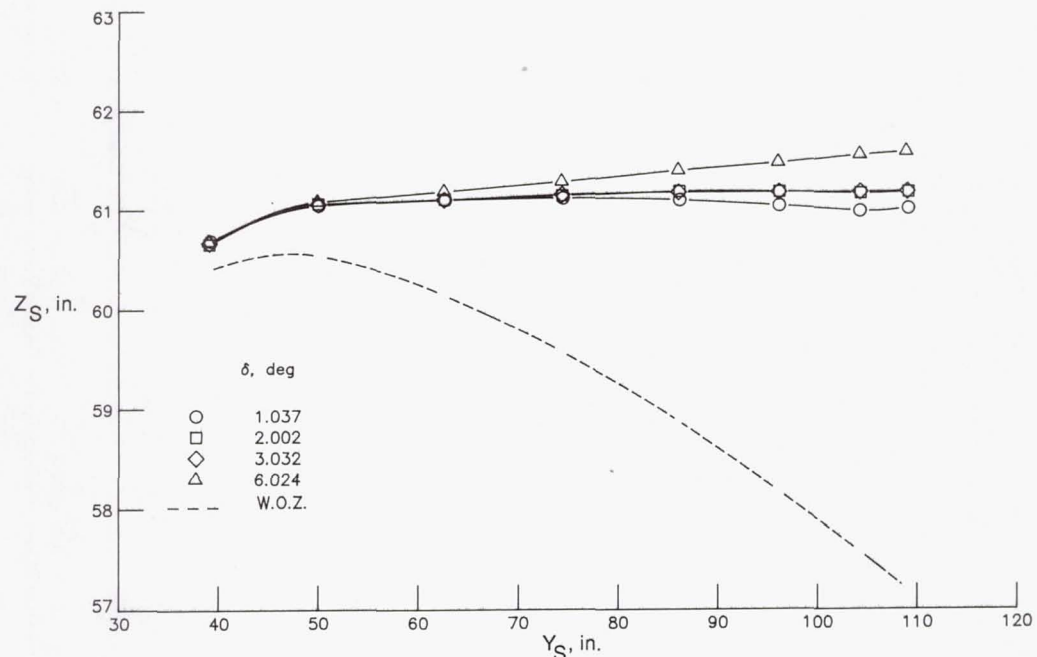
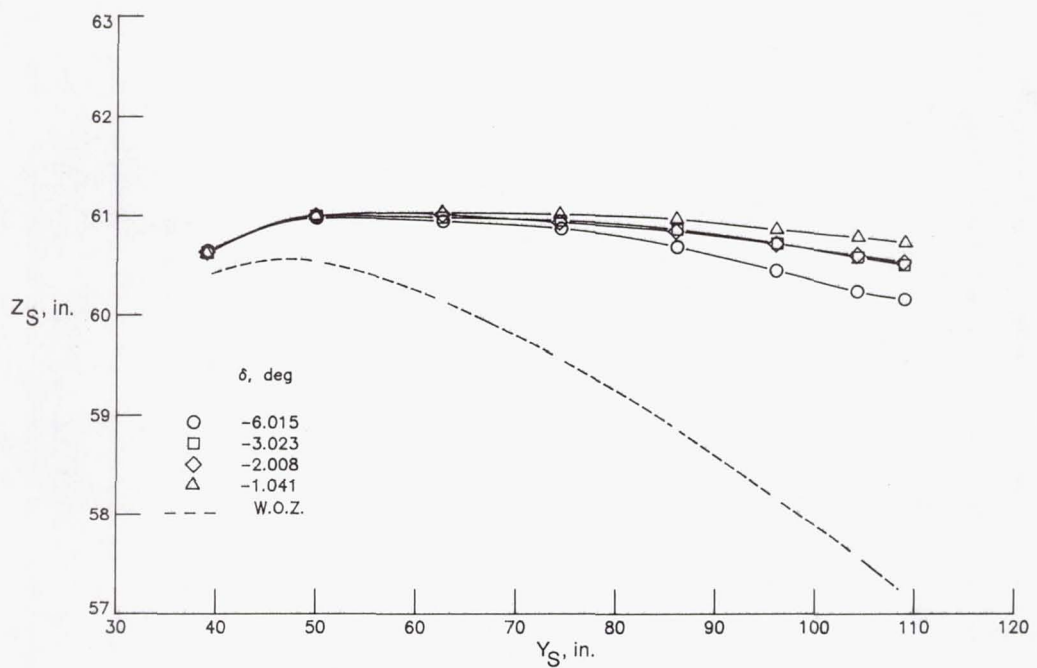
(a)  $\alpha = 0^\circ$ .

Figure 15. Variation of wing front and rear spar shapes with control surface deflection at two angles of attack,  $q = 200$  psf, and  $M = 0.600$ .



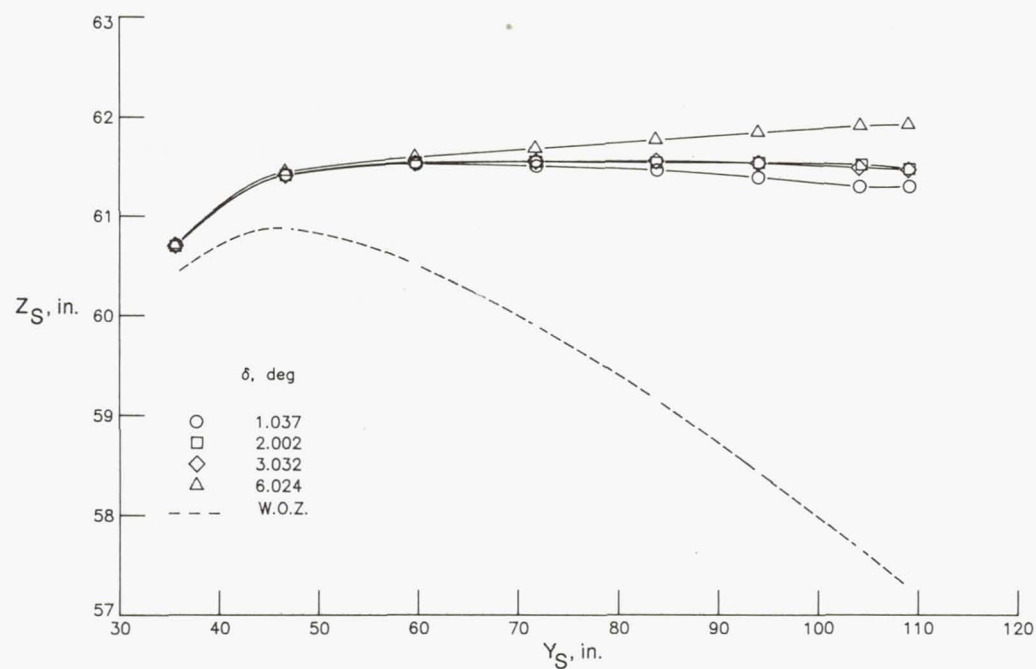
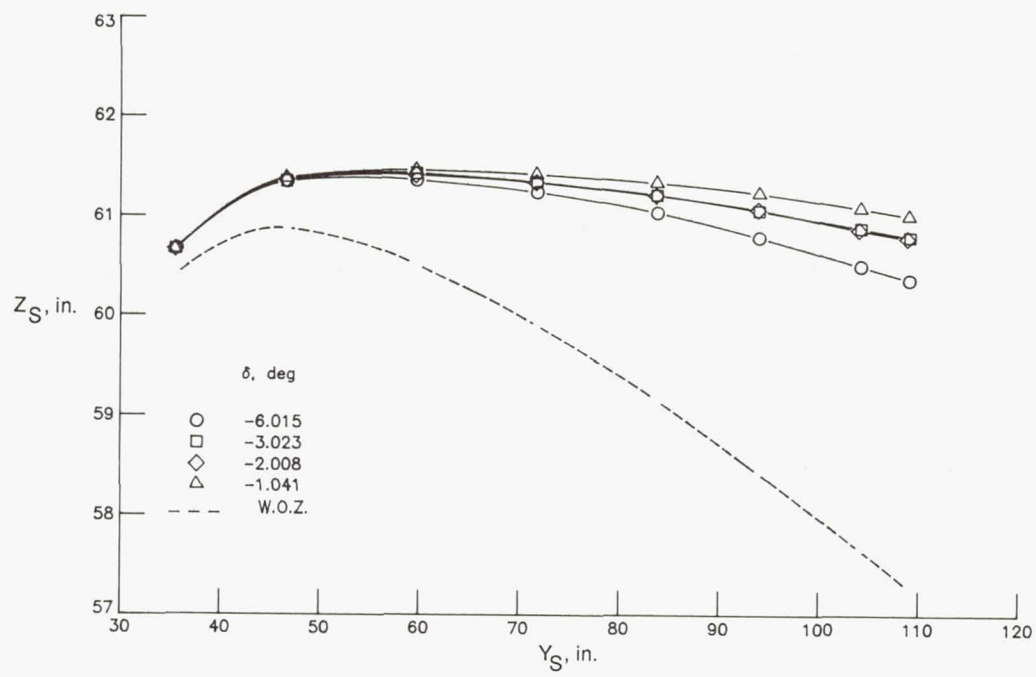
(b)  $\alpha = 2^\circ$ .

Figure 15. Concluded.



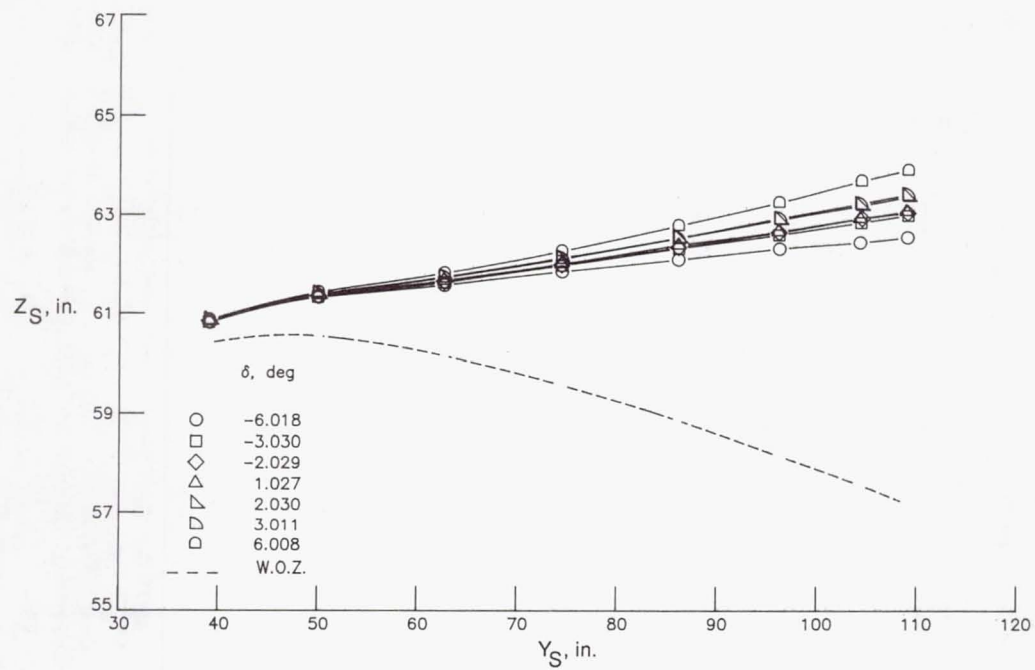
(a) Front spar;  $\alpha = 0^\circ$ .

Figure 16. Variation of wing front and rear spar shapes with control surface deflection at two angles of attack,  $q = 200$  psf, and  $M = 0.700$ .

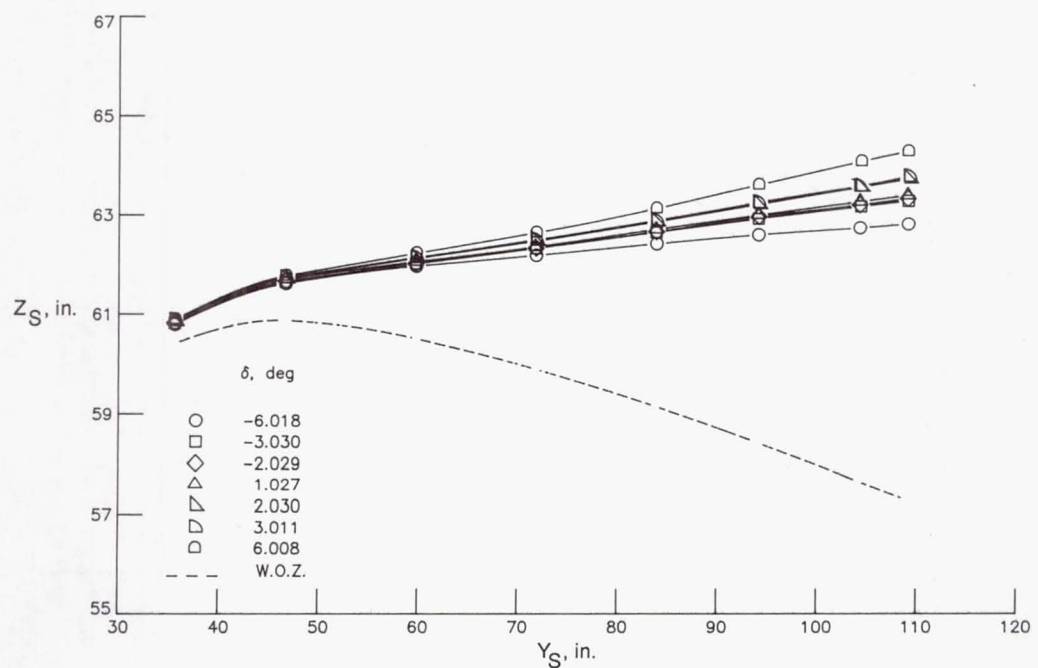


(b) Rear spar;  $\alpha = 0^\circ$ .

Figure 16. Continued.

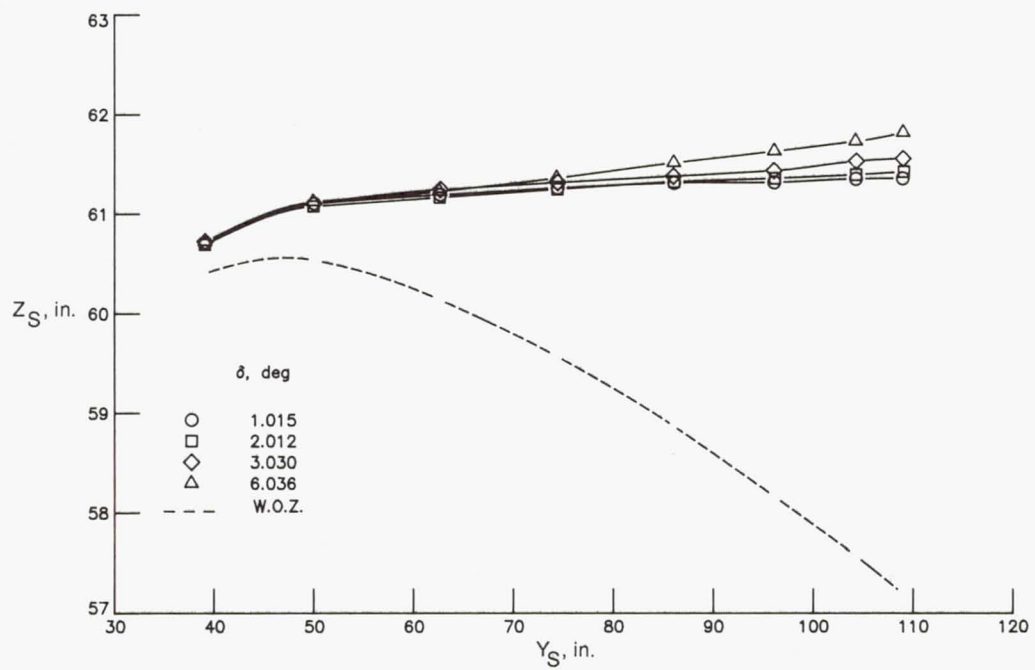
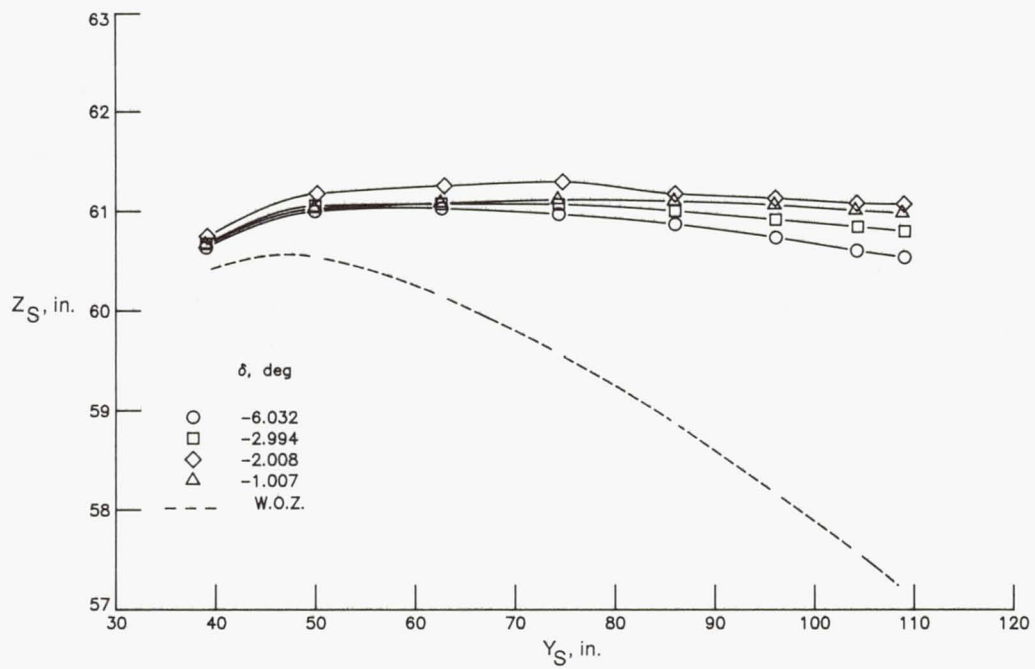


(c) Front spar;  $\alpha = 2^\circ$ .



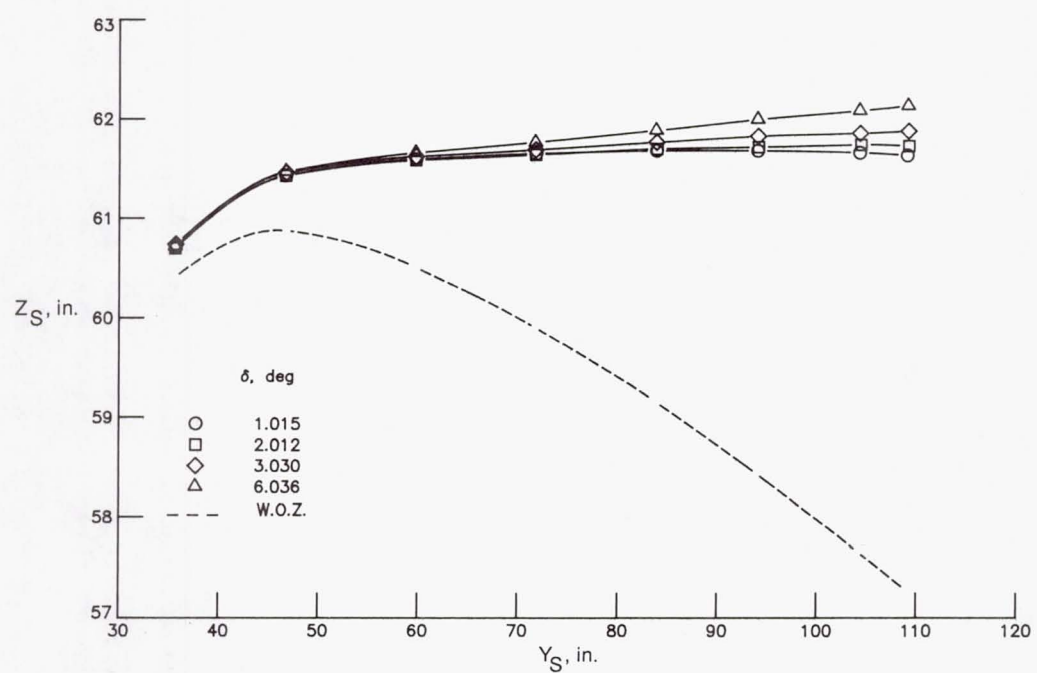
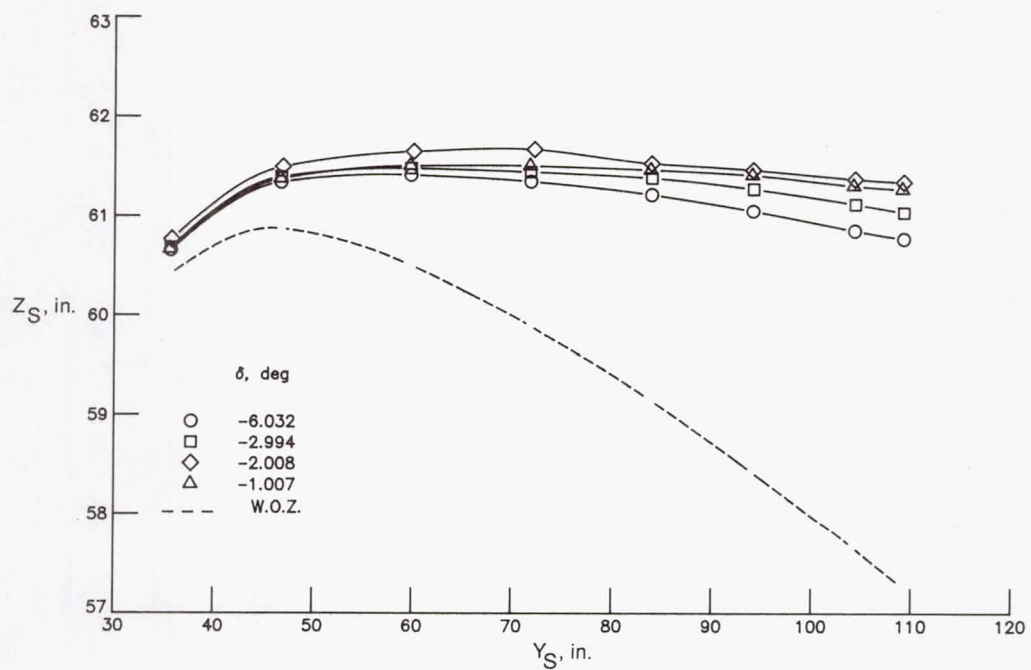
(d) Rear spar;  $\alpha = 2^\circ$ .

Figure 16. Concluded.



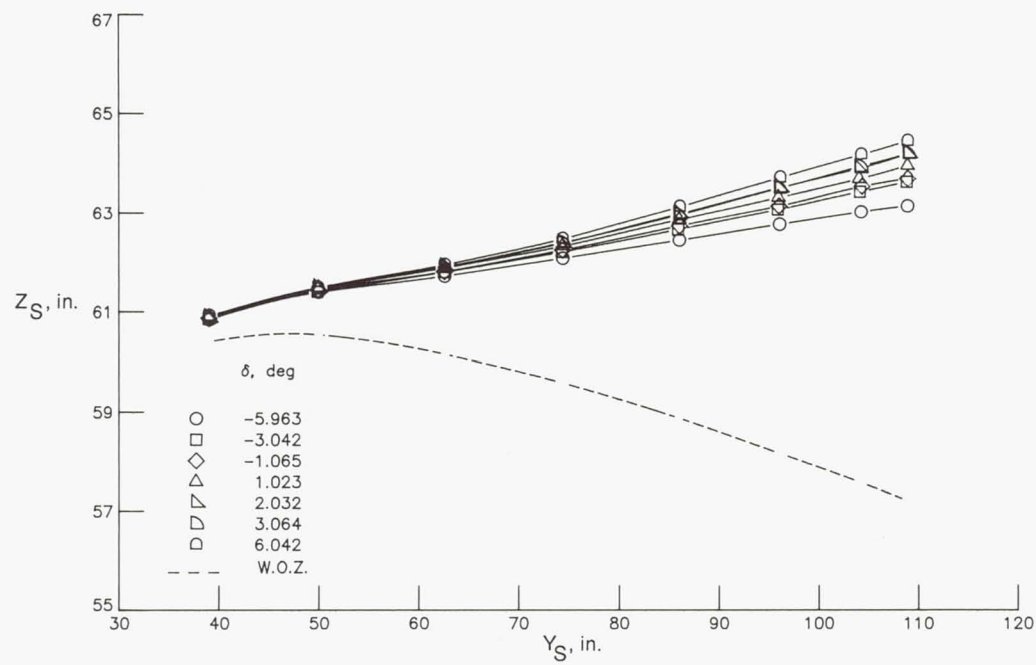
(a) Front spar;  $\alpha = 0^\circ$ .

Figure 17. Variation of wing front and rear spar shapes with control surface deflection at two angles of attack,  $q = 200$  psf, and  $M = 0.800$ .

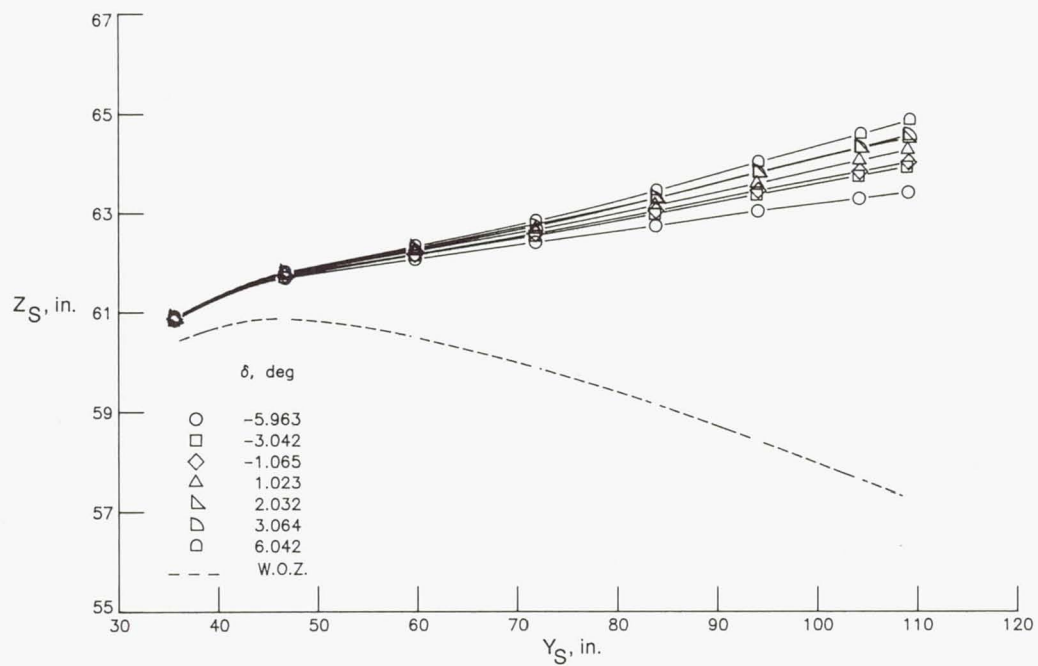


(b) Rear spar;  $\alpha = 0^\circ$ .

Figure 17. Continued.

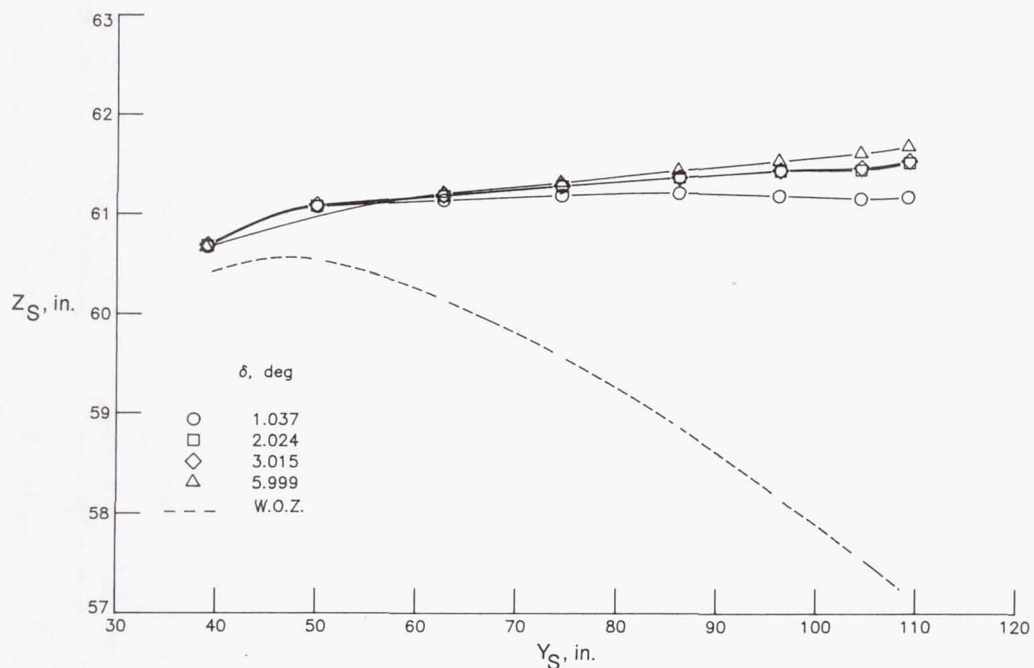
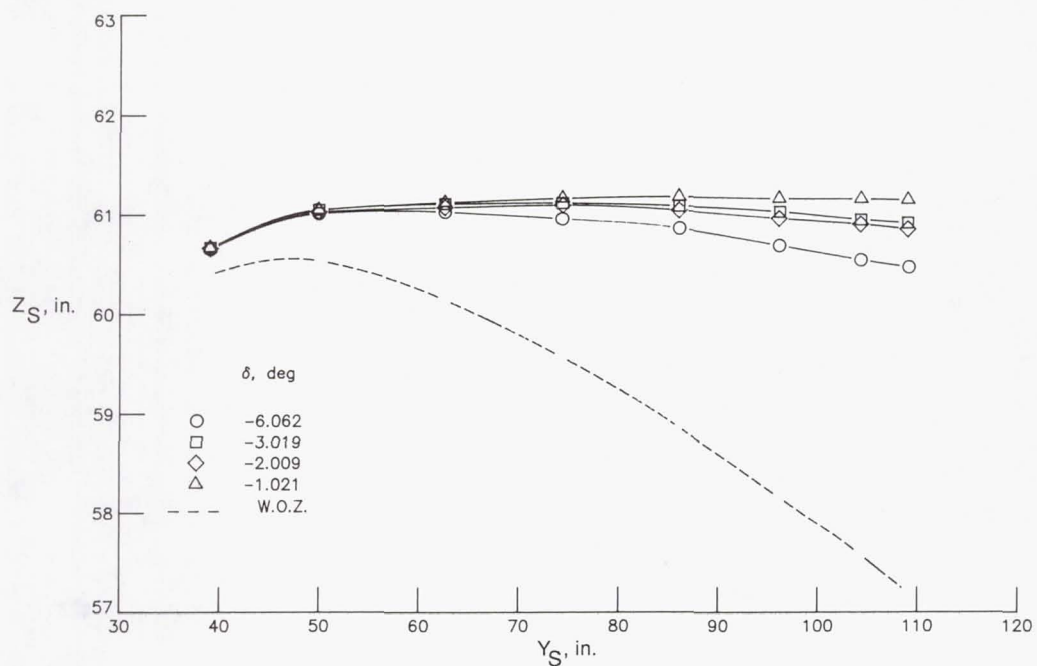


(c) Front spar;  $\alpha = 2^\circ$ .



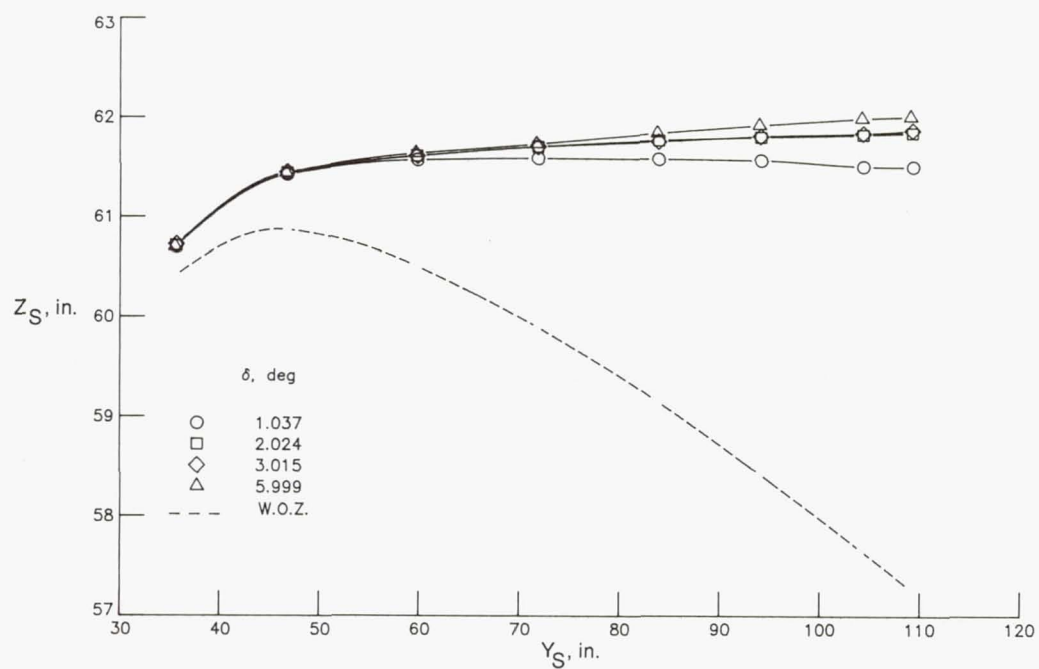
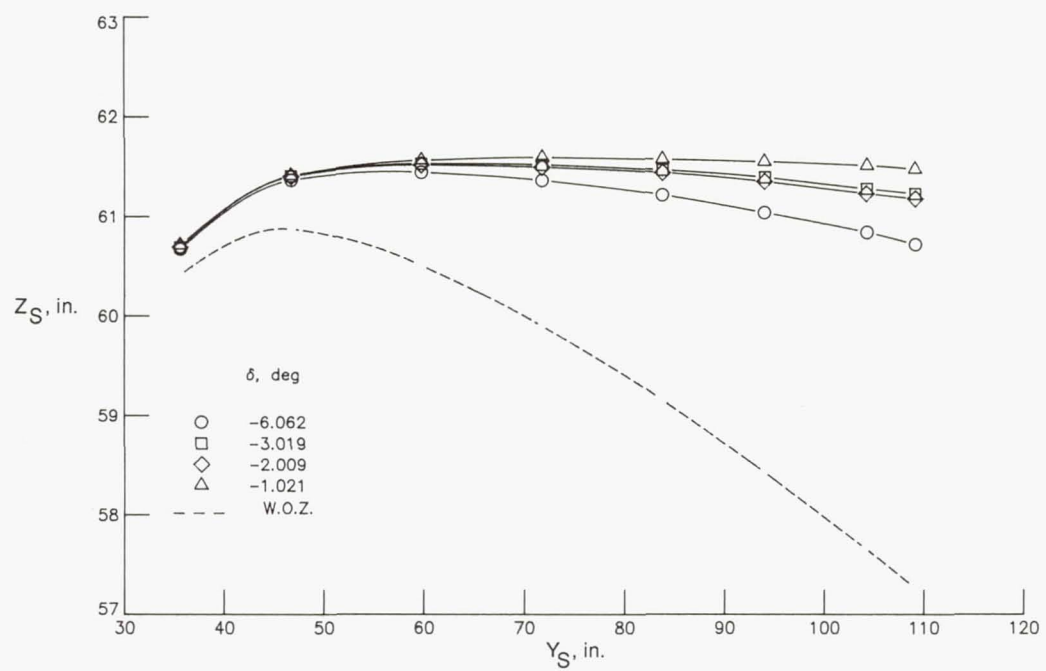
(d) Rear spar;  $\alpha = 2^\circ$ .

Figure 17. Concluded.



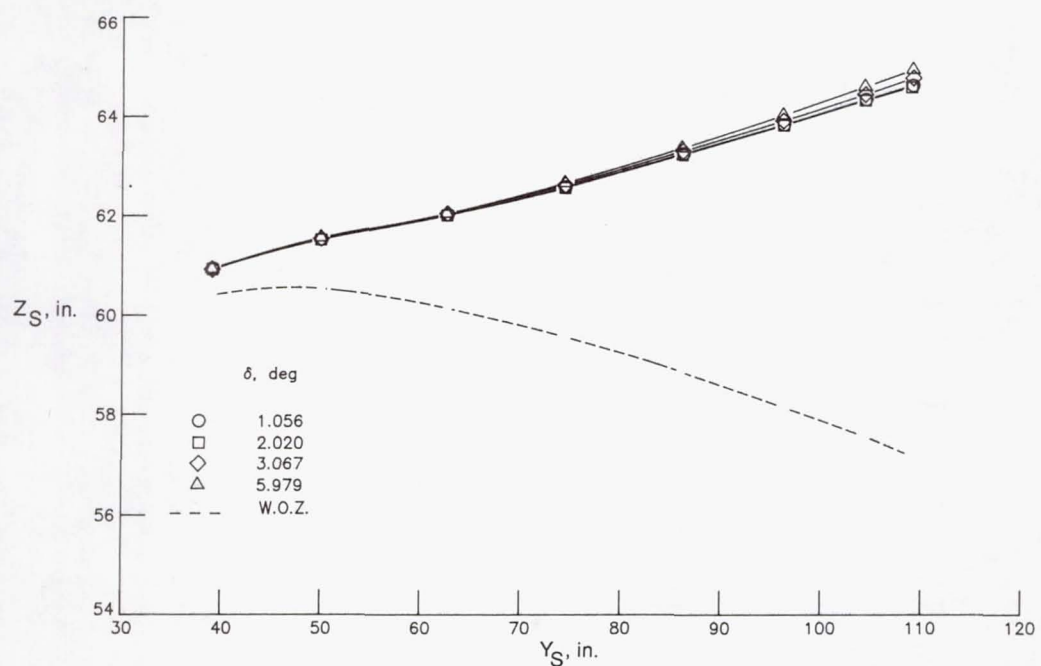
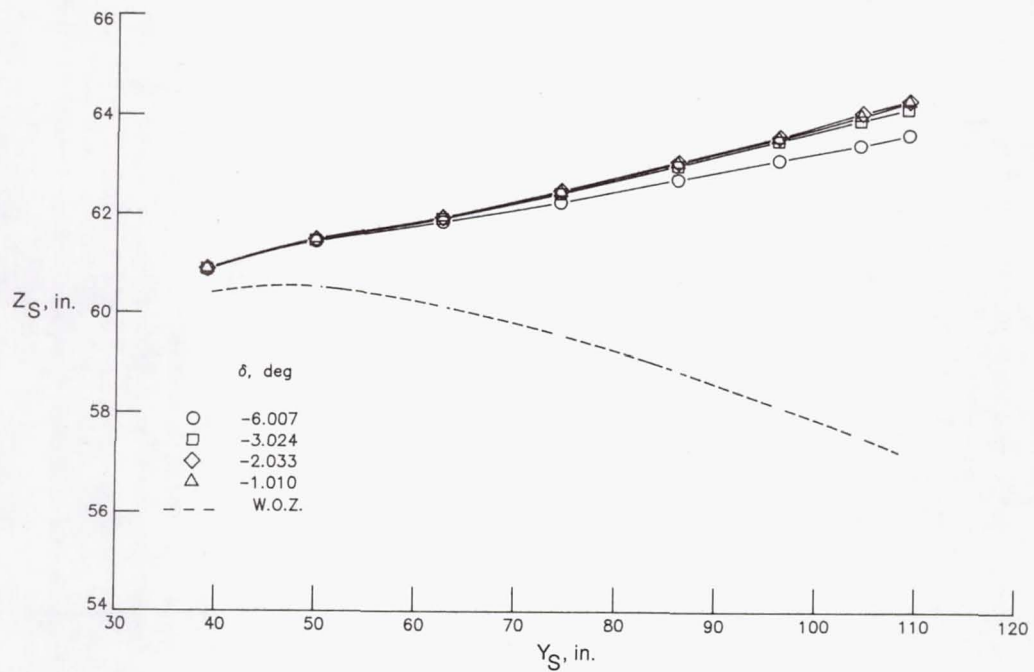
(a) Front spar;  $\alpha = 0^\circ$ .

Figure 18. Variation of wing front and rear spar shapes with control surface deflection at two angles of attack,  $q = 200$  psf, and  $M = 0.850$ .



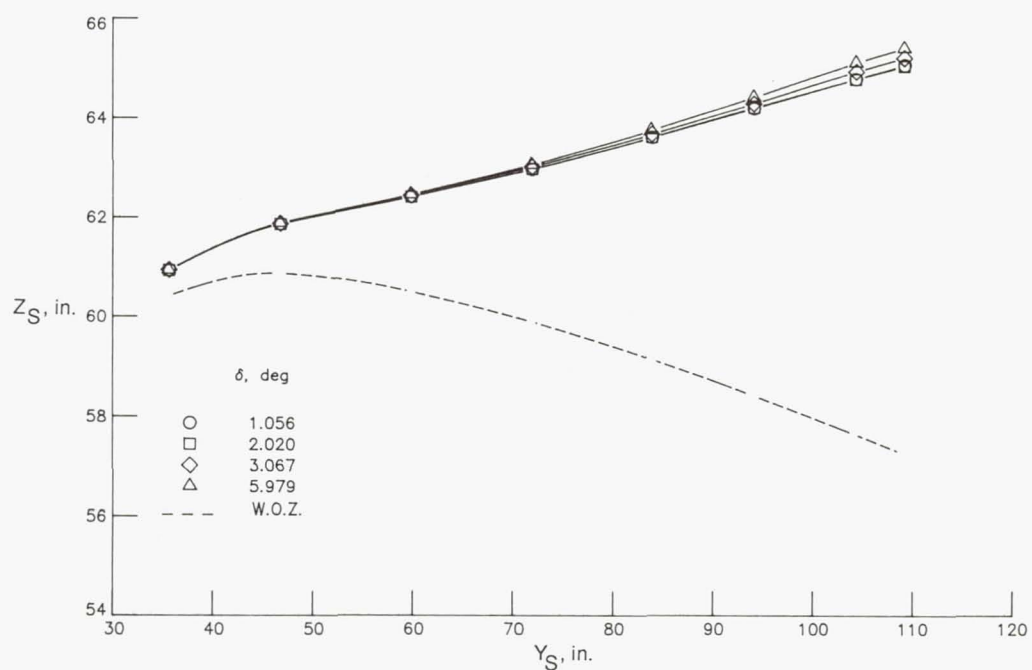
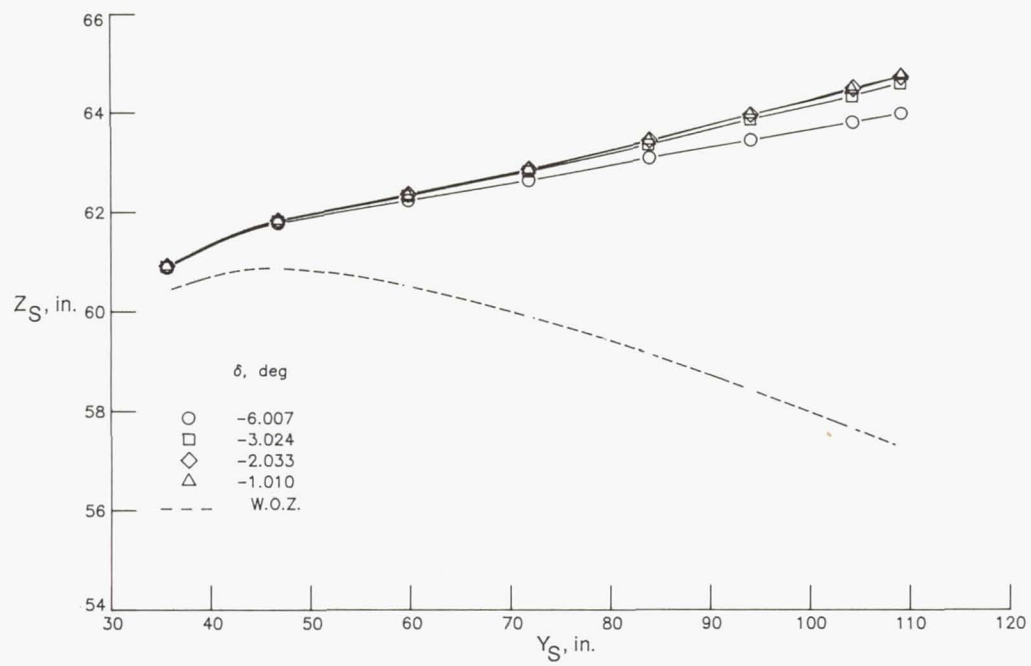
(b) Rear spar;  $\alpha = 0^\circ$ .

Figure 18. Continued.



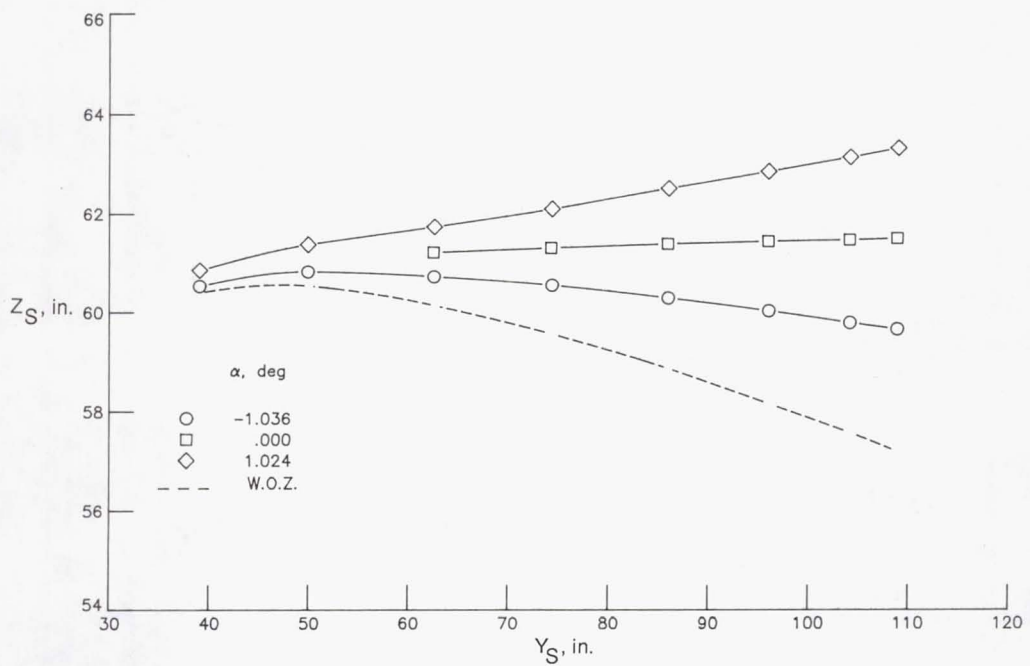
(c) Front spar;  $\alpha = 2^\circ$ .

Figure 18. Continued.

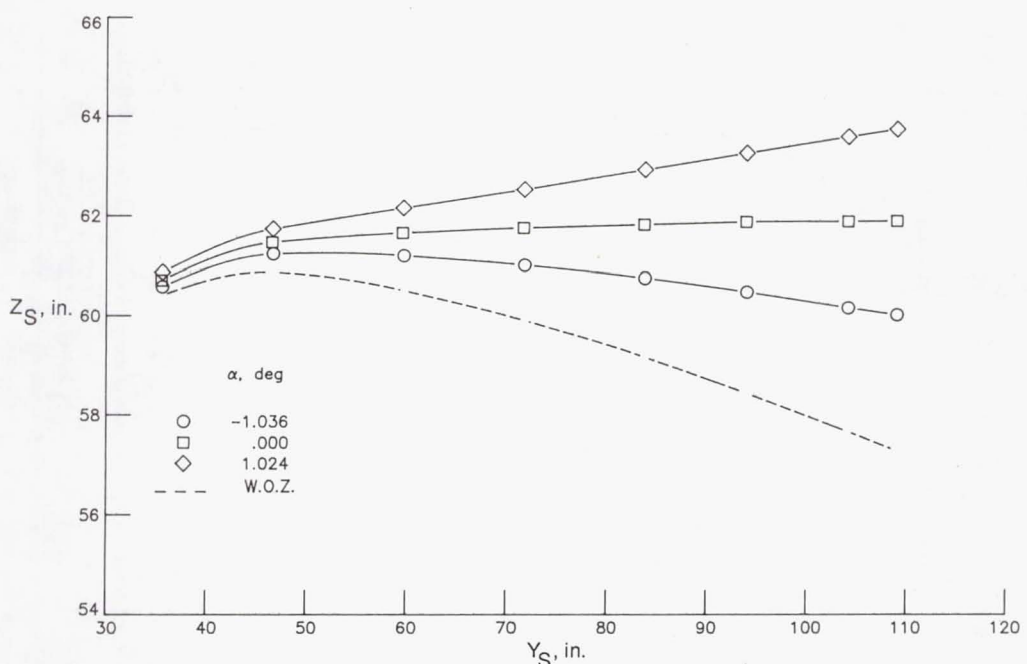


(d) Rear spar;  $\alpha = 2^\circ$ .

Figure 18. Concluded.

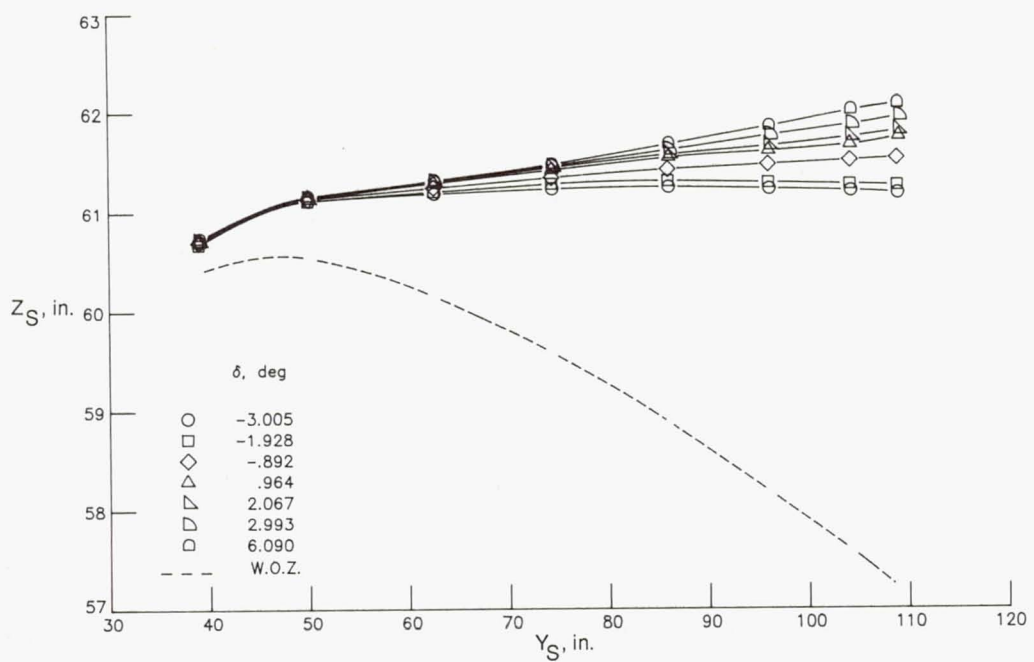


(a) Front spar.

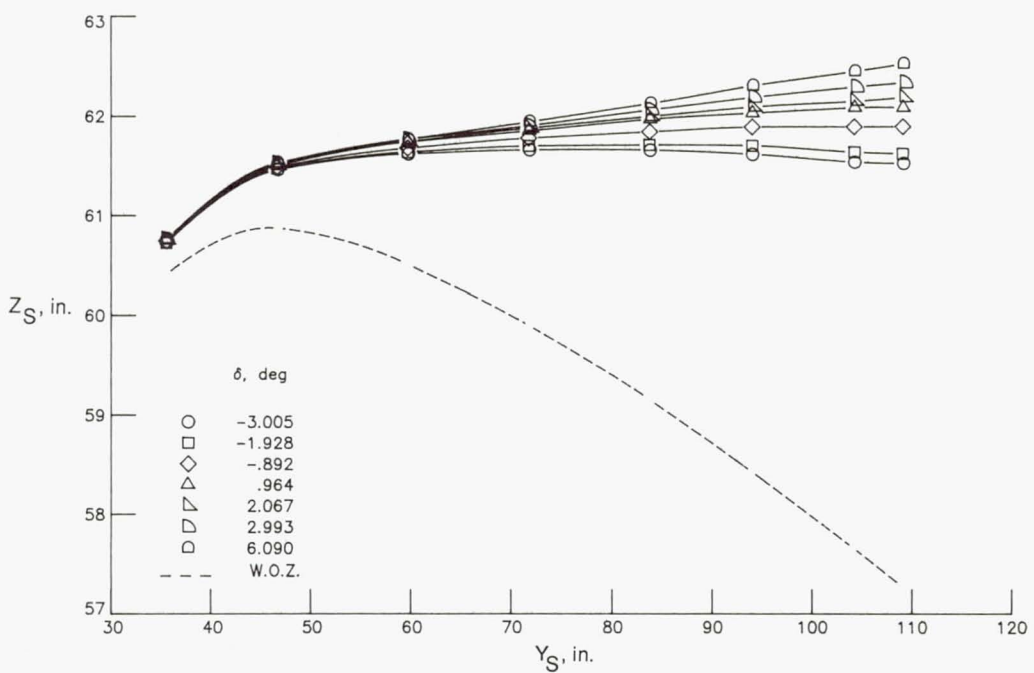


(b) Rear spar.

Figure 19. Variation of wing front and rear spar shapes with angle of attack at  $M = 0.800$  and  $q = 300$  psf.

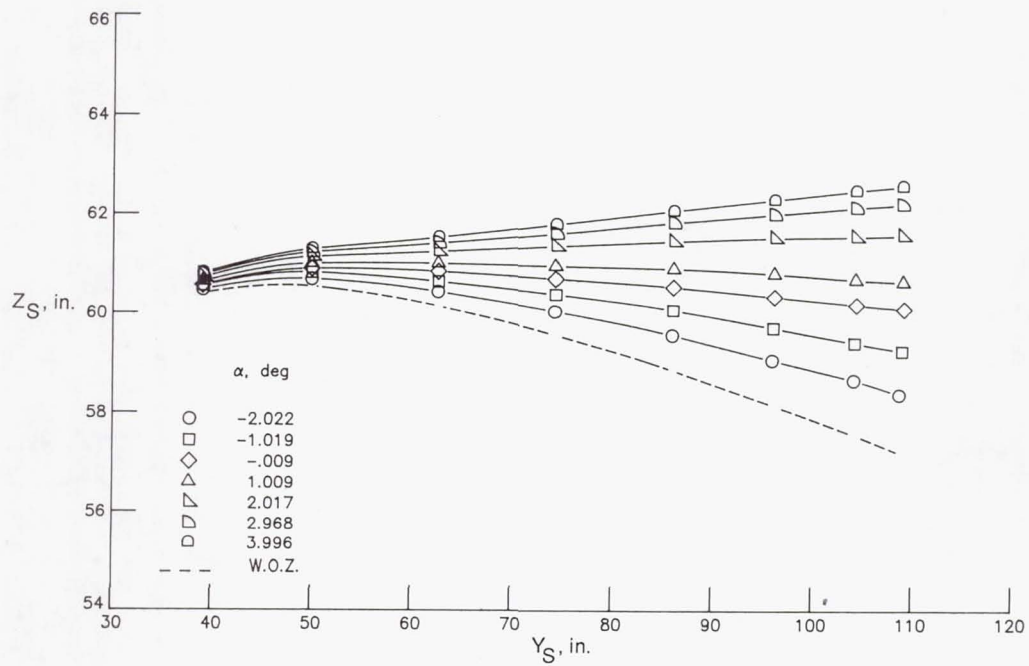


(a) Front spar.

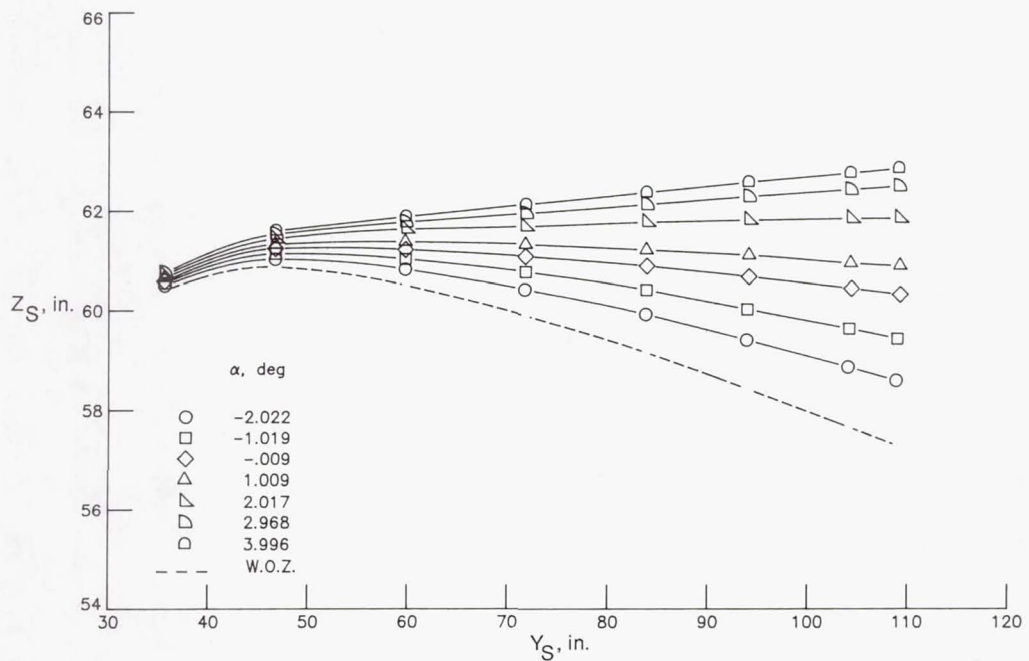


(b) Rear spar.

Figure 20. Variation of wing front and rear spar shapes with control surface deflection at  $\alpha = 0^\circ$ ,  $q = 300$  psf, and  $M = 0.800$ .

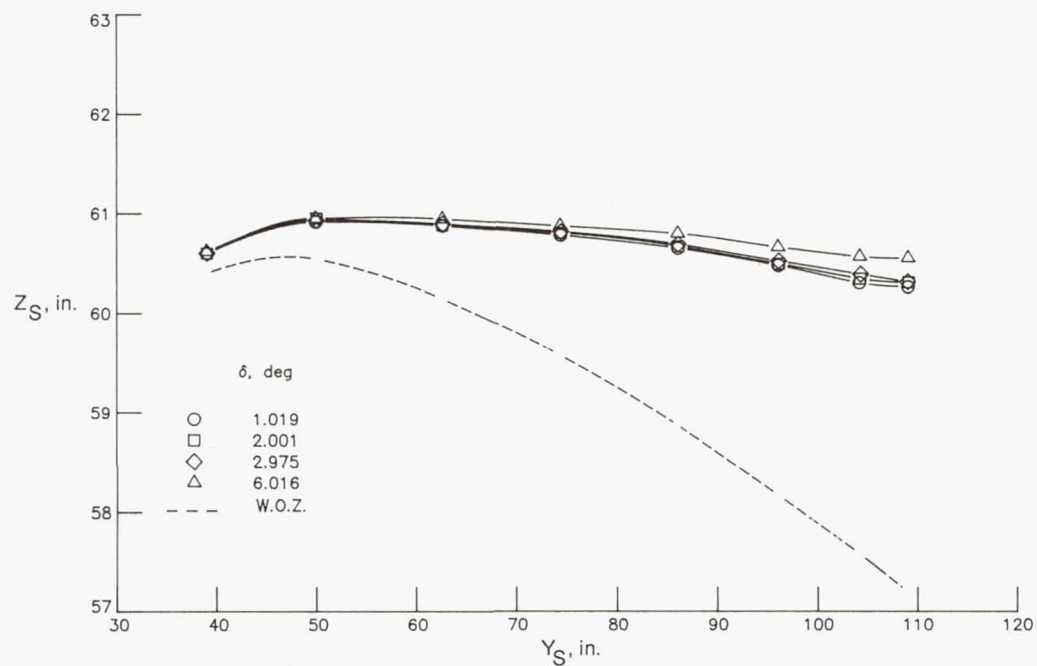
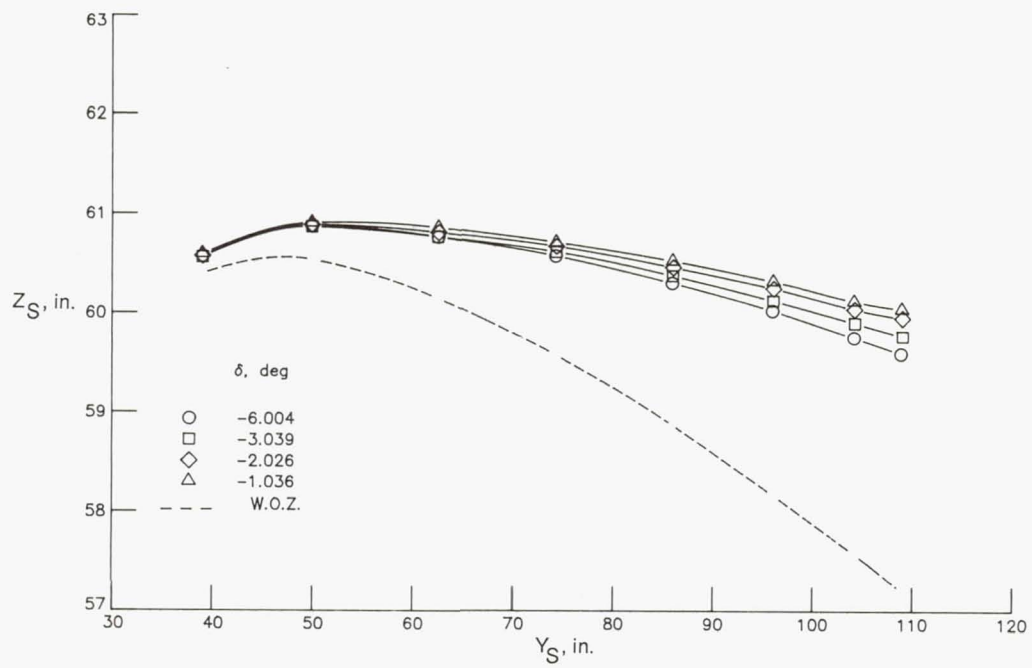


(a) Front spar.



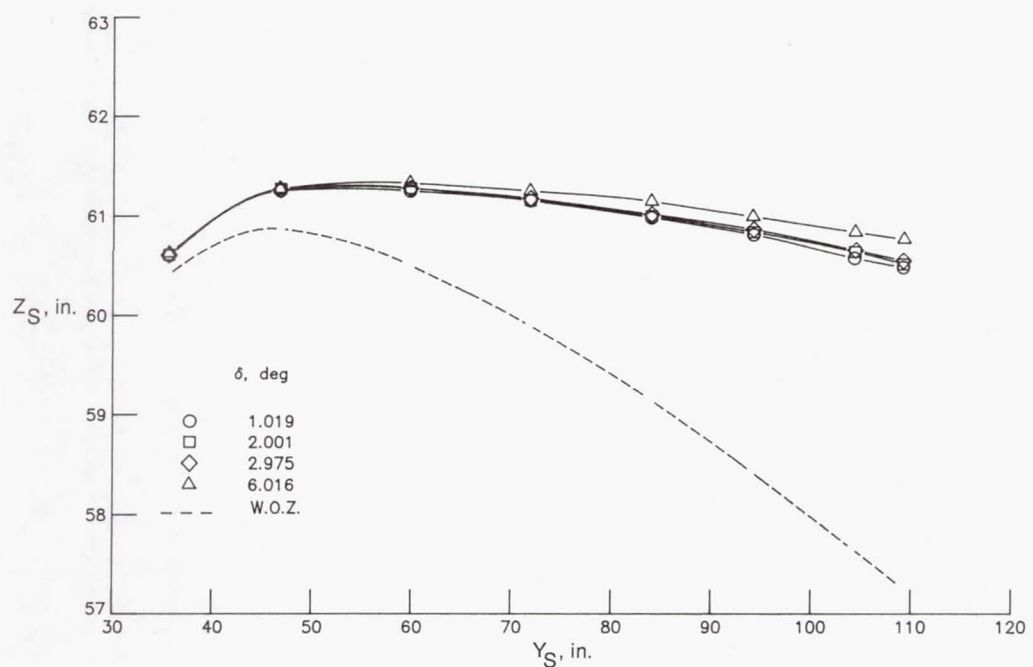
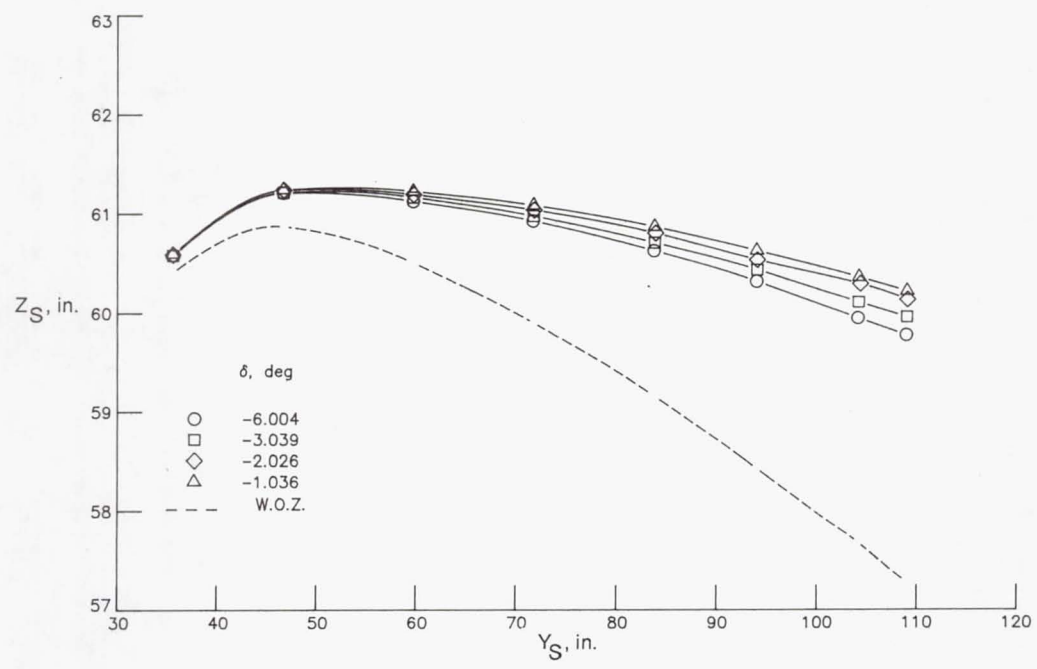
(b) Rear spar.

Figure 21. Variation of wing front and rear spar shapes with angle of attack at  $M = 0.800$  and  $q = 100$  psf in air.



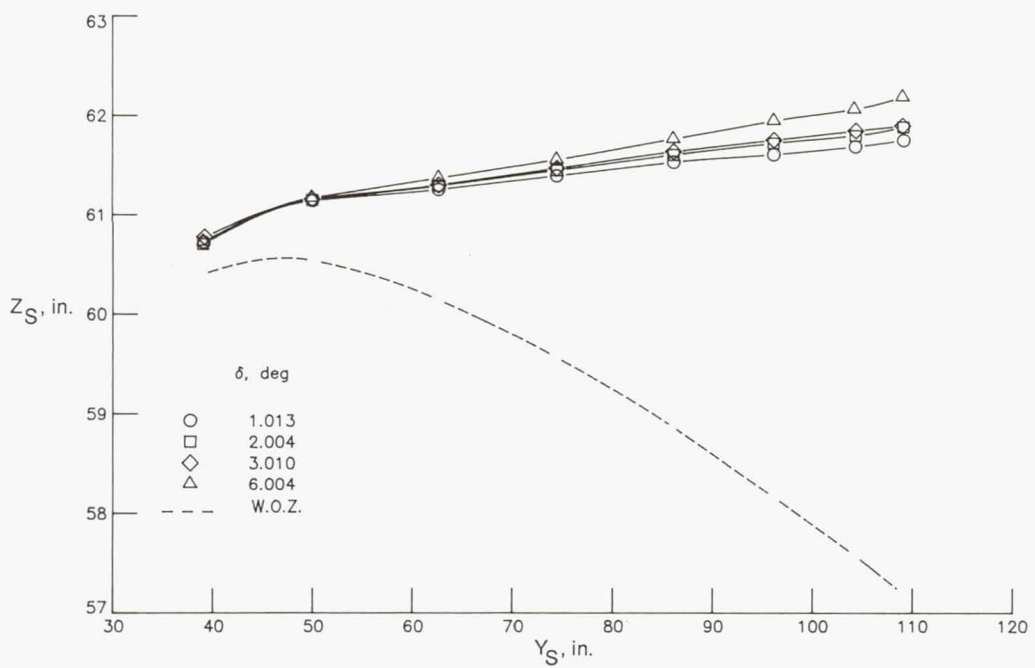
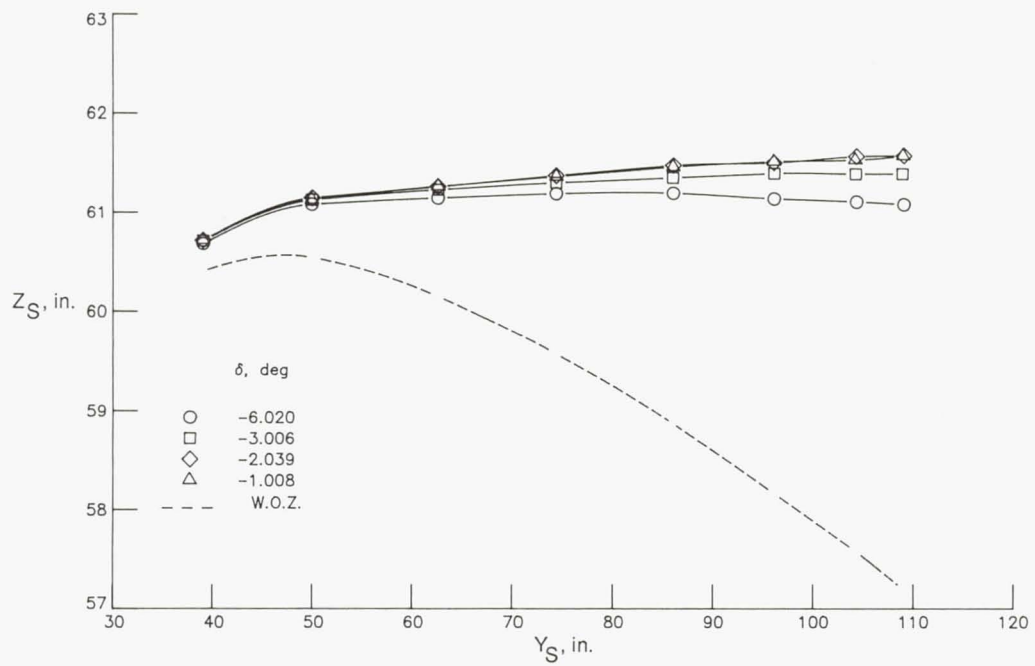
(a) Front spar;  $\alpha = 0^\circ$ .

Figure 22. Variation of wing front and rear spar shapes with control surface deflection at two angles of attack,  $q = 100$  psf, and  $M = 0.800$  in air.



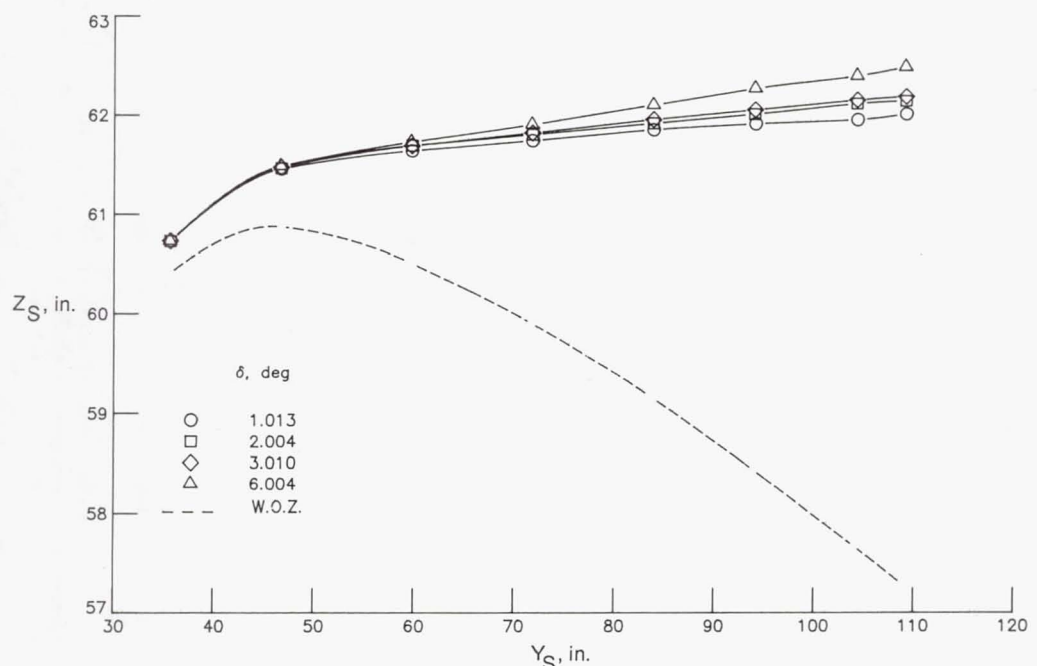
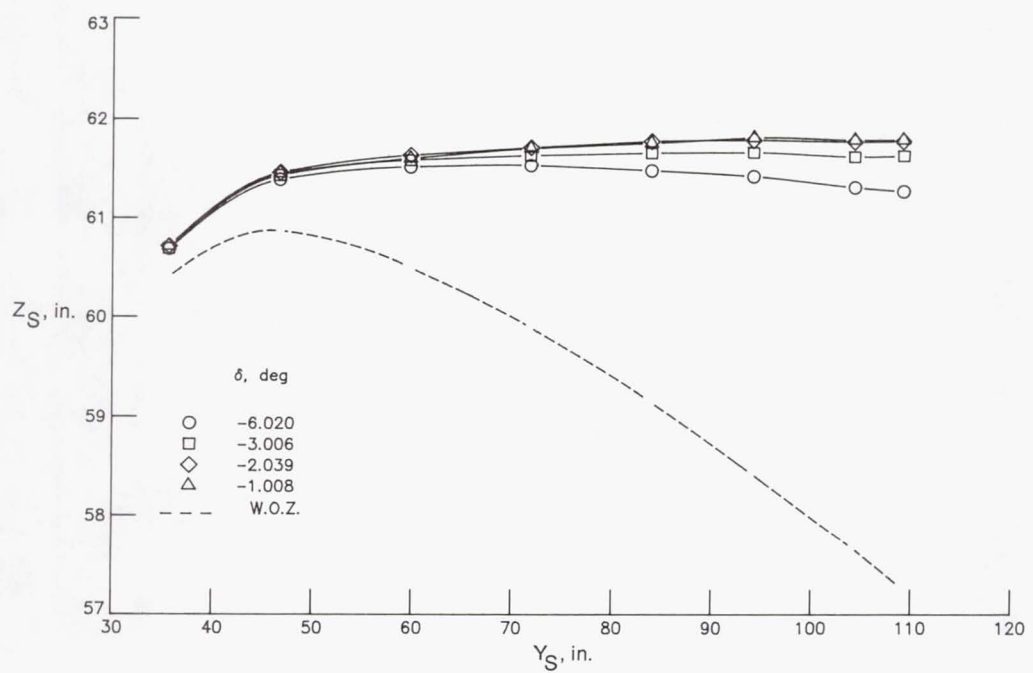
(b) Rear spar;  $\alpha = 0^\circ$ .

Figure 22. Continued.



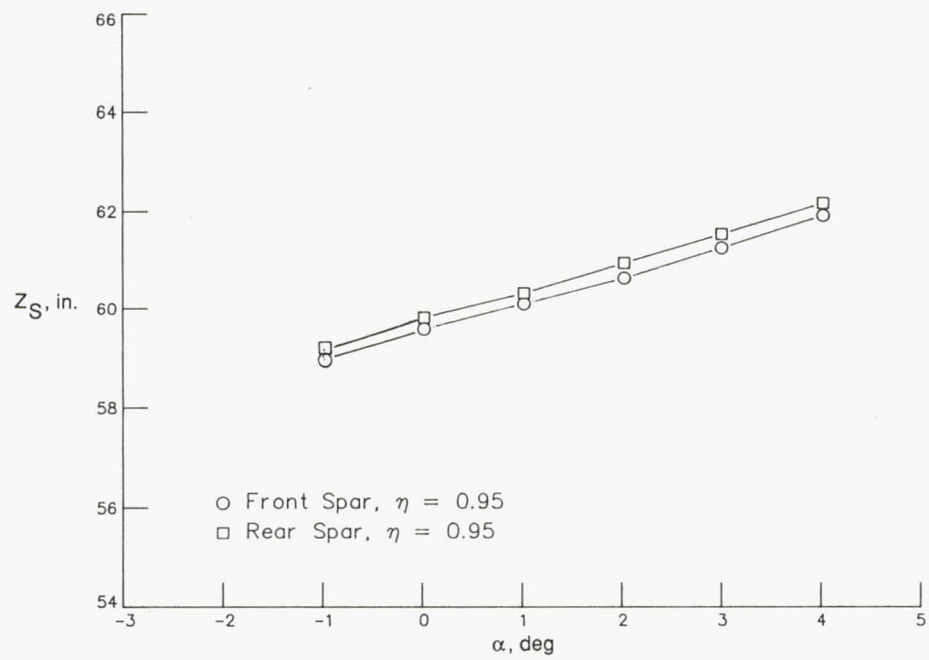
(c) Front spar;  $\alpha = 2^\circ$ .

Figure 22. Continued.

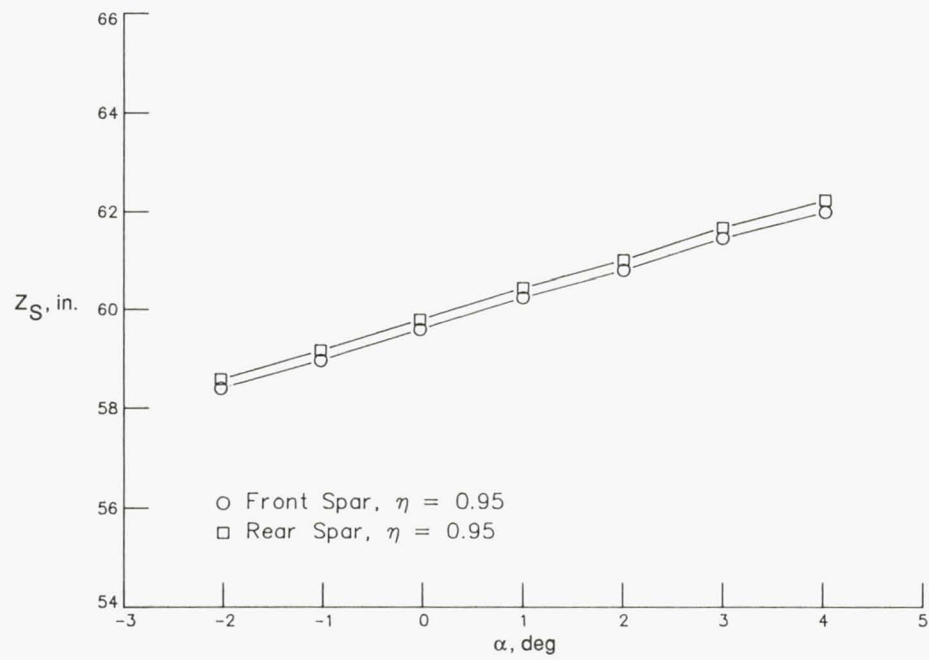


(d) Rear spar;  $\alpha = 2^\circ$ .

Figure 22. Concluded.

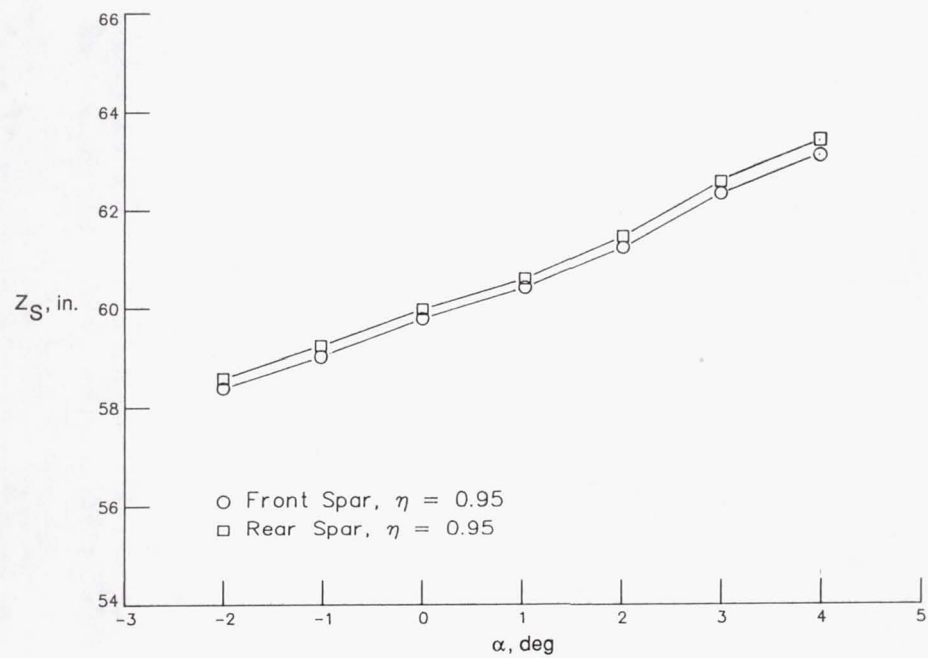


(a)  $M = 0.600$ .

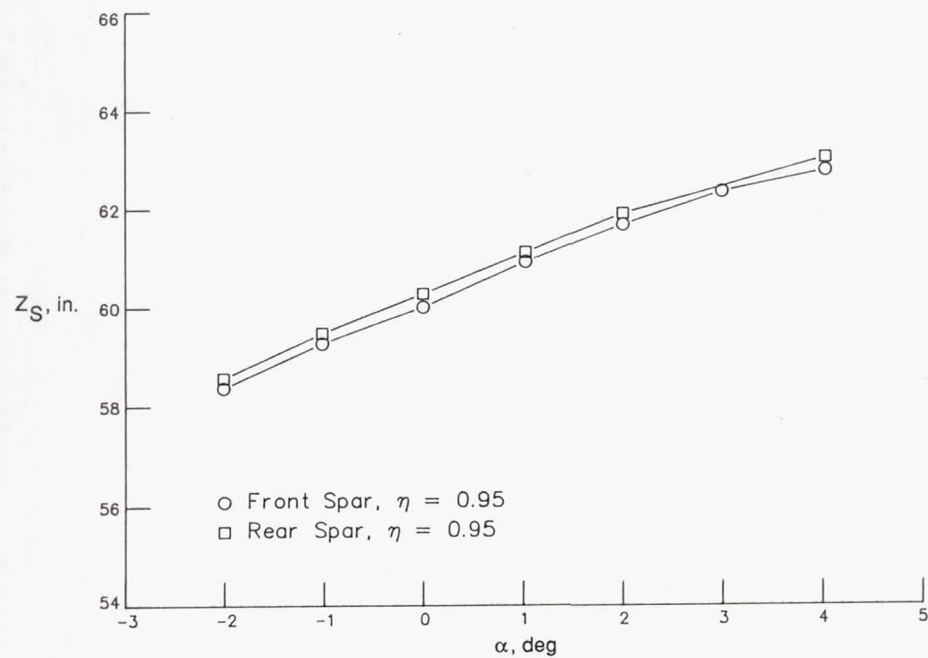


(b)  $M = 0.700$ .

Figure 23. Variation of wing front and rear spar tip deflection with angle of attack at four Mach numbers and  $q = 100$  psf.

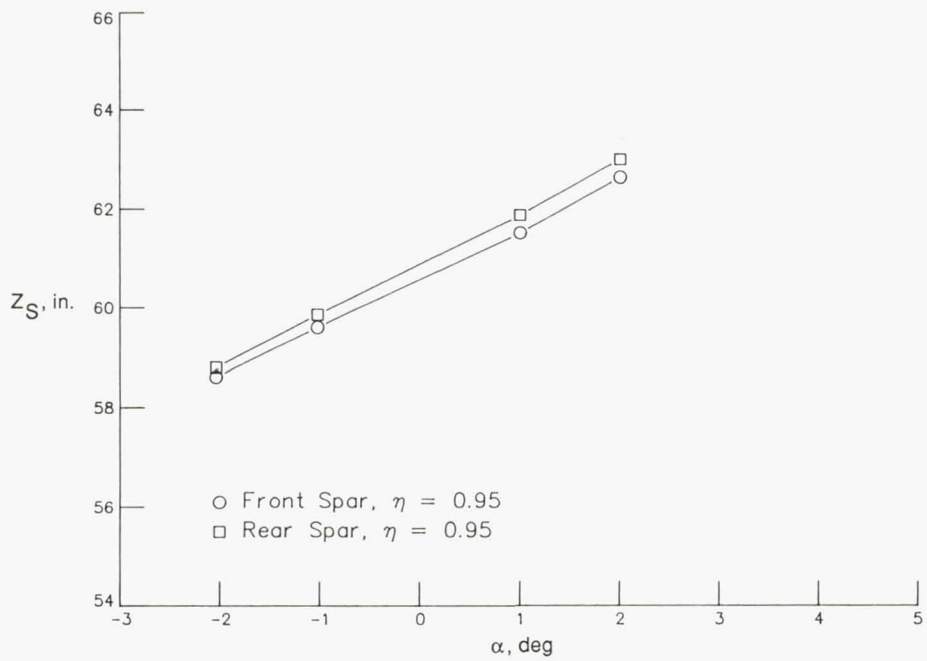


(c)  $M = 0.800$ .

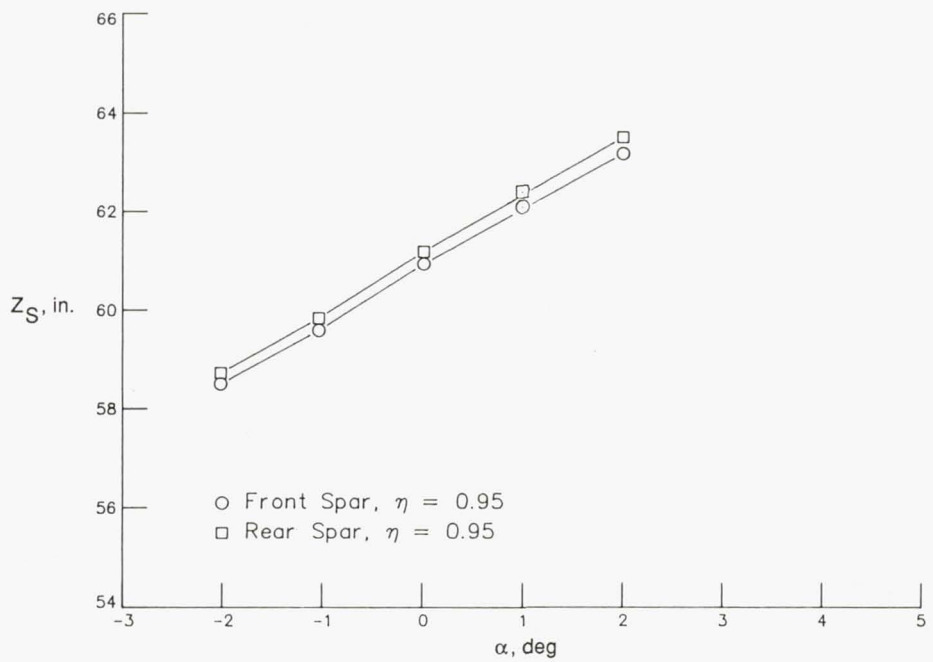


(d)  $M = 0.850$ .

Figure 23. Concluded.

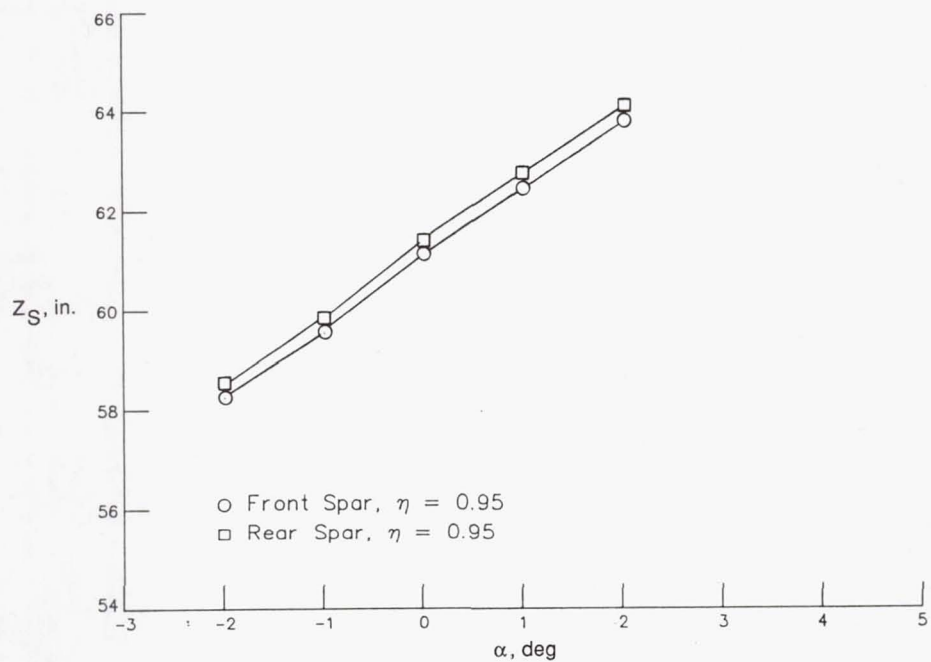


(a)  $M = 0.600$ .

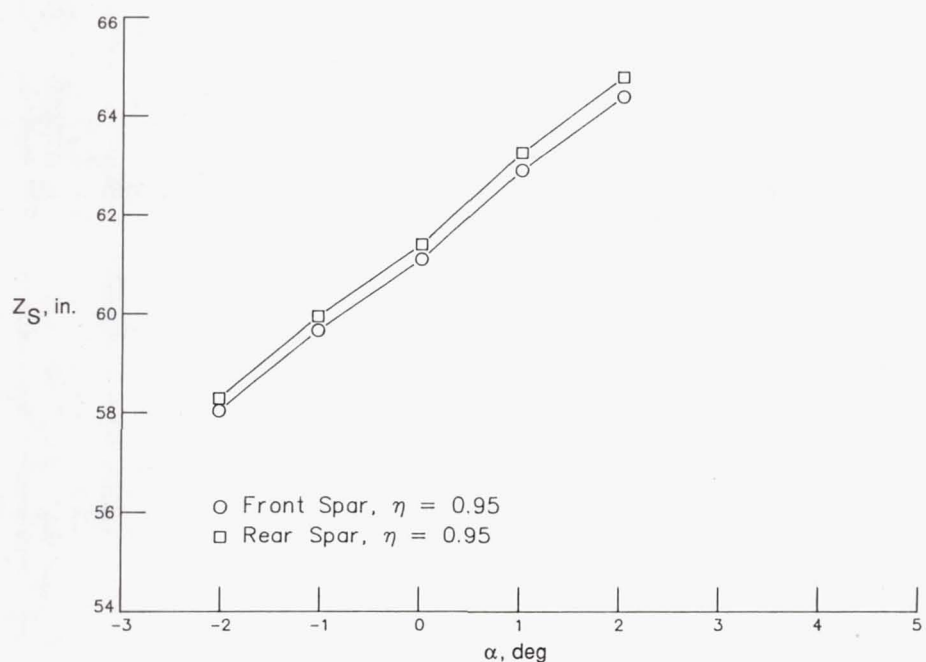


(b)  $M = 0.700$ .

Figure 24. Variation of wing front and rear spar tip deflection with angle of attack at four Mach numbers and  $q = 200 \text{ psf}$ .



(c)  $M = 0.800$ .



(d)  $M = 0.850$ .

Figure 24. Concluded.

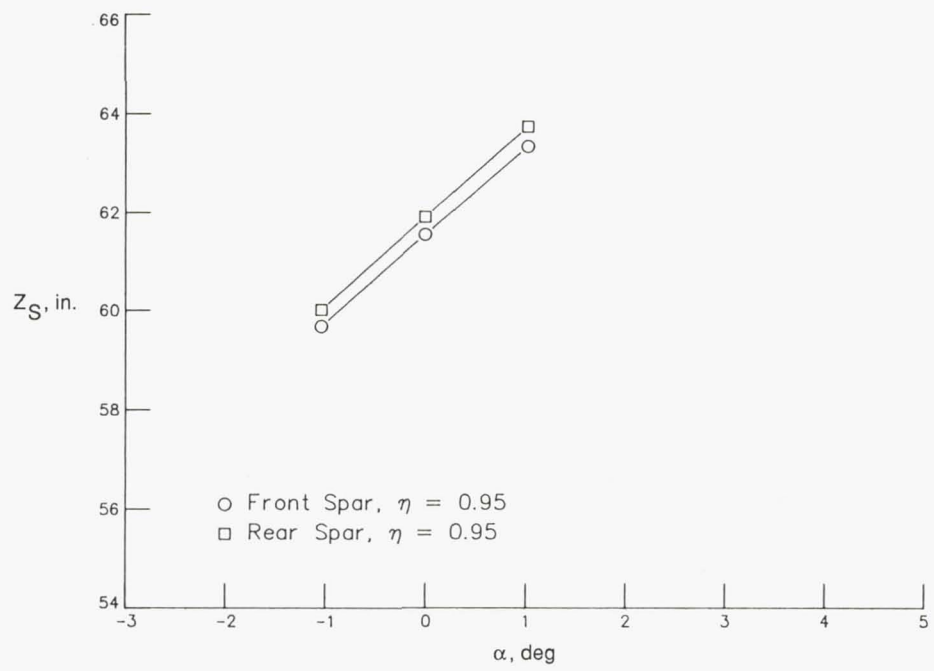
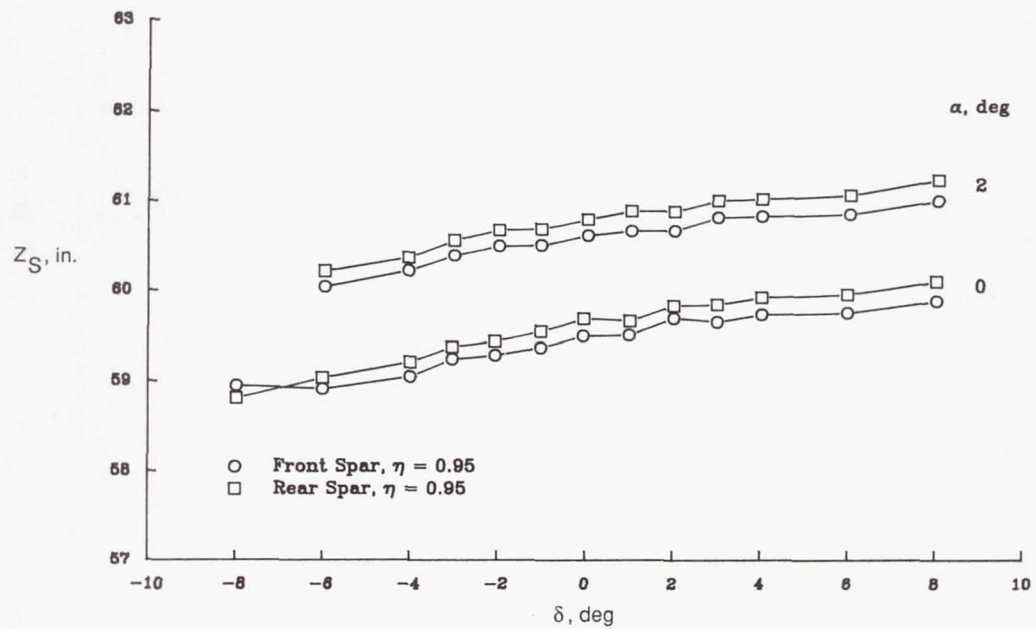
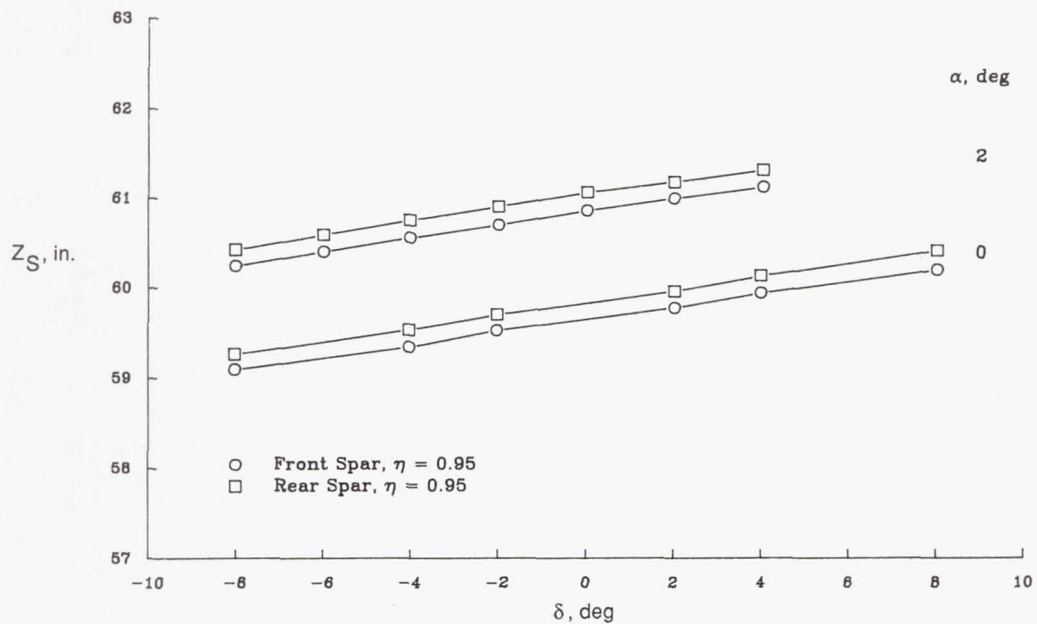


Figure 25. Variation of wing front and rear spar tip deflection with angle of attack at  $M = 0.800$  and  $q = 300$  psf.

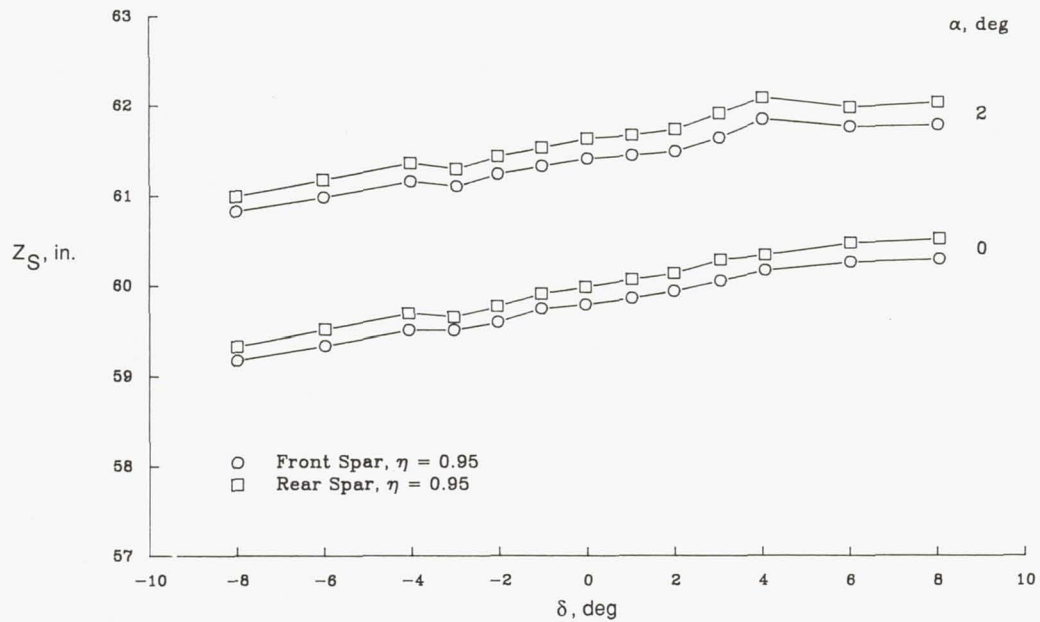


(a)  $M = 0.600$ .

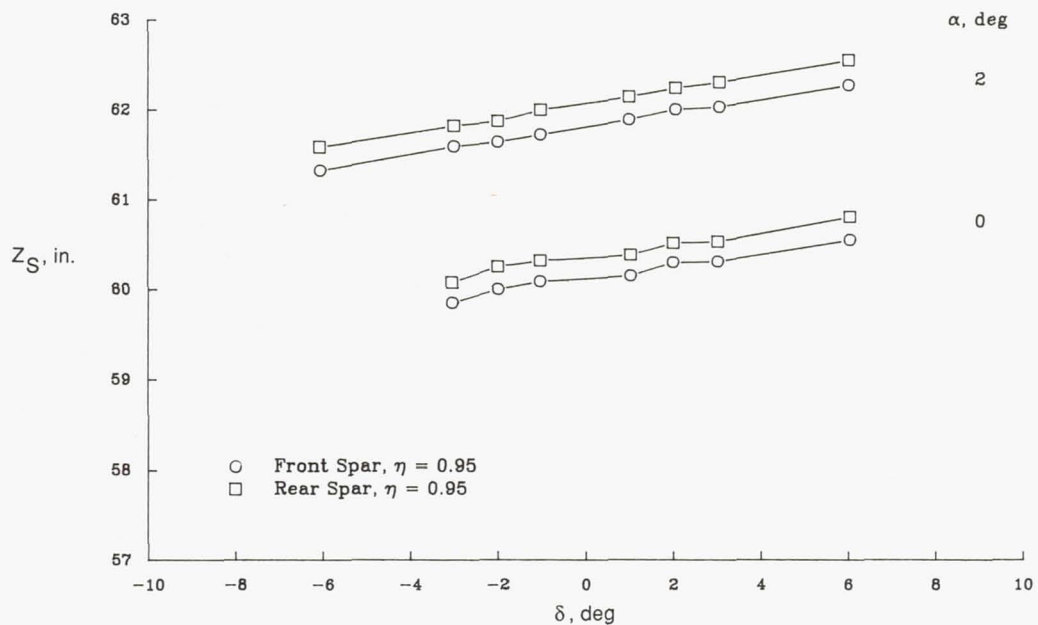


(b)  $M = 0.700$ .

Figure 26. Variation of wing front and rear spar tip deflection with control surface deflection at five Mach numbers, two angles of attack, and  $q = 100$  psf.

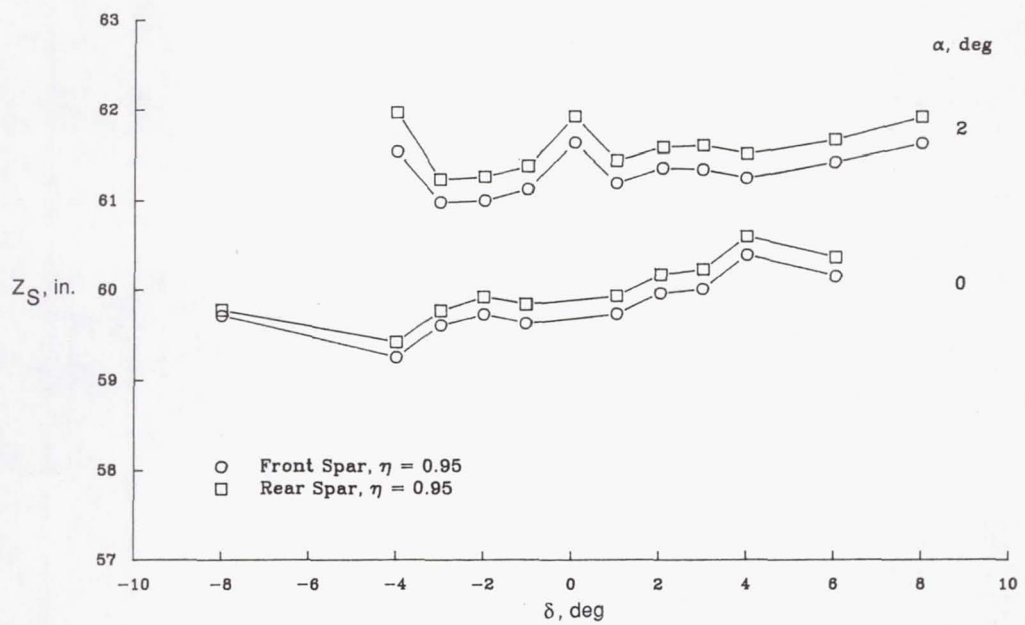


(c)  $M = 0.800$ .



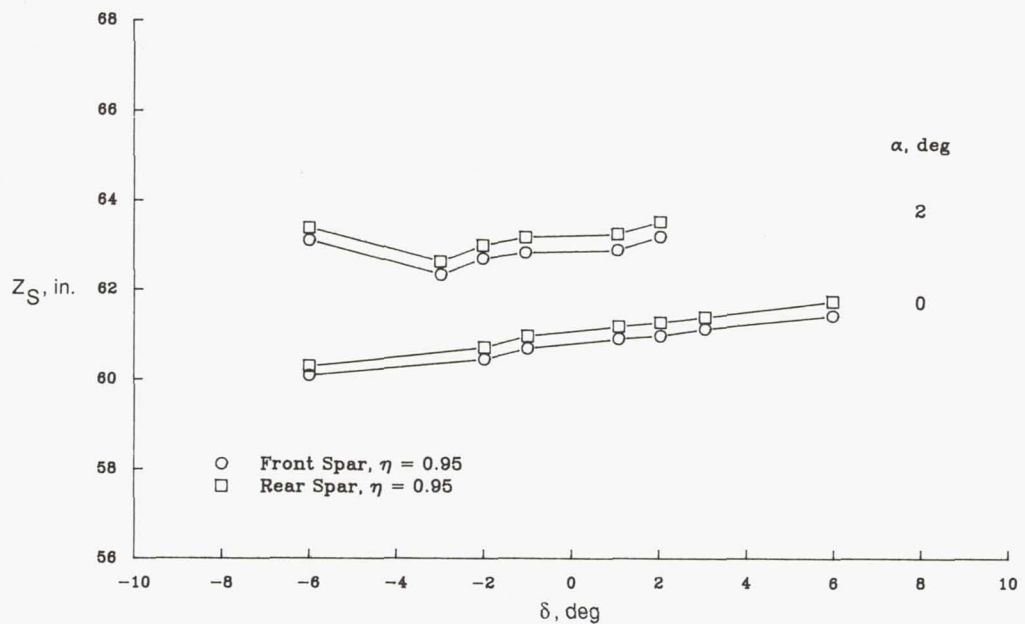
(d)  $M = 0.850$ .

Figure 26. Continued.

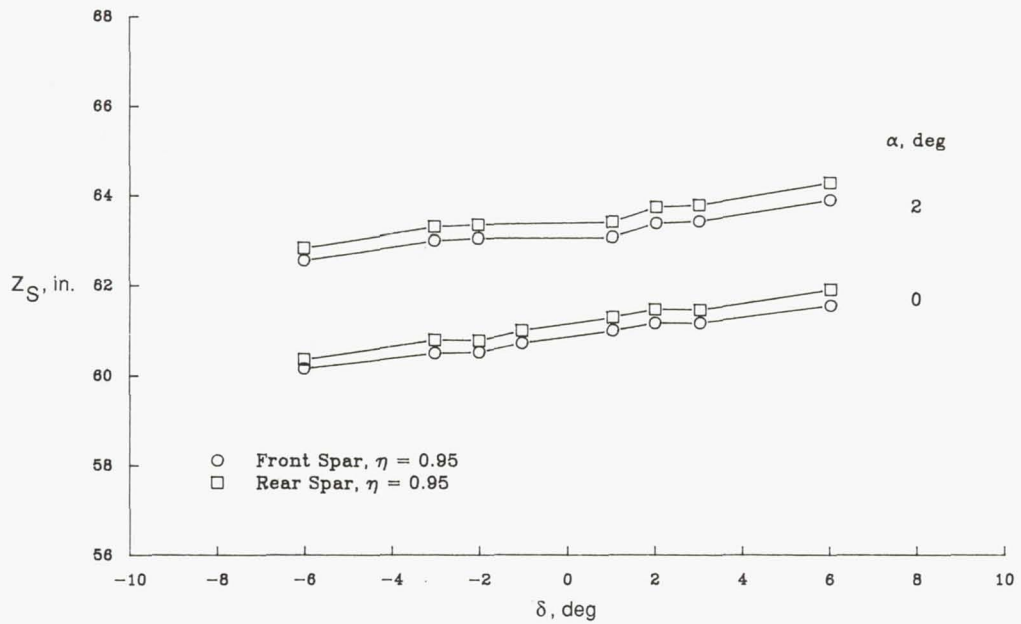


(e)  $M = 0.880$ .

Figure 26. Concluded.

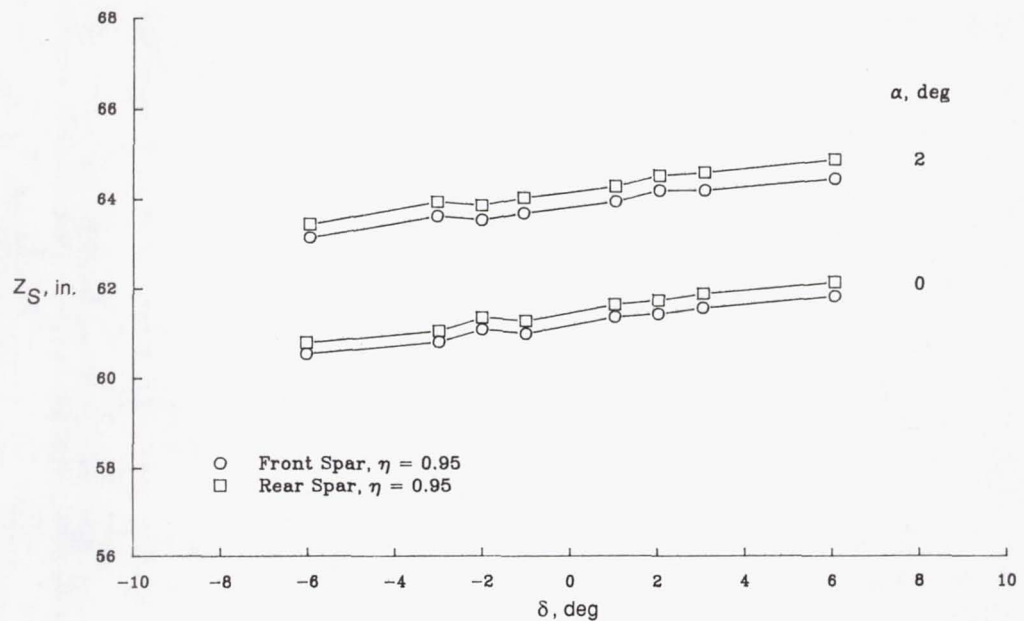


(a)  $M = 0.600$ .

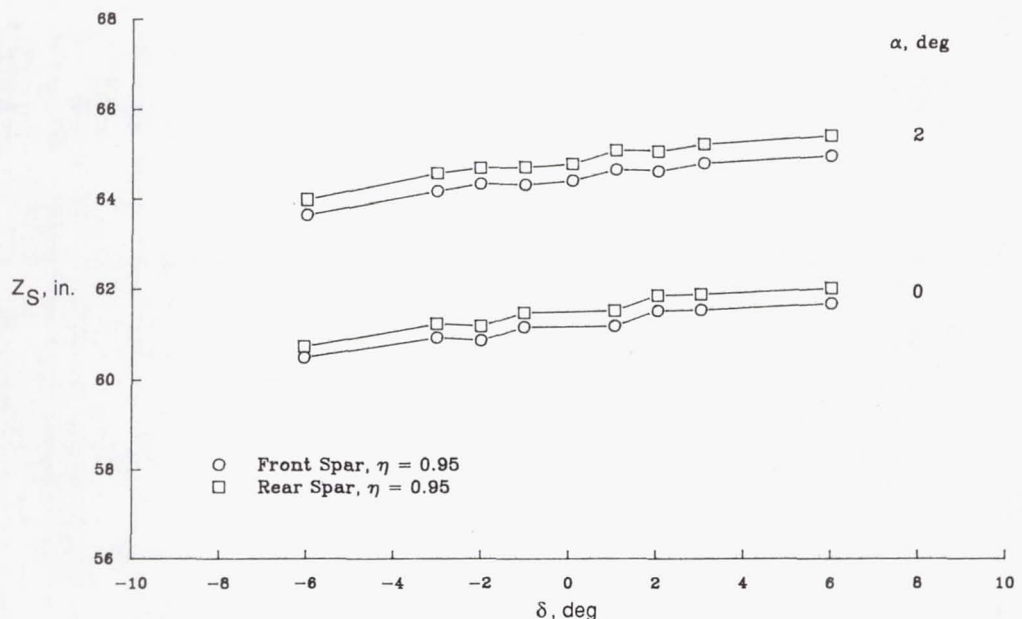


(b)  $M = 0.700$ .

Figure 27. Variation of wing front and rear spar tip deflection with control surface deflection at four Mach numbers, two angles of attack, and  $q = 200$  psf.



(c)  $M = 0.800$ .



(d)  $M = 0.850$ .

Figure 27. Concluded.

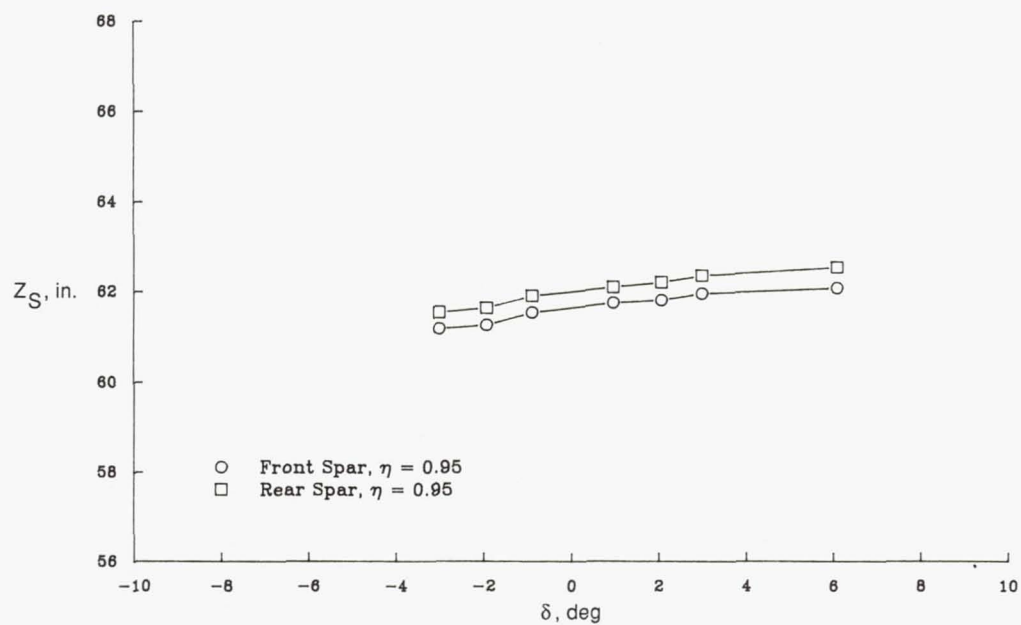
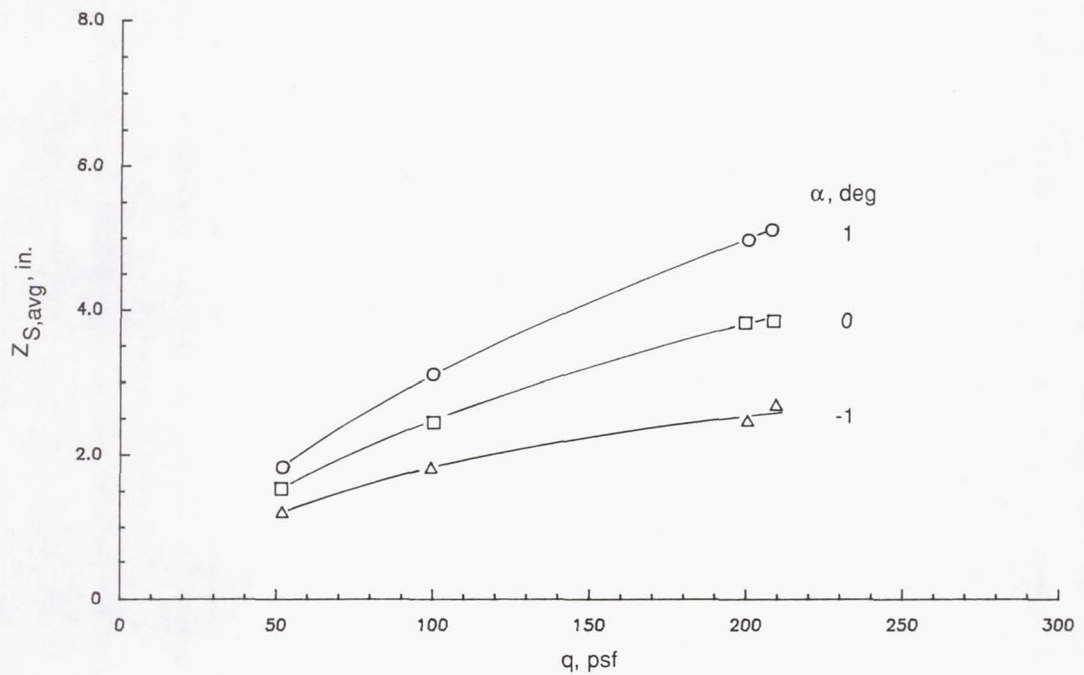
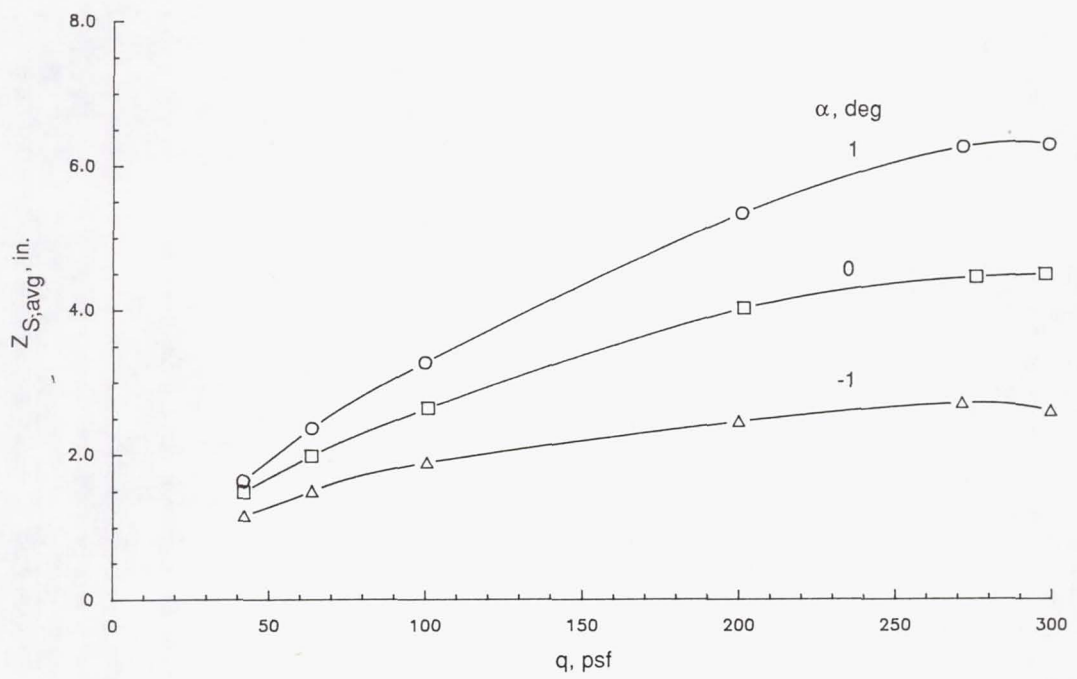


Figure 28. Variation of wing front and rear spar tip deflection with control surface deflection at  $\alpha = 0^\circ$ ,  $M = 0.800$ , and  $q = 300$  psf.

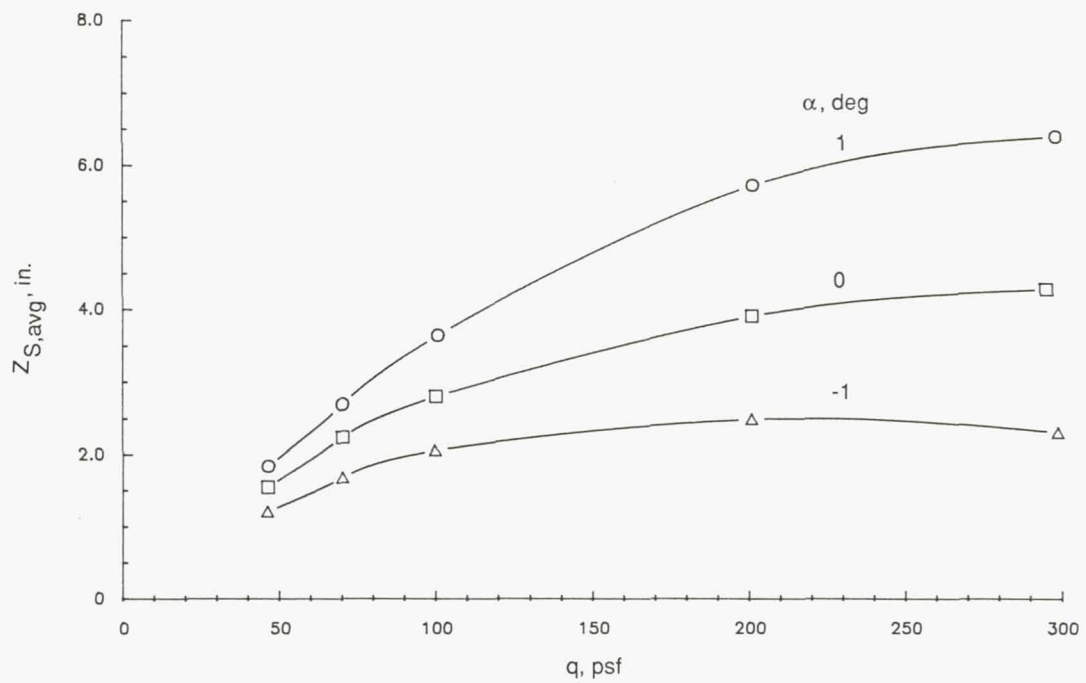


(a)  $M = 0.700$ .



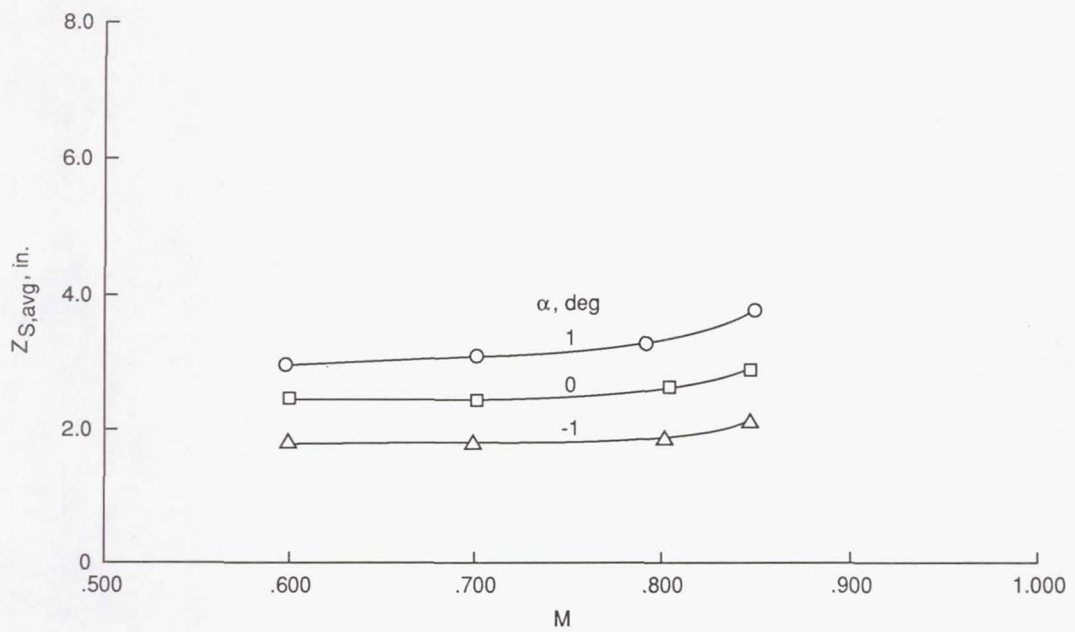
(b)  $M = 0.800$ .

Figure 29. Variation of average wing spar tip deflection with dynamic pressure at  $M = 0.700, 0.800$ , and  $0.850$  and three angles of attack. Control surface deflection,  $0^\circ$ ;  $Z_{S,avg} = 0.50(Z_{S,1002} + Z_{S,1004})$ .

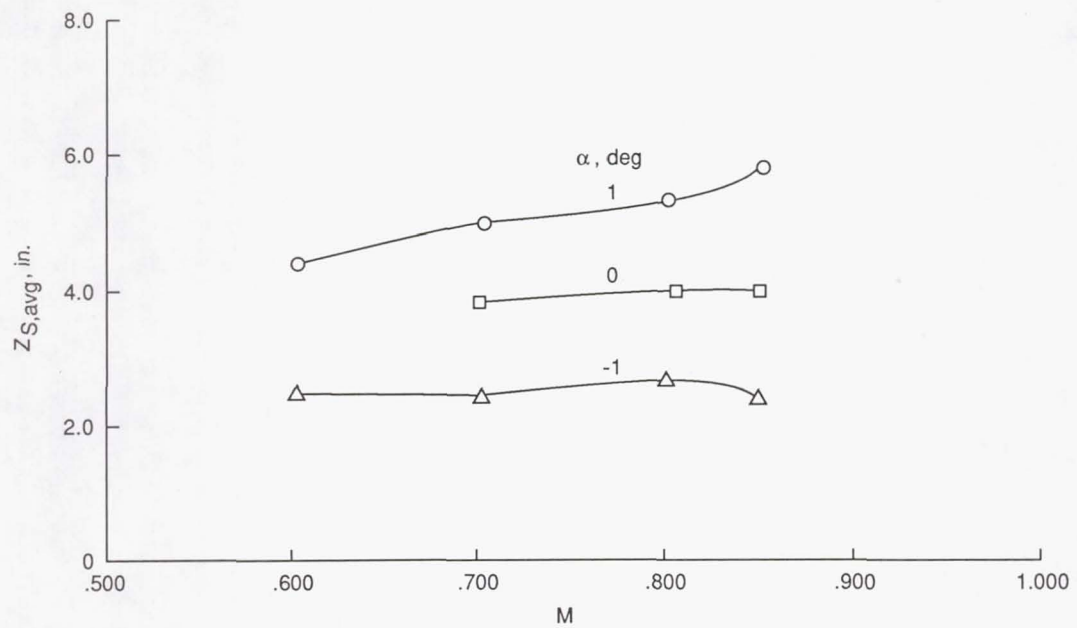


(c)  $M = 0.850$ .

Figure 29. Concluded.



(a)  $q = 100$  psf.



(b)  $q = 200$  psf.

Figure 30. Variation of average wing spar tip deflection with Mach number at  $q = 100$  and 200 psf and three angles of attack.  $Z_{S,\text{avg}} = 0.50(Z_{S,1002} + Z_{S,1004})$ .

The results of quasi-steady deflection measurements for an aeroelastic research wing are tabulated in a "Supplement to NASA TM-4194."

Copies of this "Supplement to NASA TM-4194" will be furnished upon request. Requests for the supplement should be addressed to:

NASA Scientific and Technical Information Facility  
P.O. Box 8757  
Baltimore/Washington International Airport, Maryland 21240

Cut here

Date \_\_\_\_\_

Please forward "Supplement to NASA TM-4194" to

Name of organization \_\_\_\_\_

Street number \_\_\_\_\_

City and state \_\_\_\_\_ Zip code \_\_\_\_\_

Attention: \_\_\_\_\_

Name \_\_\_\_\_

Title \_\_\_\_\_



National Aeronautics and  
Space Administration

## Report Documentation Page

1. Report No. NASA TM-4194	2. Government Accession No.	3. Recipient's Catalog No.	
4. Title and Subtitle Close-Range Photogrammetric Measurement of Static Deflections for an Aeroelastic Supercritical Wing		5. Report Date December 1990	
7. Author(s) Thomas A. Byrdsong, Richard R. Adams, and Maynard C. Sandford		6. Performing Organization Code	
9. Performing Organization Name and Address NASA Langley Research Center Hampton, VA 23665-5225		8. Performing Organization Report No. L-16720	
12. Sponsoring Agency Name and Address National Aeronautics and Space Administration Washington, DC 20546-0001		10. Work Unit No. 505-63-21	
15. Supplementary Notes		11. Contract or Grant No.	
16. Abstract Close-range photogrammetric measurements were made for the lower surface of an aeroelastic supercritical research wing having a full-span aspect ratio of 10.3. The measurements were made during wind-tunnel tests of quasi-steady pressure distributions on the wing. The tests were conducted in the Langley Transonic Dynamics Tunnel at Mach numbers up to 0.900 and dynamic pressures up to about 300 psf. Deflection data were obtained at 57 locations on the wing lower surface with dual nonmetric still-frame cameras. Representative data are presented as a graphical overview to show variations and trends of spar deflection with test variables. Comparative data are presented for photogrammetric and cathetometric results of measurements of the wingtip deflections.			
17. Key Words (Suggested by Authors(s)) Wing deflection measurements Supercritical wing deflection		18. Distribution Statement Unclassified—Unlimited	
Subject Category 02			
19. Security Classif. (of this report) Unclassified	20. Security Classif. (of this page) Unclassified	21. No. of Pages 93	22. Price A05